Master Thesis

Measuring apparent flow vector on a flexible wing kite

Johannes Oehler

Supervisor: Prof. Dr. P.W. Cheng
Dr.–Ing. R. Schmehl

University of Stuttgart
Stuttgart Wind Energy (SWE)
@ Institute of Aircraft Design
Prof. Dr. P.W. Cheng

Delft University of Technology
Wind Energy Section
@ Institute for Aerodynamics, Wind Energy, Flight Performance and Propulsion (AWEP)
Prof. Dr. G. van Bussel

May 2017

Abstract

In order to use flexible wing kites effectively in power generation, their size must be increased and aerodynamic performance should be systematically improved. To this end, validated models to predict the behavior of future kite designs are essential. The biggest uncertainty in current modeling approaches appears in the air flow experienced by the kite. This thesis develops a measurement setup for the apparent flow vector. An air data boom with a Pitot-static tube and two wind vanes is used to sense the relative flow directly below the kite. The acquired data is validated and shows that high-quality in-situ measurements of relative flow information are possible using the presented airborne setup.

Experimental data supports the current quasi-steady model for a pumping kite power system [22]. The thesis suggests a mechanistic model for the resulting aerodynamic coefficient of the airborne kite system c_R. A sole dependency of this aerodynamic coefficient on the angle of attack, as it is customary for rigid airfoils, must be rejected. Instead, the coefficient is found to be heavily dependent on the wing loading and to a lesser extent on the power ratio i.e. the non-dimensional measure for the active pitch control of the wing. The experimental data shows that the kite's angle of inflow changes during flight even when the wing is not actively pitched. This effect is mainly induced by gravitation. Further it is observed that the oscillation of the reeling velocity results in a high frequency flutter of the wing. The relation for c_R presented in this work can be used for flight path optimization as well as kite design.

Abstract

Um Kitesysteme mit verformbarem Tragflügel effektiv zur Stromerzeugung zu nutzen, sind zum einen deutlich grössere Tragflächen als bei den aktuell genutzten Surfkite-Sportgeräten erforderlich, zum anderen sollte die aerodynamische Güte der Fluggeräte verbessert werden. Validierte Modelle um das Verhalten von neuen Kitekonzepten vorherzusagen sind notwendig. Die grösste Unsicherheit bei der Modellierung ist derzeit die relative Strömung, die der Kite erfährt. In dieser Arbeit wird ein Messaufbau für den relativen Strömungsvektor entwickelt. Ein Air Data Boom mit einem Pitot-Static-System und zwei Windfahnen misst die relative Strömung unter dem Kite. Die aufgezeichneten Daten werden validiert und zeigen, dass es mit der entworfenen Messapparatur möglich ist, eine genaue in-situ Messung des relativen Strömungsvektors durchzuführen.

Die experimentell ermittelten Daten stützen das Modell eines Windenergiekonverters mit einem zyklisch fliegenden Kite aus [22]. In der Arbeit wird ein mechanistisches Modell für den resultierenden aerodynamischen Koeffizienten des fliegenden Systems c_R vorgestellt. Dieser Koeffizient ist bei verformbaren Kites, anders als bei Fluggeräten mit starren Flügeln, nicht allein vom Anstellwinkel abhängig. Der Koeffizient hängt in diesem Fall stark von der Tragflächenbelastung ab und weniger vom Leistungsverhältnis PR, das ein dimensionsloses Mass für die aktive Pitch-Einstellung des Kites darstellt. Die Messungen zeigen, dass sich der Anströmwinkel des Kites auch ohne aktives Pitchen aufgrund der Schwerkraft ändert. Ausserdem wird ein hochfrequentes Flattern des Tragflügels beobachtet, das durch die Schwankungen der Kiteabspulgeschwindigkeit v_{reel} verursacht wird. Die entwickelte Berechnungsmethode für c_R kann zur Optimierung der Flugbahn oder des Kitedesigns verwendet werden.

Acknowledgements

I am very grateful that I could work and write my thesis on the interesting and challenging topic of airborne wind energy. I would like to thank my supervisors Professor Po Wen Cheng and Dr. Roland Schmehl for offering me this opportunity. It was motivating for me to dive into this completely new subject and still being able to use and profit of what I had learned during my studies of aerospace engineering in Stuttgart.

Thank you Roland and all members of the kite power research group in Delft for your helpful comments and discussions. I am hoping to continue some of them.

Without the team of Kitepower this thesis would never have been successful. Thank you all for supporting my work and helping me with the physical building of crucial parts of my thesis. Special thanks to Joep, Bert and Bruno who contributed a lot to build a useful and working measurement setup.

Thank you all my fellow master students from room 6.08! Without you my stay in Delft and my thesis would not have been the same. Obviously. Thank you Bas for all your moral and IT support, thank you Clara and Pranav for helping me in any possible situation and being my friends. Thank you all others for your support and the many nice days and evenings we spent together!

Thank you C. V. L. & M., I was unspeakably lucky to meet you and live with you. Thank you for putting me upright again when I wasn't and for making the time we had so brilliant.

Last but not least I would like to thank my brother Daniel and all my family as well as some others for their backing throughout my studies and life and for making the person I am out of me.

Erklärung des Kandidaten

Ich versichere, dass diese Masterarbeit selbständig von mir verfasst wurde - abgesehen von der Mitwirkung der genannten Betreuer - und dass nur die angegebenen Quellen und Hilfsmittel verwendet wurden.

Datum

Johannes Oehler

"Es genügt nicht, die Welt zu verändern. Das tun wir ohnehin. Und weitgehend geschieht das sogar ohne unser Zutun. Wir haben diese Veränderung auch zu interpretieren. Und zwar, um diese zu verändern. Damit sich die Welt nicht weiter ohne uns verändere. Und nicht schliesslich in eine Welt ohne uns."

G. Anders

Contents

1 Introduction **1**
- 1.1 Motivation . . . 1
- 1.2 Use of kites for energy conversion . . . 2
- 1.3 Kite development . . . 2

2 Problem description and state of the art **3**
- 2.1 Description of the pumping kite concept . . . 3
- 2.2 Coordinate systems for tethered flight . . . 4
- 2.3 Flight path, forces and velocities for tethered flight . . . 6
- 2.4 Attempts to measure air speed . . . 10

3 Goal of the thesis and methodology **13**
- 3.1 Accurate definition . . . 13
- 3.2 Research methodology . . . 13

4 Sensor choice and test setup **15**
- 4.1 Requirements . . . 15
- 4.2 Concepts for flow measurement . . . 16
  - 4.2.1 Mechanical and Sonic Anemometers . . . 17
  - 4.2.2 Multi-hole probe . . . 18
  - 4.2.3 Air data boom with mechanical wind vanes . . . 19
- 4.3 Sensor position . . . 21
  - 4.3.1 Sensors mounted on the kite . . . 21
  - 4.3.2 Sensors mounted in the bridles . . . 21
  - 4.3.3 Perturbation of the air flow . . . 22

5 Construction and calibration **25**
- 5.1 Mounting and structure of the measurement assembly . . . 25
- 5.2 Pitot tube . . . 27
- 5.3 Angle measurement . . . 29
- 5.4 Data transfer and sensor platform . . . 31
- 5.5 Calibration and expected measurement error . . . 33
  - 5.5.1 Airspeed magnitude . . . 33
  - 5.5.2 Wind vanes . . . 40

6 Flight data **43**
6.1 Airspeed data validation 44
6.2 Calculation of the aerodynamic coefficient 50
6.3 Inflow angles 54
6.4 Prediction of c_R 61

7 Conclusion and outlook **65**
7.1 Conclusion 65
7.2 Outlook and recommendations 66

Bibliography **79**

Nomenclature

Latin Symbols

alt_{kite}	$[m]$	Altitude of the kite from GPS signal
alt_{GS}	$[m]$	Altitude of the ground station
alt_p	$[m]$	Altitude of the kite from measured pressure
alt_{ref}	$[m]$	Reference altitude of the kite
alt_T	$[m]$	Altitude of the kite from measured temperature
alt_0	$[m]$	Altitude of the kite before launch
$c_{D,plate}$	$[-]$	Drag coefficient of the wind vane
c_R	$[-]$	Resultant aerodynamic coefficient airborne system
c_R*	$[-]$	Calculated aerodynamic coefficient airborne system
$c_{R,hydra,22kt}$	$[-]$	Resultant aerodynamic coefficient of the Hydra kite at $22kt$ wind speed
$c_{R,hydra,29kt}$	$[-]$	Resultant aerodynamic coefficient of the Hydra kite at $29kt$ wind speed
$down_{GPS}$	$[m]$	Position of the kite in NED coordinate system
$east_{GPS}$	$[m]$	Position of the kite in NED coordinate system
F_a	$[N]$	Resultant aerodynamic force of the airborne system
$F_{a,max}$	$[N]$	Maximum aerodynamic force of the airborne system
F_t	$[N]$	Tether force at the upper end of the main tether
F_{tg}	$[N]$	Tether force at the ground station
g	$[m/s^2]$	Acceleration of gravity

K	$[m]$	Kite position vector in NED coordinates
k_{down}	$[m]$	Kite position below the ground station
k_{east}	$[m]$	Kite position east of the ground station
k_{north}	$[m]$	Kite position north of the ground station
$k_{\Delta p}$	$[-]$	Scaling factor for measured differential pressure
$k_{\Delta p,not-aligned}$	$[-]$	Alternative scaling factor for differential pressure
L	$[m]$	Tether length
$\frac{L}{D}$	$[-]$	Lift-to-drag ratio of the kite
lat_{GS}	$[°]$	Latitude of the ground station
lat_{kite}	$[°]$	Latitude of the kite
$long_{GS}$	$[°]$	Longitude of the ground station
$long_{kite}$	$[°]$	Longitude of the kite
$M_{stiction}$	$[Nm]$	Mechanical stiction torque of the wind vane
m	$[kg]$	Combined mass of the airborne system except tether
m_t	$[kg]$	Mass of the main tether
$north_{GPS}$	$[m]$	Position of the kite in NED coordinate system
P_{mech}	$[W]$	Mechanical Power
PR	$[-]$	Power ratio of the V3-kite
PR_{Hydra}	$[-]$	Power ratio of the Hydra kite
PR_{max}	$[-]$	Maximal power ratio
PR_{min}	$[-]$	Minimal power ratio
p	$[Pa]$	Air pressure
p_s	$[Pa]$	Static pressure
p_t	$[Pa]$	Total pressure
$p_{measured}$	$[Pa]$	Measured air pressure
p_{offset}	$[Pa]$	Offset value to correct measured air pressure
p_0	$[Pa]$	Initial air pressure before launch

R	$[J/(kgK)]$	Specific gas constant of air
r	$[m]$	Distance of the kite to the ground station
r_t	$[m]$	Radius of the main tether
r_v	$[m]$	Leverage arm of the wind vane
$range_{\Delta p}$	$[Pa]$	Range of the differential pressure sensor
$resolution_{\xi}$	$[°]$	Resolution of the AS5043 angular sensor
$resolution_{\Delta p}$	$[Pa]$	Resolution of the differential pressure sensor
S	$[m^2]$	Reference surface area of the kite
S_v	$[m^2]$	Reference surface area of the vane
$size_T$	$[bit]$	Size of the data package for air temperature
$size_{\Delta p}$	$[bit]$	Size of the data package for differential pressure
T	$[K]$	Air temperature
$T_{calibrated}$	$[K]$	Calibrated measured air temperature
T_{mean}	$[K]$	Mean air temperature during test flight
$T_{measured}$	$[K]$	Measured air temperature
T_{offset}	$[K]$	Offset value to correct measured air temperature
T_{ref}	$[K]$	Reference air temperature
$TEB_{\Delta p}$	$[\%]$	Total error band of the differential pressure sensor
t	$[s]$	Time after launch of the kite
$U_{polyfit}$	$[V]$	Ideal signal voltage obtained with a fitting function
U_{ref}	$[V]$	Supply and reference voltage for the angular sensors
U_{signal}	$[V]$	Signal voltage of the AS5043 sensor
U_1	$[V]$	Signal voltage of the sideslip angle vane
U_2	$[V]$	Signal voltage of the vertical inflow angle vane
V_a	$[m/s]$	Apparent flow vector of the kite
$V_{a,farfield}$	$[m/s]$	Flow vector at the boundaries of the CFD domain
$V_{a,local}$	$[m/s]$	Local flow vector of the CFD calculation

V_k	$[m/s]$	Kite velocity vector
V_w	$[m/s]$	Wind vector
v_a	$[m/s]$	Apparent flow velocity of the kite
$v_{a,farfield}$	$[m/s]$	Flow velocity at the boundaries of the CFD domain
$v_{a,local}$	$[m/s]$	Local flow velocity of the CFD calculation
$v_{a,ref}$	$[m/s]$	Reference true flow velocity
$v_{a,40}$	$[m/s]$	Apparent flow velocity calculated with an offset value for the differential pressure of 40 Pascal
$v_{a,+}$	$[m/s]$	Maximal calculated flow velocity in reference case
v_k	$[m/s]$	Kite flight speed

Greek Symbols

α	$[°]$	Vertical inflow angle
$\alpha_{farfield}$	$[°]$	Kite's angle of attack in CFD simulation
$\alpha_{mean,cycle6-10}$	$[°]$	Average inflow angle for cycles 6-10
$\alpha_{mean,reelin}$	$[°]$	Average inflow angle during reel-in phase
$\alpha_{mean,traction}$	$[°]$	Average inflow angle during traction phase
$\alpha_{mean,0-2000}$	$[°]$	Average inflow angle for the first $2000s$
α_v	$[°]$	Angle of attack of the wind vane
$\alpha_{stiction}$	$[°]$	Minimal angle of attack to overcome stiction
β	$[°]$	Sideslip angle
β_{mean}	$[°]$	Average sideslip angle during test flight
$\beta_{mean,ideal}$	$[°]$	Expected average sideslip angle for a symmetric kite
β_{pitot}	$[°]$	Yawing angle of the Pitot tube
γ	$[°]$	Deviation of the local flow direction from farfield flow
Δp	$[m^2/s]$	Differential pressure

Δp_{pitot}	$[Pa]$	Measured differential pressure
Δp_{offset}	$[Pa]$	Offset value to correct measured differential pressure
$\Delta p_{offset,c}$	$[Pa]$	Offset value measured prior to test flight
Δp_{WT}	$[Pa]$	Differential pressure in the wind tunnel
Δv_a	$[m/s]$	Error of the calculated apparent flow velocity
δp	$[Pa]$	Uncertainty of the air pressure measurement
ϵ	$[°]$	Depower ratio angle of the kite (see Fig. 5.2)
θ	$[°]$	Polar angle of the kite
ξ	$[°]$	Turning angle of the AS5043 angle encoder
Π	$[-]$	Ratio of measured to actual differential pressure
ρ	$[kg/m^3]$	Air density
ρ_t	$[kg/m^3]$	Density of the main tether
σ_U	$[V]$	Standard deviation of the signal voltage
σ_α	$[V]$	Standard deviation of the calculated angle
ϕ	$[°]$	Azimuth angle of the kite in wind reference frame

Abbreviations

ADC	Analog-to-Digital Converter
AWES	Airborne Wind Energy System
CAD	Computer Aided Design
CFD	Computational Fluid Dynamics
FSI	Fluid-Structure Interaction
I2C	Inter-Integrated Circuit
IMU	Inertial Measurement Unit
ISA	International Standard Atmosphere
KCU	Kite Control Unit
LEI	Leading-Edge Inflatable
NED	North-East-Down
PCB	Printed Circuit Board

List of Figures

2.1 Concept of the pumping cycle traction kite system [1] 3
2.2 Kite position and used reference frames 5
2.3 Wind vectors for a kite in parking mode and crosswind flight after [15] 6
2.4 Three-dimensional kite flight path in North-East-Down coordinate system during one full pumping cycle 7
2.5 Forces acting on a kite while flying ideal crosswind vertically with and without the effect of gravity 8
2.6 Flying upwind and downwind in crosswind mode 9
2.7 Current measurement device for apparent flow velocity 11

4.1 Different mechanical and sonic anemometers 17
4.2 Multi-hole probe in an airborne wind energy application [4] 18
4.3 Air data booms of different size 19
4.4 Deviation from farfield flow velocity $v_{a,farfield}$ in proximity of the kite (from [6]) 22
4.5 Angular deviation from unperturbed farfield flow vector $V_{a,farfield}$ in proximity of the kite (from [6]) 23

5.1 Sensor position in the bridles below the kite and definition of inflow angles 26
5.2 Definition of the inflow angle α and the power ratio angle ϵ [17] . 27
5.3 Sensor setup mounted in the bridles above the KCU 28
5.4 New (left) and old (right) Pitot-static tube 29
5.5 Assembly for angular measurement 30
5.6 Mechanical and electrical components of the windvane assembly . 30
5.7 Wind vane assembly for angular measurement mounted in the wind tunnel 31
5.8 Measured oscillation of supply voltage and signal voltage due to current drawn by other consumers 32
5.9 Complete measurement assembly with pivotable Pitot tube, two wind vanes, data processing unit and camera 33
5.10 Measured differential pressure by the Pitot-static system 34
5.11 Measured barometric pressure compared to the wind tunnel reference 36
5.12 Measured air temperature compared to the wind tunnel reference 37
5.13 Yawing effect on differential pressure measurement 38

5.14 Measurement error due to uncertainty in Pitot tube misalignment 39
5.15 Calibration of the wind vane 41

6.1 Kite altitude throughout the entire flight test 43
6.2 Picture of the on-board camera 20 seconds after take-off 44
6.3 Comparison of kite altitude obtained from different sources 45
6.4 Calculated apparent flow velocity v_a using different calibration rules during launch sequence 48
6.5 Calculated apparent flow velocity v_a for different calibration rules while flying pumping cycles 49
6.6 Variation of the aerodynamic coefficient c_R over 8 pumping cycles 52
6.7 Variation of the aerodynamic coefficient c_R with depower ratio and wind speed for different kites [17] 53
6.8 Prediction of the aerodynamic coefficient c_R over 8 pumping cycles using power ratio and wing loading 54
6.9 Signal and supply voltages for the angular measurement during one hour of testflight 55
6.10 Smoothing rule for the measured angles to correct for errors induced by supply voltage oscillation 56
6.11 Variation of the inflow angles β and α during flight 57
6.12 Variation of the inflow angles β and α during one pumping cycle . 58
6.13 Variation of the inflow angle α and c_R during traction phase . . . 59
6.14 High frequency oscillations of the inflow angle α and v_{reel} during traction phase show the same frequency and a good correlation . . 61
6.15 Predicted c_R* value calculated from aerodynamic Force F_a, power ratio and inflow angle α compared with real c_R 62
6.16 Predicted c_R* values during traction phase calculated from aerodynamic Force F_a, power ratio and inflow angle α compared with real c_R 63

List of Tables

6.1 Difference between calculated air temperature T and measured air temperature $T_{calibrated}$ 46

Chapter 1

Introduction

1.1 Motivation

Transition of humanity's energy metabolism towards a more sustainable way is essential to secure future life on earth. One essential element of this metabolism is the generation and use of electricity. Wind energy is today contributing the biggest portion to the growth of electricity production from renewable sources. However by moving from a niche market that supplements conventional power plants towards the future backbone of electricity generation wind energy exploitation faces some major challenges these days.

- The variance of their power output combined with a limited grid and storage capacity set's a physical limit to the share of renewables in electricity generation.

- Acceptance of new wind farm projects by broad public set's a social and political limit to their further extension.

- Finite availability of free land area with high wind speeds curbs the efficiency of future projects with current technology.

Airborne Wind Energy Systems (AWES) can solve the major problems of current renewable electricity production. By accessing and exploiting steadier winds further away from the earth's surface, they can reach high capacity factors, thereby decreasing the fluctuation of energy production and need for storage capacity in a renewable energy supply scenario. By flying high aloft they are also further away from our eyes and ears, so both visual impact on the landscape and contribution to noise pollution are minimized. AWES can further open new wind harvesting potential in areas where conventional turbines cannot be operated economically due to low wind speeds as they exploit high altitude winds that are present in almost every region on earth.

1.2 Use of kites for energy conversion

Several approaches exist for the design of AWES such as lighter-than-air wind turbines, autonomously flying aircraft exploiting wind shear in the upper atmosphere as well as various kinds of tethered wings, commonly referred to as kites [20]. Most research and development is today focused on kites with either a ground based or airborne generator. This thesis will focus on flexible wing kites which are used on the TU Delft's pumping cycle AWES prototype. Kites were the first flying objects created by humans but were unlike aircraft lacking broad scientific interest until the late 20th century. Despite their use in arts, cult, war and leisure for millenia, using kites for energy conversion gained attention only after Miles L. Loyd published his paper "crosswind kite power" in 1980 which suggested the use of kites to produce electricity. His estimations show that AWES could easily supply global electricity demand [15].

1.3 Kite development

Current soft kites used in the TU Delft's AWES prototype are surfkites or upscaled versions of them. As of now there is no scientific approach implemented to assist kite design and predict the performance of a future kite. The upscaling and development of a new kite is based on prior experience. Testing the kite and searching to eliminate shortcomings of the chosen design in the future is the current method to find an appropriate kite design.
This trial and error approach is used for surfkites as well, but not deemed efficient with kite size, complexity and demands increasing. Comparing kites with aircraft one can say that there was a similar development. First designs were selected in a trial and error process rather than a theoretical approach. But in order to advance and develop ever bigger and more capable aircraft scientific investigation was necessary. Trial and error is not a suitable method to design a $100m^2$ kite just as it is unrealistic to successfully build a new helicopter or a 30 meters wingspan aircraft without proper knowledge of its aerodynamics and dynamic behavior.
Further one can not expect to find an optimal kite design considering that the number of prototypes and thus design options considered will be ever smaller, the bigger and more expensive the system is growing. This is why the kite research group is aiming at developing useful numerical tools, using Computational Fluid Dynamics (CFD) and considering Fluid-Structure Interaction (FSI) in order to predict and thereby improve aerodynamic performance of future flexible wing kites.
To develop tools for kite simulation the validation of current models is absolutely necessary. The intention of this thesis is not providing real time data for operation, but delivering a data set which allows to validate numerical tools.

Chapter 2

Problem description and state of the art

Scope of this project is the prototype of a pumping cycle power kite AWES tested and operated by TU Delft and kitepower B.V. which uses a leading edge inflatable LEI-kite.

2.1 Description of the pumping kite concept

In order to develop a suitable measurement strategy some basic knowledge about the system of a pumping cycle traction kite is necessary. Power production is achieved by unrolling (Fig. 2.1 top) and retracting (Fig. 2.1 bottom) a tether from a ground based drum that is connected to an electric generator.
The aerodynamic force of the kite tensions the tether and spins the generator during reel-out. While reeling the kite in again the generator must work as a

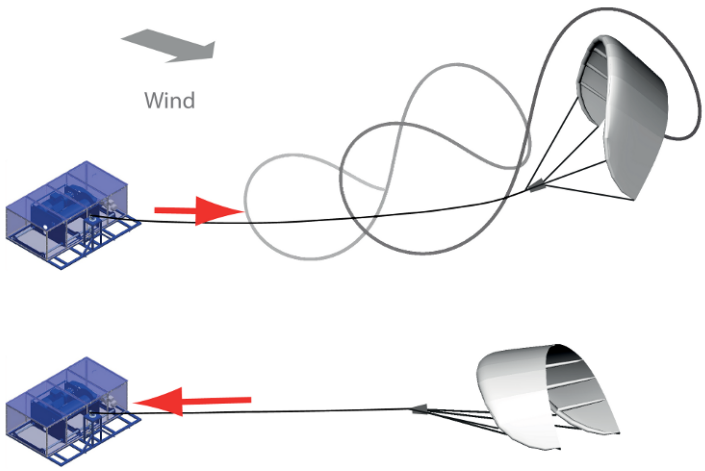

Figure 2.1: Concept of the pumping cycle traction kite system [1]

motor against the tether force. Mechanical power can be calculated by the law

$$P_{mech} = F_{tg} \times v_{reel} \tag{2.1}$$

where P_{mech} is the mechanical power applied on the drum, F_{tg} is the tension in the tether at the ground station and v_{reel} is the reel-out or reel-in speed [1].
In order to achieve a high net power production, tether force should be maximized during reel-out and minimized during reel-in. This requires the aerodynamic force of the kite system F_a which is the cause for the tether tension to vary from one extreme to the other, depending on the active phase of the pumping cycle. The aerodynamic force is calculated according to

$$F_a = c_R \frac{\rho}{2} v_a^2 S \tag{2.2}$$

where c_R is the aerodynamic force coefficient of the kite system, ρ is the air density, v_a is the apparent flow speed of the kite and S is the reference surface area of the kite. F_a does account for all relevant aerodynamic forces of the airborne system which are lift and drag of the kite and tether drag as in [22]. With the kite's reference surface and meteorological conditions constant the aerodynamic coefficient of the kite and its air speed remain the key variables to influence the aerodynamic force and thus tether force. Both values are of great interest to assess flight performance.

2.2 Coordinate systems for tethered flight

Just as for aircraft there are several coordinate systems in use for tethered wings. [19] gives a good overview over the most common coordinate systems. In this section only reference frames with relevance for this thesis will be discussed. This includes the earth fixed North-East-Down (NED) coordinate system and the wind reference frame. Fig. 2.2a shows those two coordinate systems.
Both have their origin at the point where the tether exits the ground station. The wind reference frame has its X-axis aligned with the wind direction and is frequently used for models where a constant wind vector is assumed or at least the wind direction is assumed constant in space. It allows the derivation of simple analytic relations and is used in Sect. 2.3 to explain basic movements of the kite.
For the evaluation of the experimental results I chose to rely on the NED coordinate system. Just as the wind reference system it is a right handed Cartesian coordinate system. The advantage of this coordinate system is that it has a precise definition and does not change with the wind direction. This causes the wind reference system to change constantly in an experiment as the true wind speed is not constant in space and time.
Although there is a sensor for the wind direction installed close to the ground station during the test, we can not assume that this wind direction and the one

the kite experiences during its flight are the same. Firstly we only measure the local flow on the ground which oscillates strongly and secondly we must expect that the wind direction changes by around 10° from ground level to an altitude of $alt = 200m$ [16] where the kite usually flies due to the variation in wind speed in the atmospheric boundary layer.
This effect called Ekman spiral originates from the dependency of the Coriolis force on the wind velocity. Close to the ground friction of the earth surface decellerates the wind and consequently Coriolis force cannot balance the pressure gradient between high and low pressure areas. At high altitudes the wind blows parallel to the isobars, closer to the ground it has an additional component towards areas with low air pressure [16]. This is why the NED coordinate system will be used in Sect. 6 whereas the wind reference frame is mainly used to explain basic kite movements in this section.

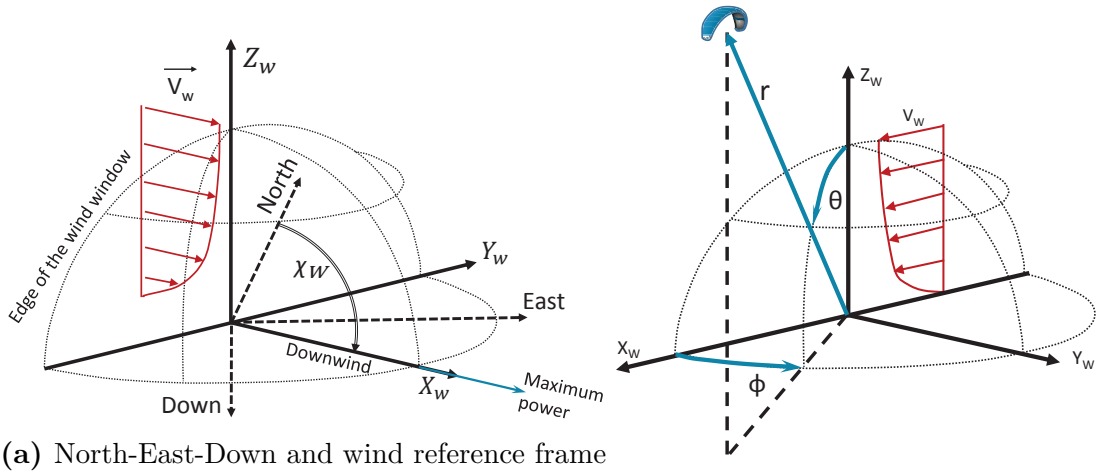

(a) North-East-Down and wind reference frame from [19]

(b) Position of the kite in the wind window

Figure 2.2: Kite position and used reference frames

Fig. 2.2a also shows the wind window which is a quarter sphere where the kite can fly. Generally the kite can only fly downwind of the ground station and experiences the maximal lift force at the perfect downwind position. The closer the kite is to the edge of the wind window, the lower is the traction power of the kite system.
Fig. 2.2b shows the variables that are used to describe the kite's position. The radius r is the distance between kite and ground station, the polar angle θ towards the vertical and the azimuthal angle ϕ towards the downwind direction complete the description of the kite's position in the wind window. As stated before we do not know and cannot define a downwind direction which is valid for all flight situations. This is why the polar angle, which does not depend on wind direction will be used in the experimental part and the azimuthal angle ϕ will only be used

to relate to theoretical kite models.

2.3 Flight path, forces and velocities for tethered flight

During a power kite's usual flight pattern there are two extremal situations which are sketched in Fig. 2.3:

- Firstly, the parking position, where the kite ideally does not move and the apparent flow vector V_a is equal to the wind vector V_w.
- Secondly, ideal crosswind flight perpendicular to the wind direction where V_a reaches its maximum.

In the case of crosswind movement both kite movement V_k and wind vector V_w contribute to the apparent flow vector V_a of the kite. This can result in kite speeds exceeding wind speed by a factor of 5 or more just as the tips of a conventional wind turbine. Perfect crosswind flight of the kite results in the maximum apparent flow speed and maximum tether force F_{tg}. This is why crosswind flight is aimed for during power production phase whereas parking corresponds to the reel-in phase described in Sect. 2.1.
Fig. 2.4 shows an actual kite flight path during one pumping cycle where the GPS position of the kite in NED coordinates relative to the ground station is plotted. In power phase the kite has to turn frequently in order to stay close

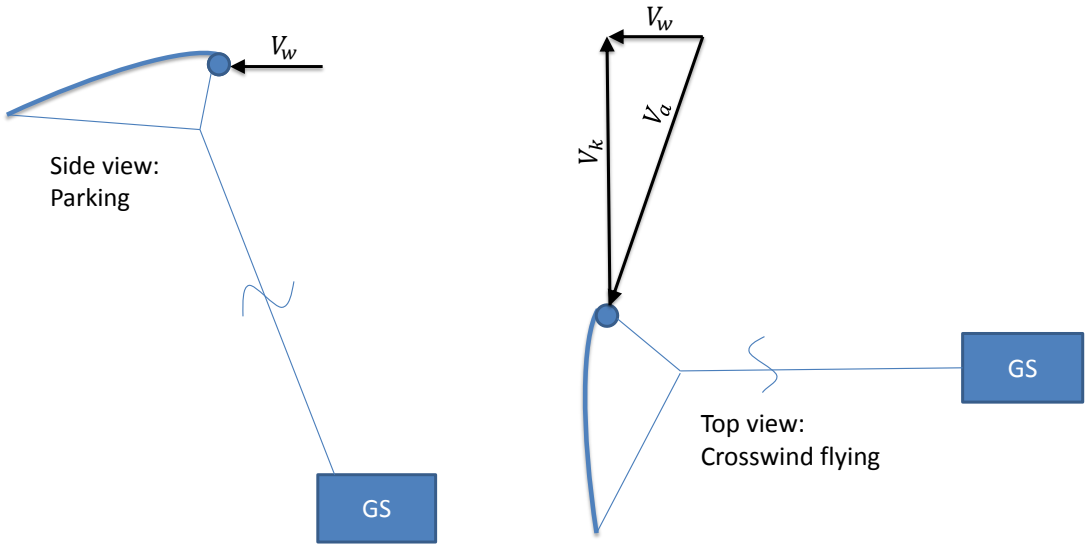

Figure 2.3: Wind vectors for a kite in parking mode and crosswind flight after [15]

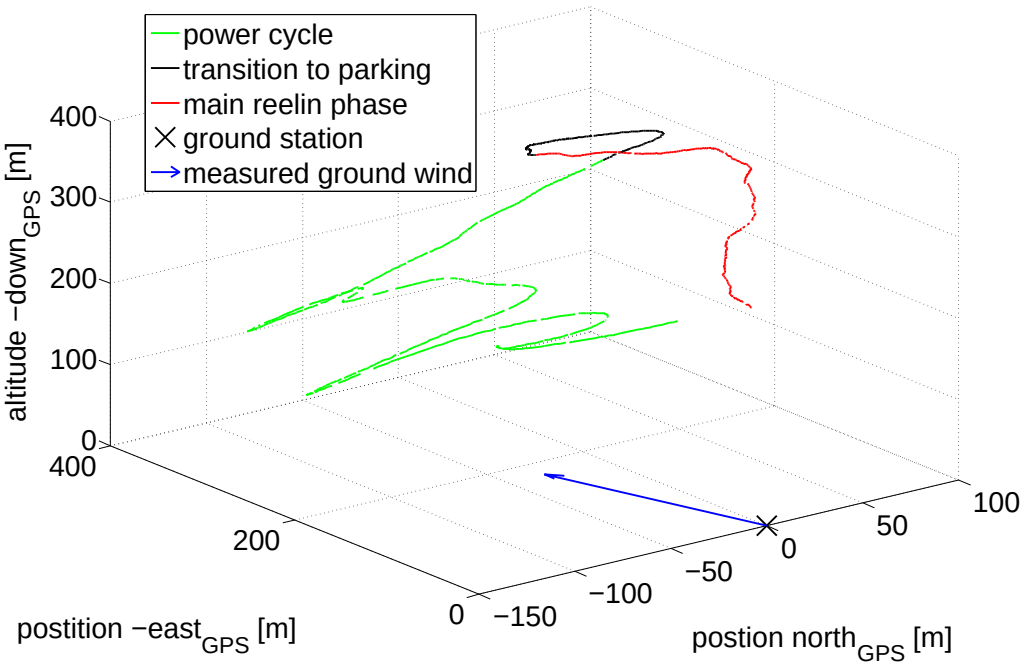

Figure 2.4: Three-dimensional kite flight path in North-East-Down coordinate system during one full pumping cycle

to the downwind position and maintain crosswind flight. Downwind position is where the measured ground wind vector points at. The pattern flown during power cycle should always be centered around the downwind position to achieve maximal power yield which was the case in this flight.
As the kite moves fast during power production phase but is tethered to the ground station and thus forced to stay on a quasi spherical flight path the flight situation is changing quickly and constantly. In this example the kite flies a lying oval followed by a figure of eight thereby increasing its distance to the ground station due to reel-out of the tether. At the end of the power cycle the kite flies into parking position where it reaches its maximal altitude and starts the reel-in phase.

Taking a closer look at the power phase one can distinguish different flight situations during crosswind flight, where apparent flow vector and thus aerodynamic forces acting on the kite change considerably. During one pattern flown such as an oval or a figure of eight the kite's movement is usually composed of all four of these states. The different states are flying upwards or downwards which changes the influence of gravity and flying upwind or downwind which affects the direction of the wind vector with respect to the kite's flight direction. During one traction phase we observe considerable variations of the kite speed in an interval

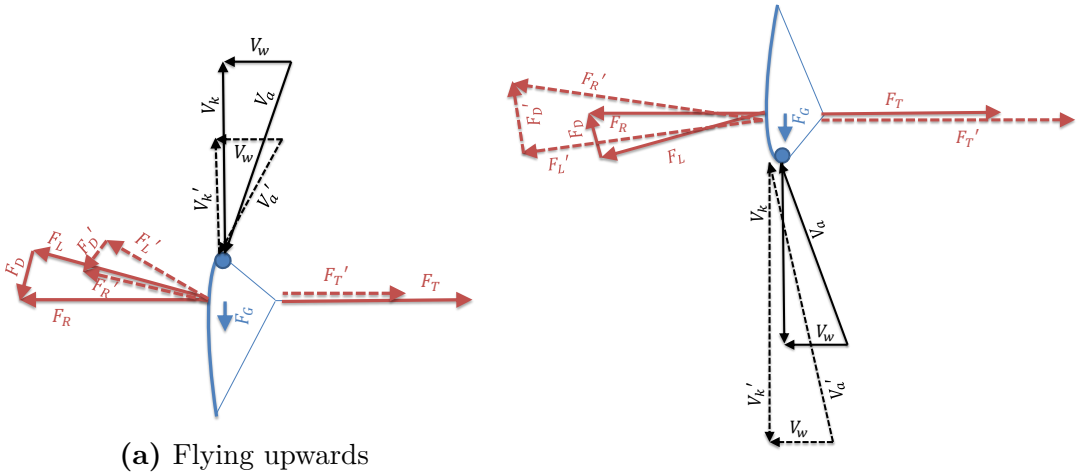

(a) Flying upwards

(b) Flying downwards

Figure 2.5: Forces acting on a kite while flying ideal crosswind vertically with and without the effect of gravity

of $v_k \in [10\frac{m}{s}; 30\frac{m}{s}]$ (compare Fig. 6.5).
Fig. 2.5a shows the forces and velocity vectors of a kite flying upwards. Solid lines picture the situation one would obtain after turning from ideal horizontal crosswind flight instantly into vertical flight. The gravitational force is oriented against flight direction so the forces are not balanced which results in the deceleration of the kite. As the wind vector stays the same, the angle of inflow will increase and the vector of resulting aerodynamic forces is tilted upwards, thereby balancing the gravity influence and resulting in a new force equilibrium (dashed lines) at lower kite speed v_k and apparent flow velocity v_a. The opposite effect leads to a new equilibrium with higher kite speed and lower angle of inflow for downward flight considering gravity influence in Fig. 2.5b. The resulting equilibrium is sketched in dashed lines.

For horizontal kite flight there are also two main flight modes to distinguish:

- Downwind flight where the kite flies towards the perfect crosswind position.
- Upwind flight where the kite flies away from the perfect crosswind position.

Fig. 2.6 shows crosswind flight upwind and downwind on a horizontal semicircle that is part of the hemisphere of the kites possible positions assuming constant tether length. In ideal crosswind flight at the downwind position wind vector V_w and kite speed vector V_k are perpendicular to each other as in Fig. 2.3. For all other positions their relative angle changes with the kite's azimuth angle ϕ relative to the downwind position. Globally the apparent flow vector V_a can be calculated according to

$$V_a = V_w - V_k \tag{2.3}$$

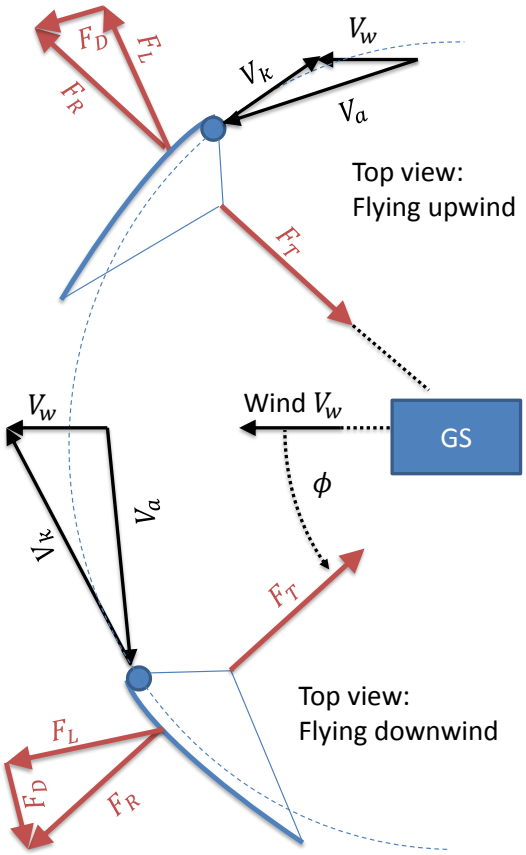

Figure 2.6: Flying upwind and downwind in crosswind mode

from the kite speed vector V_k and the wind vector V_w [1]. For different azimuth angles ϕ the magnitude of V_a changes far less than the kite speed v_k as can be seen in Fig. 2.6. According to [1] the apparent flow velocity is equal in magnitude for a given azimuth angle ϕ be it negative or positive if lift-to-drag ratio of the kite $\frac{L}{D}$ and wind speed v_w are constant. Referring to Fig. 2.6 one can state that in downwind flight kite speed is bigger than apparent flow velocity, whereas for upwind flight it is lower than the apparent flow velocity. In most flight situations the kite movement will be described as a combination of either up or downward flight plus an upwind or downwind component.

2.4 Attempts to measure air speed

As the apparent flow speed is a variable of major interest for kite control and aerodynamic calculations it has been measured before. Several flights were absolved with a Pitot tube installed in the kite's bridles measuring differential pressure [8].
The results of that measurement method were not always satisfying. By its design, the concept did not allow any measurement of the inflow angles but could only supply apparent flow speed magnitude. As explained in detail in Sect. 4.3 the position of the sensor below the kite results in a deviation of the measured dynamic pressure from the undisturbed free stream value. Further was the installation in the bridles difficult and time consuming. Cables for the signal as well as for the power supply had to be connected to the sensor box situated on the kite.
The pressure sensor for the calculation of air density did not work reliably, also was the actual air temperature not recorded. This resulted in a big uncertainty for the value of the air density, in some cases the properties of the International Standard Atmosphere (ISA) would be used [8]. The time synchronization had to be done manually as the airspeed sensor's data and the kite data used for control such as GPS-position and tether force were not logged at the same place.
Concerning the quality of the core components of the measurement equipment, the pitot tube and its differential pressure sensor Franka states several problems. The distance from the pitot static tube's tip to the static pressure port was too small with a value of one tube diameter and five suggested for a good result [2]. Also was the sensor used for differential pressure sensing allowing a certain amount of leakage air flow which would alter the measurement result.
The stream alignment of the sensor as seen in Fig. 2.7a is achieved by a badminton shuttle. In case of misalignment the shuttle's drag inflicts a momentum on the Pitot-static tube to turn it into the apparent flow. At low flight speed this mechanism does not work reliably which results in faulty measurements. Another major problem was the decceleration of the flow upstream of the shuttle which would alter the sensed differential pressure as measurements in [8] show. The

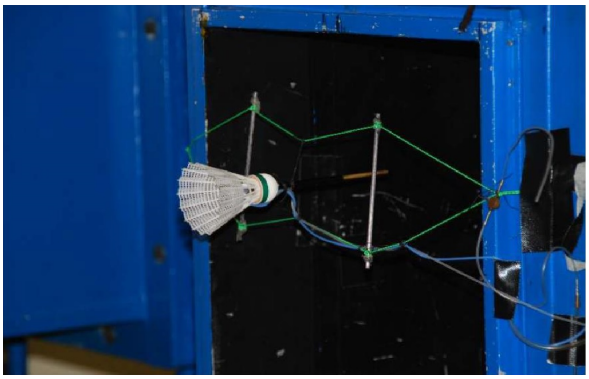

(a) Wind tunnel test

(b) Test flight

Figure 2.7: Current measurement device for apparent flow velocity

sensor setup is shown in Fig. 2.7. Fig. 2.7b shows the mounted setup during a test flight. It is positioned around two chord lengths below the kite's canopy and thus in the middle between kite and Kite Control Unit (KCU).
I will end this brief overview over past experiments with the recommendations of my predecessors. Ruppert's recommendations for a better assessment of the aerodynamic properties of the kite are implementation and use of a better GPS system and use of a better pitot-static-system as well as a more advanced logging method [19]. Francas recommendations in order to achieve accurate airspeed sensing are to

- find or build an improved pitot-static tube with reduced tip proximity errors,
- replace the differential pressure sensor with a sensor that does not allow through- flow, so that no additional errors are introduced,
- ensure proper alignment with the incoming flow throughout the entire kite flight envelope.

Chapter 3

Goal of the thesis and methodology

The goal of this thesis is to

"determine the apparent flow vector of a flexible wing power kite in operation"

3.1 Accurate definition

The apparent flow vector of the kite is defined as the flow vector V_a the kite would encounter at its current position and flight situation without the perturbation of the kite itself. This value is equal to the farfield value for a CFD simulation or the reference airspeed for any analytic calculation.
A flexible wing kite or soft kite is a tethered airfoil which changes its shape with steering and depower input as well as with aerodynamic loading.
The addition "during operation" means that the intended measurement is an in-situ measurement with per se unknown environmental conditions like wind and rain as to distinguish it from a test in a controlled and defined environment.

3.2 Research methodology

The research questions to be answered are:

- How can true air speed magnitude be measured accurately?
- How can inflow angles be measured accurately?
- Which variables have a major influence on the kite's apparent flow vector and thus the aerodynamic forces?
- How can the information of these measurements help to improve the performance of the traction kite power system?

The strategy to answer these questions and thus the thesis outline will be as follows. Firstly, possible flow measurement technologies will be identified and then evaluated with respect to their compatibility with the kite system. The most promising option will then be chosen and an appropriate measurement setup is to be developed. Also the location where to measure the flow vector will be evaluated.
Corrections to correlate the measured data with the intended value of the apparent flow vector V_a will be developed by testing the measurement setup under controlled conditions in the wind tunnel. Finally, the test results in actual flight conditions will be discussed in order to answer the two latter research questions.

Chapter 4

Sensor choice and test setup

The apparent flow vector is composed of the wind vector and the kite speed vector according to

$$V_a = V_w - V_k \tag{2.3}$$

. To obtain the apparent flow vector one can thus either measure it directly or calculate it from wind speed and kite movement. Whereas the kite speed vector is accessible via GPS-data of the kite, the wind vector is difficult to obtain. As seen in Fig 6.1 the power phase where V_a is of greatest interest takes place at an altitude of 120 to 250 meters above ground, during reel-in the kite reaches even higher altitudes. Currently there is no possibility to measure wind speed at the position of the kite at reasonable costs.
Theoretically available measurement methods for wind at the altitude of common wind turbines are metmasts and the Light Detection And Ranging (LIDAR) method as used in [18]. Both are considered too costly for the frame of this thesis. Airborne measurements with kites or ballons as well as aircraft or drones are used for scientific wind measurements at high altitudes [13]. Those methods as well as a metmast measure the wind only at their own position which should for security reasons not be in the range of the kite to avoid a crash.
Consequently would any of those measurements require the extrapolation of the measured signal to the wind at the kite's position which induces a big uncertainty as wind can not be assumed constant over time and space. That's why it is decided to aim for a measurement setup which is flying with the kite, to measure the apparent flow directly. This is also advantageous as only the uncertainty of one measurement has to be considered in contrast to adding wind vector and kite speed vector where the uncertainties of both measurements would sum up.

4.1 Requirements

The goal of the thesis and the decision for an airborne system implicates several requirements for the measurement system. Following needs arise from the thesis goal as stated in Sect. 3.1:

- In order to give a satisfying result for V_a, at least three independent values

must be measured as a vector in three-dimensional space needs three independent values to be clearly identified such as a set of 3 velocities (v_x, v_y, v_z) or magnitude and two orientation angles.

- As the kite system is a flexible structure the measurement setup should be insensitive to a change of the wing geometry.

- The nature of an in-situ measurement requires persistence with respect to the environmental conditions which might occur during kite operation such as temperatures ranging from $-20°C$ to $+40°C$, sun radiation and ideally rain, fog and humidity. As the setup is intended for occasional experiments and not flight control it is acceptable if it is in some conditions not operational.

From the decision for an airborne system additional requirements arise:

- Low weight and low drag in order not to alter flight performance

- High crash worthiness or low cost and easy replacement as a possible crash or rough landing must be expected

- Installation of the system must be easy and quick as well as safe in order not to damage the kite or cause injuries

4.2 Concepts for flow measurement

Except for a multihole probe there is currently no single tool compatible with our requirements to determine apparent flow vector. The most well known instrument to assess apparent flow vector used in airborne applications is an air data boom [11]. It is usually a combination of several sensors, measuring true airspeed magnitude and two inflow angles separately.
The most common wind sensor used for wind turbines and also to measure ground wind in the TU Delft's AWES is an anemometer [9, 1]. Anemometers are also used in scientific research for high altitude wind measurements on kites or metmasts [13].
[3] evaluated different probes for their ability to measure airspeed on a kite accurately. The concepts he rated best were a multi-hole probe, a Pitot-static tube and mechanical or sonic anemometers. As these sensors are all known of having been used in airborne applications the focus is laid on these. Mechanical wind vanes were not part of that study as he had focused on flow velocity and not inflow angles but will be considered as a supplement to Pitot-static tubes in Sect. 4.2.3.

4.2.1 Mechanical and Sonic Anemometers

The most well known and most commonly used anemometer is a cup-anemometer which can measure the wind speed component in one plane [9]. In order to get all the intended information about the apparent flow vector three of those anemometers must be combined.

Another option is a combination of a propeller anemometer which orients itself into the wind in combination with angular vanes in an air data boom assembly, this option will be discussed in Sect. 4.2.3. An alternative to three 1D anemometers would be a sonic 3D anemometer. Fig. 4.1 shows those three different kinds of anemometers: a cup anemometer, two propeller anemometers and a sonic 3D anemometer. A sonic 1D anemometer as used on the ground station for ground wind sensing is excluded from a closer regard as it is assumed inferior to a mechanical anemometer which is much lighter, smaller and cheaper.
Dimensions for a usual threedimensional sonic anenometers are a height of $50cm$ and $25cm$ in diameter, as well as a weight of about one kilogram. Further are they usually not intended for an airborne application but rather for ground wind measurement on buildings, or wind turbines [14]. Taking into account power supply, a data acquisition system and mounting it will require a rather big and heavy construction. High cost for a sonic anemometer as well as low crash resistance are more reasons why this concept is not the favored option. Crash worthiness thereby is not referred too as a design that survives any assumed crash, as this is for any aircraft hardly doable, but rather the likeliness to be operational

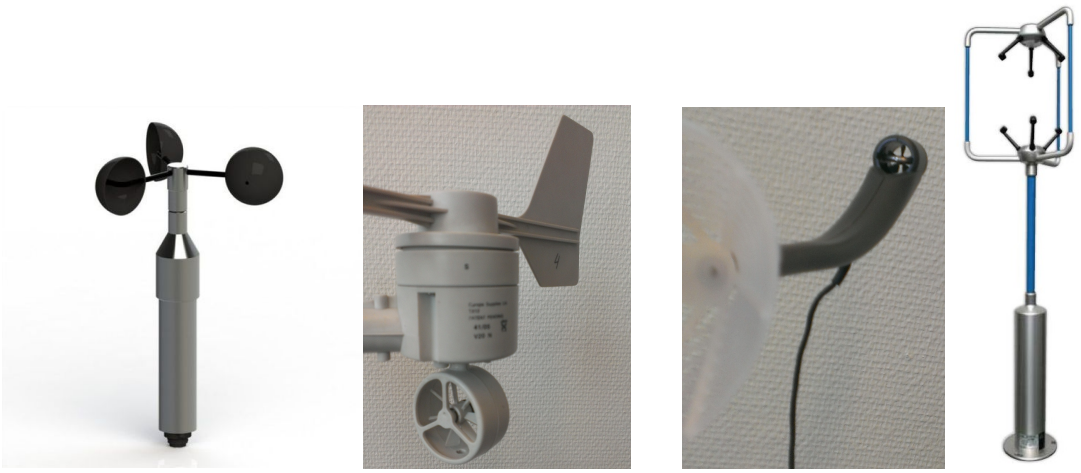

(a) cup anemometer **(b)** propeller anemometers **(c)** sonic 3D anemometer

Figure 4.1: Different mechanical and sonic anemometers

with minor repair after a rough landing.
All the same drawbacks such as large dimensions, weight and sensitivity to a crash are also true for a construction with three mechanical anemometers. Cup and propeller anemometers as shown in Fig. 4.1a and 4.1b are frequently used for wind sensing [9], but rarely seen in flying applications. Combining three of them and thus measuring the flow vector components in every direction separately could give good results in theory. However the measured data only makes sense if all three components are always accurately measured. With only one sensor malfunctioning, the data set will be rendered useless.
Their sensitivity to the inflow angle is the root cause that this technology seems unsuitable for the use on the kite. If there is not a full set of three velocity components it is not possible to determine if a lower measured flow speed originates from a different inflow angle or a lower actual flow velocity. As described in [5] cosine law describes the sensitivity of propeller anemometers towards the inflow angle.

4.2.2 Multi-hole probe

Multi-hole probes are a common tool to measure inflow angles and true airspeed at once in windtunnels and on aircraft [10]. With Ampyx power's PowerPlane there is even a AWES prototype using a multi-hole probe for airborne sensing of the apparent flow speed (see Fig. 4.2.
In usual applications of multi-hole probes there is a rigid structure to mount it and define its orientation. This is not necessarily the case for a flexible wing. Major drawbacks using a multi-hole probe are:

- Low accuracy for angular measurement at low speeds ($v_a < 60\frac{m}{s}$) because of low measured pressure differences [10].

Figure 4.2: Multi-hole probe in an airborne wind energy application [4]

- High crash sensitivity as the sensor should ideally be placed upstream of its mounting to measure free stream values.
- Complicated calibration with several hundreds of calibration points is necessary for an accurate interpretation of measured data [10].
- Cost of several hundreds of euros for a single instrument.

For these reasons using a multi-hole probe is not the option of choice for our flexible wing kite.

4.2.3 Air data boom with mechanical wind vanes

For usual flight operation a Pitot tube is the most frequently used device for airspeed measurement on planes. Air data booms are mainly used in airborne applications where the angle of attack as well as sideslip angle vary for different flight situations. Air data booms are usually additional equipment for calibration or scientific missions e.g. atmospheric research. Air data booms as shown in Fig. 4.3a are usually designed for highly precise measurements on manned aircraft and therefore expensive and large in size to reach the unperturbed flow far away from the aircraft.
For the use on the flexible wing kite such a system is not suitable. Also is the speed range of below $25\frac{m}{s}$ very different from usual flight missions and therefore different sensors are needed. However in recent years with advance in microelectronics and unmanned aerial vehicles (UAV) there are small sized air data booms available such as the miniature air data boom from space age control in Fig. 4.3b.

(a) Air data boom on a Adam A500 propeller aircraft (left wingtip) [21]

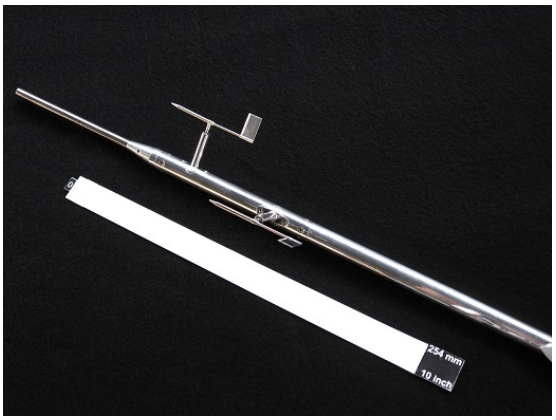

(b) Picture of a miniature air data boom [21]

Figure 4.3: Air data booms of different size

Most air data booms consist of a Pitot tube to measure dynamic pressure and two wind vanes to measure inflow angles. Often temperature and static pressure sensors are integrated to allow calculation of the fluids properties such as density and speed of sound.
The wind speed sensor can be mounted in a flexible way where it can move and align with the stream or fixed as in Fig. 4.3b. If the sensor is fixed to the assembly inflow angles should be small and the sensitivity of the sensor towards a change in inflow angle low. Else the inflow angle data must be used to correct the signal and calculate true air speed magnitude.
Mechanical wind vanes are a proven way to determine inflow angles on airborne and ground wind sensors, even at low wind speeds. Further they are simple to calibrate. So they will be chosen for the inflow angle sensing [11, 23]. For the measurement of flow velocity both Pitot tubes and mechanical anemometers are deemed possible. One major advantage of a mechanical anemometer is that it is nearly insensitive to fog and rain which can pose problems for Pitot and multi-hole probes. It is further easy to calibrate and indicates air speed directly in contrast to a Pitot-static system that measures differential pressure and requires air density for the calculation of flow velocity.
The drawbacks of mechanical anemometers as shown in Fig. 4.1b are that they are much more sensitive to flow misalignment and have a certain inertia [5]. Thus the response time to an abrupt change in air speed will be bigger than for a Pitot tube. Fig 5.13 shows the angular sensitivity for a Pitot tube. For the mechanical anemometer the velocity signal follows the cosine of the angle, whereas for the Pitot tube the differential pressure follows roughly the cosine of the angle. As airspeed grows with the square root of the differential pressure Pitot tubes are far less sensitive for changing inflow conditions with usually very low deviation from the ideal signal for small angles below 15 degrees (compare Fig. 5.13.
The need to measure air density for the Pitot based measurement is not a real disadvantage as aerodynamic formulae such as Eq. 2.2 use differential pressure calculated from density and air speed rather than airspeed alone. The sensor of choice for the air speed magnitude will thus be a Pitot-static system.
To sum it up briefly the air data boom concept with mechanical wind vanes and Pitot-static system will be chosen for the following reasons:

- It is a proven concept for airborne applications that can be miniaturized.
- It measures directly the three variables of interest thus only minimal post processing is needed.
- It can be operated in the expected flight envelope, especially low speed flight.
- It is a fail-safe design as values doe not depend on one another. Any of both angles or differential pressure signal alone provide useful data in case

of single sensor failure. This is a major advantage over multi-hole probes and a combination of anemometers.

4.3 Sensor position

In order to obtain the free stream flow vector that corresponds to the farfield condition of a simulation one has to measure either at a place where there is no perturbation caused by the actual flying object, or correct the measured data for the known influence of the flying object.
As we are in the current situation lacking reliable information of the way the flow is affected by the kite the latter does not seem promising. In fact the measurement to be performed aims to support and validate calculations that could finally tell in which way the flexible structure of the kite interacts with the air flow in different flight situations.

4.3.1 Sensors mounted on the kite

Attaching the flow sensing device to the kite directly in a way analogue to the air data booms used for fixed wing aircraft has one major advantage: The reference system for all measured data is connected to the kite. That way one can always assume that the flow vector of the sensor is equal to the quantity the kite experiences at this position.
The downside is the perturbation of the flow by the kite itself. Depending on the distance between sensors and kite, the sensors will measure the local flow situation which is heavily affected by the kite airfoil. [12] shows that static pressure error varies several percent as a function of lift coefficient c_L for pressure probes mounted in the front of a wing. For a probe half a chord length in front of the wing tip the measured differential pressure varies about 10 % of the dynamic pressure, for a distance of a quarter chord length sensed differential pressure even varies 14% of dynamic pressure. As there is no accurate model yet to determine the kite's actual c_L those errors can not be corrected for. An air data boom that reaches further than half a chord length ahead of the flexible wing would decrease this error. However this requires an air data boom length of much more than one meter which seems unrealistic to be fixed on the flexible kite structure experiencing deformations and high accelerations.

4.3.2 Sensors mounted in the bridles

Mounting the sensor in the bridles as in Fig. 2.7b can eliminate the influence of the kite as one can move the sensors several chord lengths away from the airfoil easily. It will therefore be the option of choice. It requires a mounting of the sensors at a defined position and orientation that can be correlated with the system of a

tethered flexible wing. Expected flow perturbations in proximity of the kite as discussed in this section are the main reason to choose such a mounting.
Installing the sensors on the KCU itself is considered a bad option as the KCU can move independently of the kite in an unpredictable way and does itself perturb the flow.

4.3.3 Perturbation of the air flow

Fig. 4.4 shows a CFD result of the air flow around the kite. The free stream air speed is $v_{a,farfield} = 32,15\frac{m}{s}$, the angle of attack with reference to the kite's center chord is $\alpha_{farfield} = 14°$. Dark blue indicates areas where local air speed is more than 10% lower than $v_{a,farfield}$, dark red indicates areas where local air speed is more than 10% higher than $v_{a,farfield}$.
Measuring flow velocity below the kite inside the C-shape of the wing would inflict a high installation error (see Fig. 4.4b). From Fig. 4.4a it is apparent that one should go either far below the kite's center chord or to the front of the wing to measure an airspeed magnitude that is close to the free stream value. Measuring airspeed at the tips could also deliver good results with a small installation error as derived from Fig. 4.4b. Both options are used on aircraft, a wingtip installation can be seen in Fig. 4.3a but pose problems for a flexible wing as there is no rigid structure to mount a long boom.

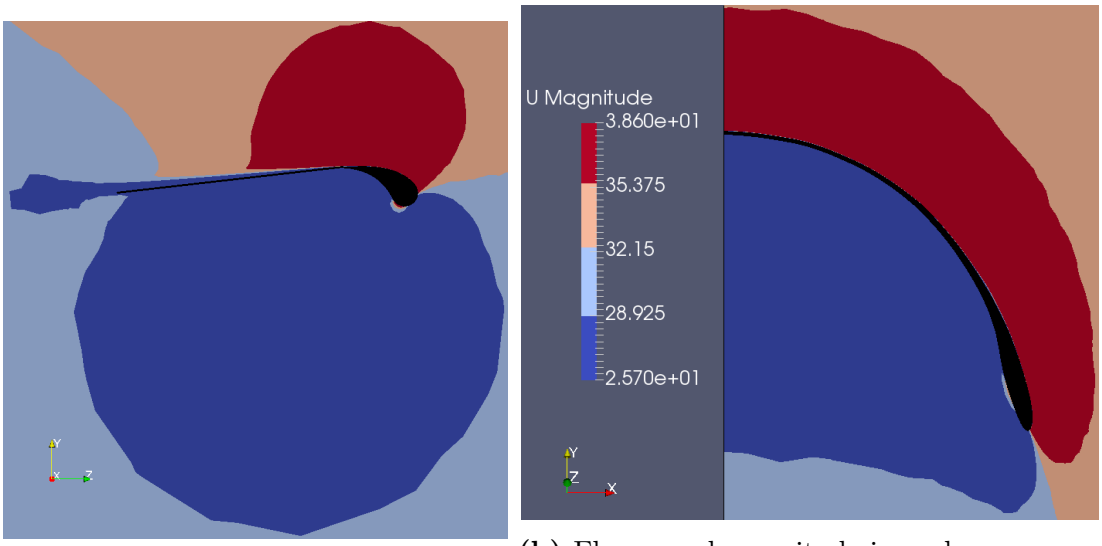

(a) Flow speed magnitude in the kite's symmetry plane

(b) Flow speed magnitude in a plane perpendicular to $V_{a,farfield}$ through 0,25c of center chord

Figure 4.4: Deviation from farfield flow velocity $v_{a,farfield}$ in proximity of the kite (from [6])

Figure 4.5 shows the angular deviation γ of the local flow vector $V_{a,local}$ with respect to the flow vector of the unperturbed air $V_{a,farfield}$.

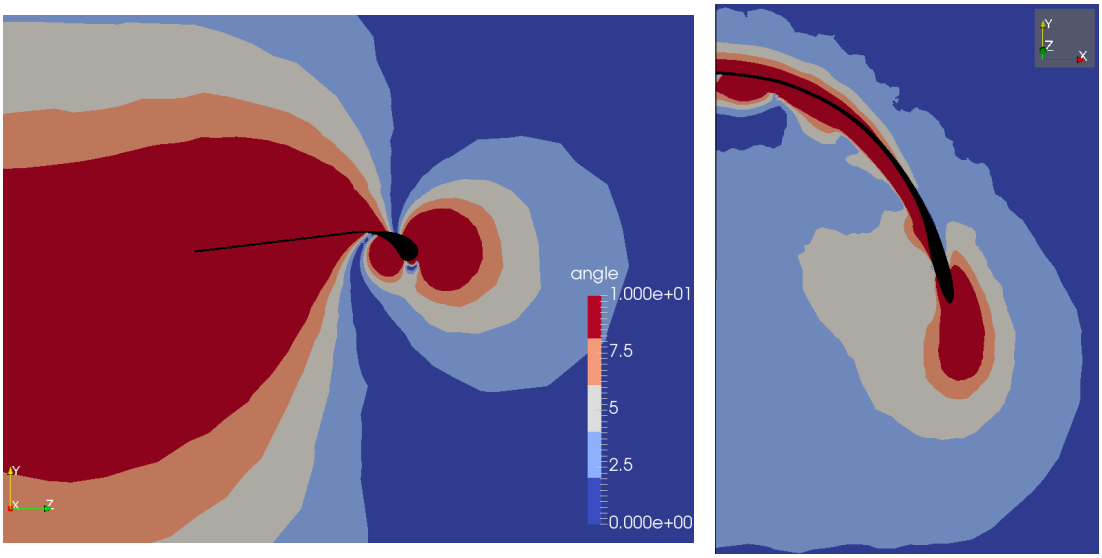

(a) Flow vector's angular deviation from unperturbed flow in the kite's symmetry plane

(b) Flow vector's angular deviation in a plane perpendicular to $V_{a,farfield}$ through 0,25c of center chord

Figure 4.5: Angular deviation from unperturbed farfield flow vector $V_{a,farfield}$ in proximity of the kite (from [6])

The angular deviation γ is calculated by using the scalar multiplication

$$V_{a,farfield} \odot V_{a,local} = cos(\gamma) \times |V_{a,farfield}| \times |V_{a,local}| \tag{4.1}$$

of the local flow vector $V_{a,local}$ with the flow vector of the unperturbed flow $V_{a,farfield}$. For the CFD-calculation both vectors are known. Red areas indicate angular deviations of $\gamma \geq 8°$, dark blue indicates deviations of $\gamma \leq 2°$ thus areas where sensing the inflow angle of the apparent flow appears promising.
Half a chord length in front of the center chord deviations range from $\gamma = 4 - 8°$. An air data boom in front of the kite should have a length of roughly one chord length in order to cut the installation error of the measurement below $\gamma = 4°$. The area in front of the wing tips should also be dropped for sensing the inflow angle as large deviations γ occur according to Fig. 4.5b. Consequently the air data boom will be installed 3-4 chord lengths below the kite as can be seen in Fig. 5.1.

Chapter 5

Construction and calibration

Existing air data booms such as in Fig. 4.3 are designed for rigid aircraft. They point into flight direction and are thus vulnerable to a landing that does not occur on a landing gear. The price for the miniature sensor measuring flight speed and two inflow angles in Fig. 4.3b of about 2000$ is another down side of using an existing measurement device. This is why I decided to design and build my own measurement setup.

5.1 Mounting and structure of the measurement assembly

All air data booms do have a rigid mounting. This is required as the inflow angle must be measured relative to a known reference. To allow for a stiff and lightweight assembly a carbon fiber composite tube is chosen as platform to mount all sensors. It will be attached to the power lines as they are the most stable part of the bridle system due to their loading of roughly 1,5 kN during traction phase. The two power lines take the biggest proportion of the kite's aerodynamic force which is controlled to be between 3 and 4 kN during traction phase. The steering lines in the back bear only a small force and are therefore usually slack during flight (see Fig. 6.2).
The position of the sensors is shown in Fig. 5.1 and will be about three to four chord lengths below the kite to measure the real free stream parameters away from the local influence of the kite as discussed in Sect. 4.3.3. The distance to the KCU which also deflects the air flow is about one meter (see Fig. 5.3b.
As the power lines connect to the front of the kite and steering and depower lines connect to the trailing edge there will be no interference of the sensors with the steering lines as can be seen in figure 5.1a. This would cause severe problems as any contact or entanglement of the steering lines with the measurement setup could destroy the setup or render the kite uncontrollable.
In order to allow a stable reference of the assembly it has to be fixed in at least three points to avoid any free rotation. As shown in Fig. 5.1b the two power lines have a V-shape. They connect in one point with the single line main tether below

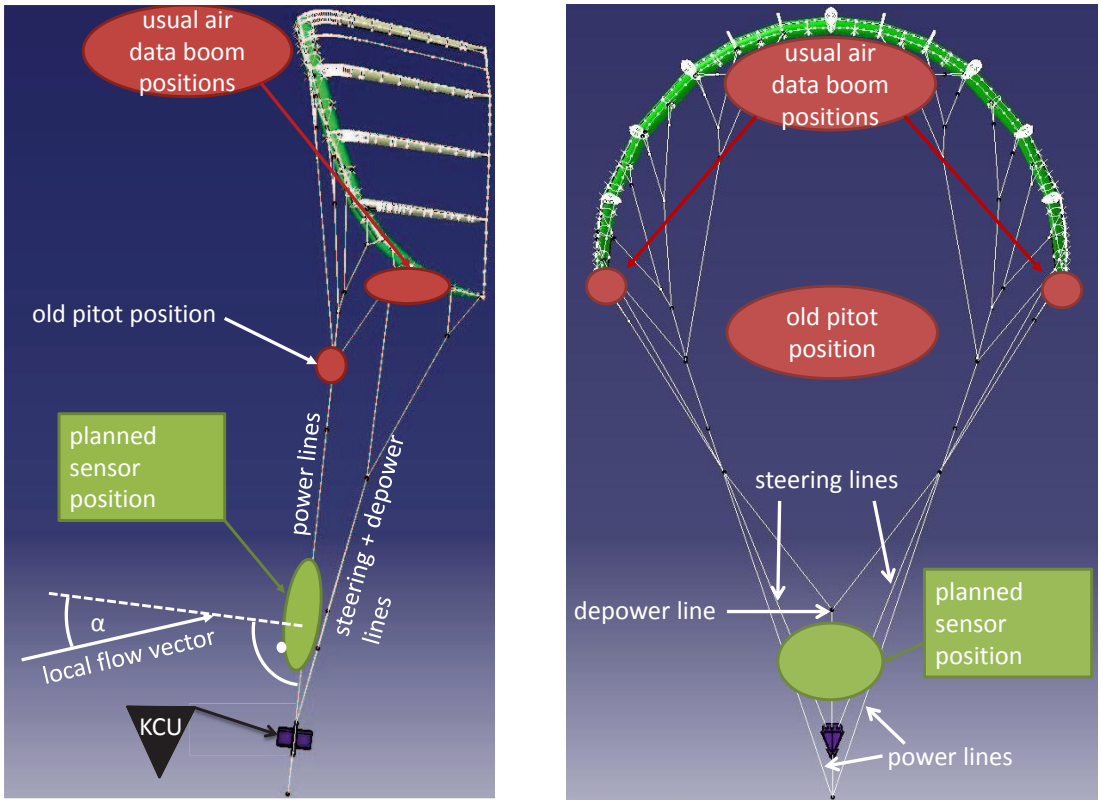

(a) Side view **(b)** Front view

Figure 5.1: Sensor position in the bridles below the kite and definition of inflow angles

the KCU and open up towards the tips of the kite. About 1 m above the KCU their distance to each other is about 80 cm which allows to mount an assembly which connects both power lines. In order to have a symmetric assembly that does not have a bias to any side a mechanical frame is chosen that connects in two points to both of the power lines. The inflow angles are defined towards the normal vector of the plane made up by the power lines as shown in Fig. 5.1a and Fig. 5.2. This is an advantageous reference as the measurement setup is mounted in exactly this plane.
Although the choice of reference system is mainly due to its simplicity and to avoid later correction it is deemed a better option then relating the inflow angles to the kite, for example to its center chord. As can be seen in Fig. 5.2 the orientation of the kite's center chord indicated by the power ratio angle ϵ varies with the power ratio PR. For the $25m^2$ V3-kite used in this test flight the correlation between the power ratio angle ϵ which describes the pitch of the kite's center chord and the power ratio is unknown. Further is the kite deformation due to different loading and the span-wise variation of the local chord's orientation during flight unknown.

The chord of the kite can therefore hardly be used as a reference. This is why the measured angle α will be referred to as inflow angle and not angle of attack. The sideslip angle β is defined as the inflow angle from left or right side towards the normal vector on the plane of the power lines in a way similar to *alpha*. If the sideslip angle *beta* indicates flow coming from the right side it has a positive value, α is positive when the flow comes from a downward direction as shown in Fig. 5.2.

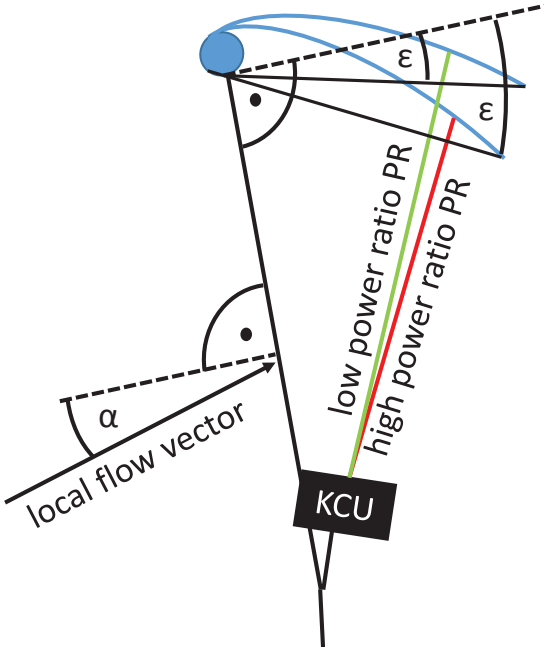

Figure 5.2: Definition of the inflow angle α and the power ratio angle ϵ [17]

Fig. 5.3 shows a drawing of the mechanical frame mounted in the power lines as well as a picture of the measurement setup on the field test right before launch. In Fig. 5.3b one can see that for the real flight the lowest part of the mounting frame for the sensors is about two and a half feet or 0,75 meters above the KCU which can be seen at the bottom of the picture in black color. The distance between the lowest sensor and the KCU is thus about one meter which should be enough to avoid the sensing of any flow perturbation of the KCU. This distance is little more than what was expected after looking at the drawing in Fig. 5.3a which is due to a smaller opening angle of the V-shaped power bridles with respect to the value in the CAD-drawing.

5.2 Pitot tube

The Pitot-static tube used is originally intended for model aircraft. The complete measurement unit with differential pressure sensor, temperature sensor and Pitot

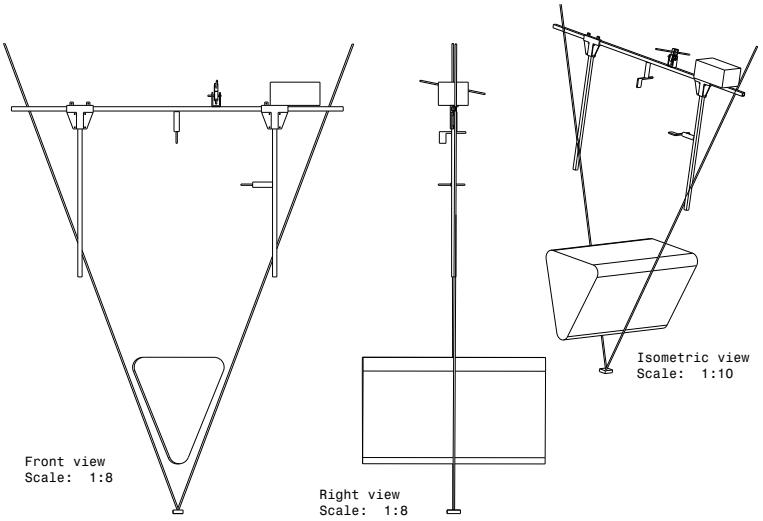

(a) Drawing of the installed setup

(b) Installed measurement setup prior to test flight

Figure 5.3: Sensor setup mounted in the bridles above the KCU

tube comes from unmanned tech company and costs around 60 Euros. It provides measured differential pressure with $size_{\Delta p} = 14bit$ and temperature with $size_T = 11bit$ at a frequency of $f_{\Delta p} = 10Hz$ via a I2C bus to the Pixhawk microcomputer. The range of the differential pressure sensor is $range_{\Delta p} = 1psi = 6895Pa$, the resolution is $resolution_{\Delta p} = 0,84Pa$ according to

$$resolution = \frac{range}{2^{size-1}} \tag{5.1}$$

. The new Pitot tube is a response to the poor data quality of the old airspeed measurements. Fig. 5.4 shows both the new and old Pitot-static tube.
The new Pitot tube is much closer to an optimal measurement device as in [2] where the holes for sensing the static pressure should be several tube diameters behind the tip. It also eliminates the problem of leakage mentioned in [8] as it uses another measurement method. The MS4525DO sensor measures the deformation of a membrane due to a pressure difference to obtain the differential pressure instead of measuring a leakage flow.
In order to measure flow magnitude independent of the inflow angle, the Pitot tube is mounted on a finned pivotable beam that aligns with the flow as pictured in Fig. 5.9. By changing from a drag shuttle to a vane that uses lift to align with the flow the problems of misalignment at small velocities and measuring errors because of the flow deceleration upstream of the drag shuttle are addressed. A lift vane has a bigger arm of leverage even at low angles of misalignment and has a much smaller effect of flow perturbation upstream of it. The accuracy

Figure 5.4: New (left) and old (right) Pitot-static tube

and calibration rule for the airspeed measurement sensor as well as its yawing sensitivity is evaluated in Sect. 5.5.1.

5.3 Angle measurement

The angular measurement system is composed of two main elements, the wind vane and a AS5043 rotary position sensor (Appendix A) connected by a shaft. The data sheet claims that the sensor has a resolution of $resolution_\xi = 0,35°$. The sensor can provide a digital or analog signal. We use the analog one which provides a voltage signal that varies from zero to half the supply voltage for angles from 0-360 degrees.
Fig. 5.5 shows drawings of the wind vane assembly with some dimensions in mm. All mechanical parts but the bearings and shaft are 3D-printed. The bottom part will be clamped onto the squared carbon tube of the main structure which is 13 mm wide. The dimensions of the assembly without the vane are only $4x4x3cm^3$ as seen in Fig. 5.5b.
The working principle of the sensor is that Hall sensors trace the rotation of a magnet which is glued onto the main shaft and thus connected to the wind vane which aligns with the local flow vector. The shaft is machined from non magnetic steel to avoid interference with the magnetic field of the main magnet. The magnet's position should be very well determined, its axis should be aligned with a precision of 0,25 mm towards the axis of the detecting sensors. For the details on sensor position and a drawing of the main shaft refer to appendix A and B.

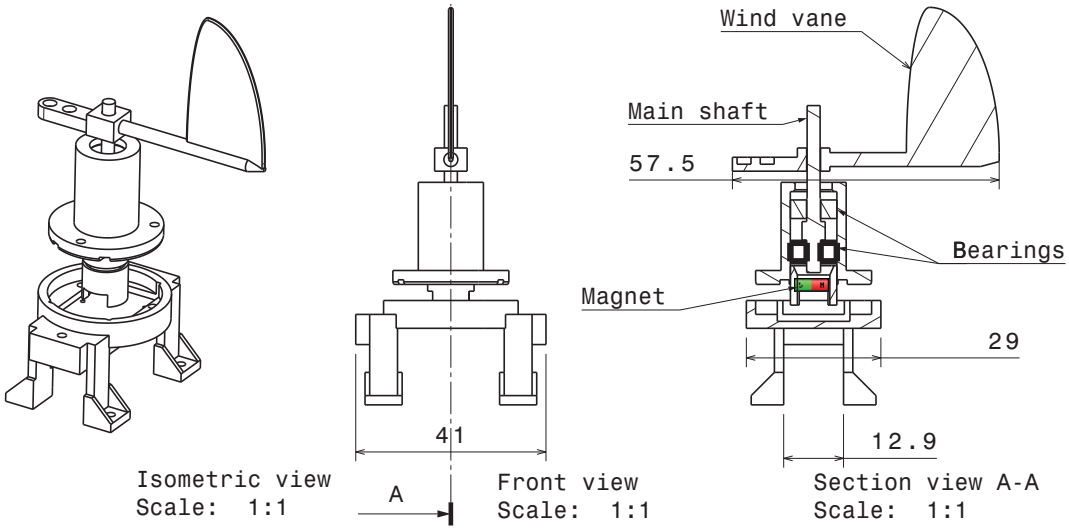

(a) Isometric view of the entire windvane assembly

(b) Front and section view of the windvane assembly

Figure 5.5: Assembly for angular measurement

Fig. 5.6 shows the different parts of the wind vane assembly. Most structural parts as well as the vane are 3D-printed. That way all holes for assembly, and even openings for the Printed Circuit Board (PCB) and electrical connections can already be included into the design (see 5.6a).

For the assembly, first the sensor itself (size SSOP16), is soldered onto a fitting PCB. The PCB with sensor can then be mounted onto the 3D printed bottom part. The bearings are attached to the main shaft and the magnet is glued at the end face of it (Appendix B). The electrical connections including two capacitors for buffering should be soldered according to (Appendix A). An attachment point for a cable with power supply, ground and signal is installed as in Fig. 5.6c.

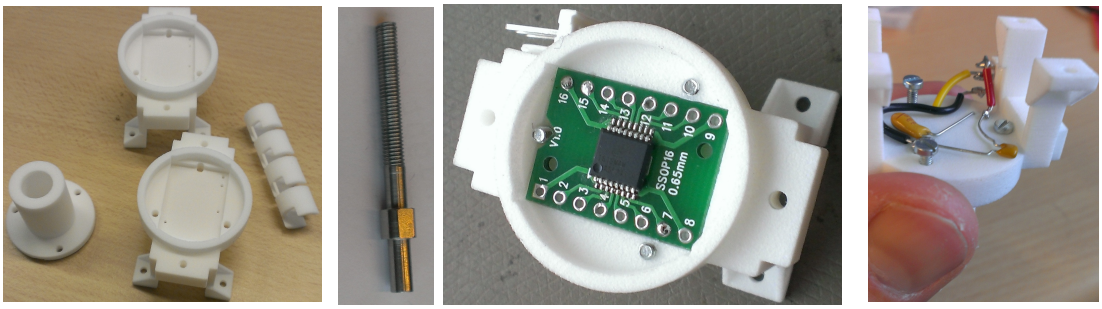

(a) 3D-printed parts of windvane assembly

(b) Main shaft to mount the magnet and sensor mounted on the PCB

(c) Electrical connections

Figure 5.6: Mechanical and electrical components of the windvane assembly

After making sure that all connections are good, the three 3D-printed structural parts and the shaft with magnet and bearings should be assembled as in Fig. 5.5b. After tightening the three M2-screws pictured in Fig. (5.6b, 5.6c) and connecting the vane to the thread on top of the main shaft, the assembly for flow angle measurement should be operational and look like the one in Fig. 5.7. To avoid any perturbing influence of gravity or accelerations on the flow direction sensing some soldering tin is attached to the front part of the vane as a counterweight.

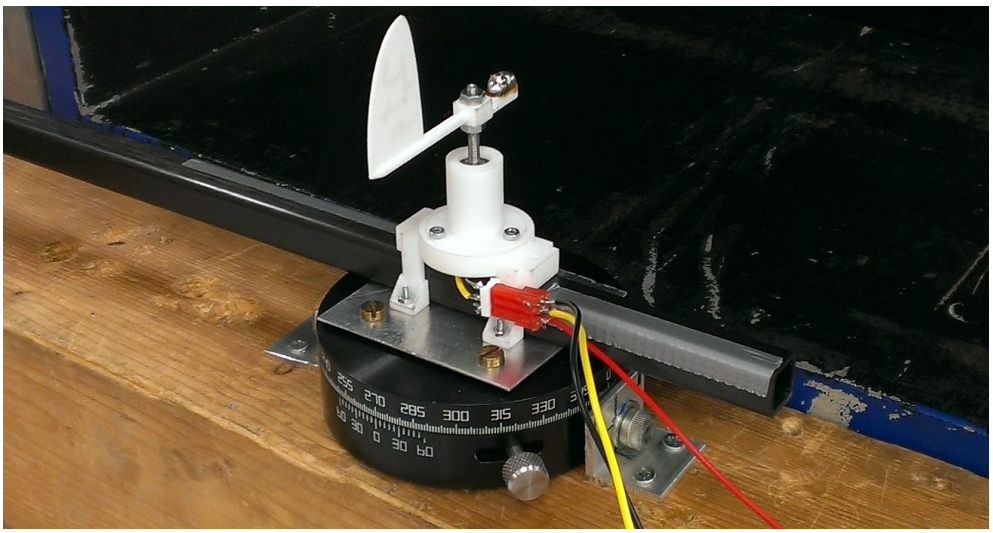

Figure 5.7: Wind vane assembly for angular measurement mounted in the wind tunnel

5.4 Data transfer and sensor platform

In order to process the measured data and transmit it to the KCU and ground station a Pixhawk microcomputer is used. It can read airspeed data through its Inter-Integrated Circuit (I2C) serial interface and has two inputs for an analogue voltage signal of 3,3 V. There are six different variables of interest throughout the flight:

- Differential pressure Δp_{pitot}
- Barometric pressure $p_{measured}$
- Air temperature $T_{measured}$
- Reference voltage U_{ref}
- Voltage for sideslip angle U_1

- Voltage for vertical inflow angle U_2

The sensor data is transmitted via antennas to the KCU and from there to the ground station. That way it can be ensured that all data sets are always logged simultaneously so there is no need for additional synchronization. Another advantage of the instantaneous transmission is that data is saved on the ground once it is sent an can therefor not get lost during a later crash.
In theory it would even be possible to use the live-data acquired for kite control but this is not intended. In order to keep the amount of data transmitted as small as possible, only the six variables of interest are sent out from the Pixhawk computer. The software of the Pixhawk is further modified to keep the output voltage U_{ref} at a constant level.

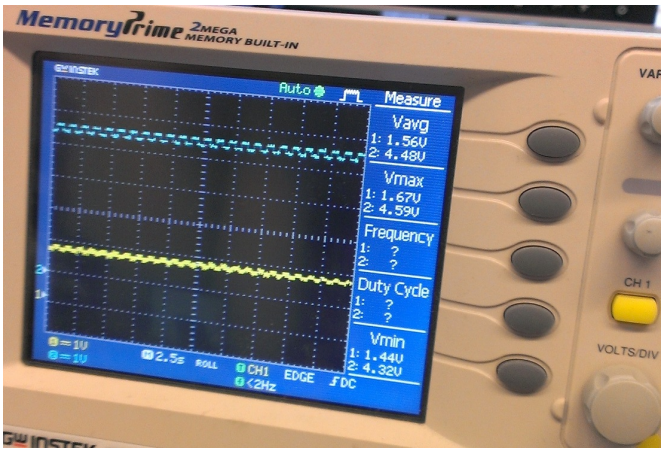

Figure 5.8: Measured oscillation of supply voltage and signal voltage due to current drawn by other consumers

Fig. 5.8 shows the oscillation of the supply voltage the Pixhawk microcomputer supplies to the wind vanes as well as the oscillation of the analog signal of the measured angle which is ratiometric to the supply voltage. For both voltages we see a repeating pattern with a constant frequency of one Hertz. The supply voltage drops every second from its maximal value of 4,59 V down to 4,32 V which results in a noisy signal for the measured angle.
This oscillation is due to a bright LED which blinks with a frequency of 1 Hz during operation with the standard Pixhawk firmware. For our flight test we disable the blinking of this LED and use a power bank that supplies a slightly higher voltage than during the ground test pictured in Fig. 5.8. By doing so we obtain a roughly constant supply voltage of $U_{ref} = 4,65V$ as shown in Fig. 6.9.
The Pixhawk microcomputer and its autonomous power supply as well as antennas are housed in a plastic box to protect them from rainwater and crash as can be seen in Fig. 5.9 on the right side. The battery with a capacity of 5000 mAh should give the measurement setup an autonomy of several hours, which is longer

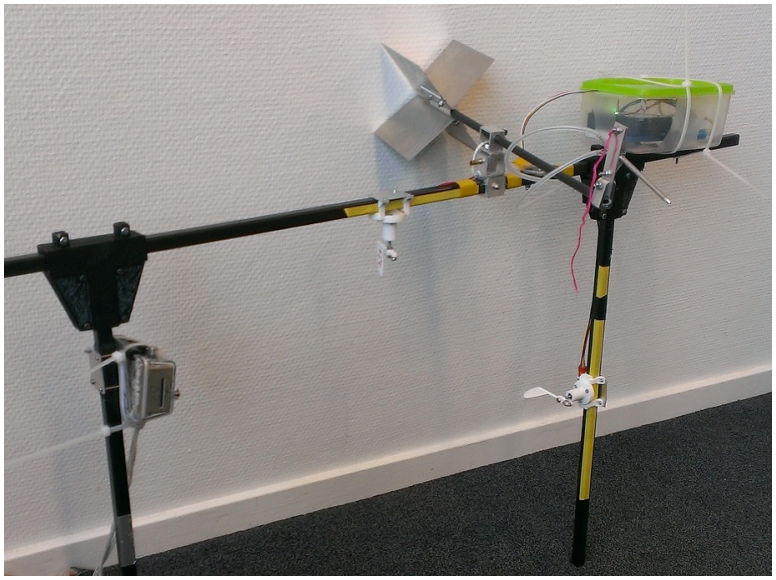

Figure 5.9: Complete measurement assembly with pivotable Pitot tube, two wind vanes, data processing unit and camera

than the autonomy of the kite itself which is limited to about two hours because of the batteries that supply the KCU.

5.5 Calibration and expected measurement error

This section explains how the measured quantities are transferred into the intended variables and which measurement errors we assume. Only errors arising from the measurement method are thereby considered. Installation errors that originate from the deviation of the measured local flow towards the free stream cannot be quantified as we are currently lacking an accurate model that could predict the local flow around the kite. The installation error is considered small as the position with the expected minimal installation error is chosen for the measurement (see Sect. 4.3).

5.5.1 Airspeed magnitude

To calculate air speed from the differential pressure Δp which is measured by the Pitot-static tube Bernoulli's law for energy conservation is used:

$$p_s + \frac{\rho}{2} v_a^2 = p_t \Leftrightarrow p_t - p_s = \Delta p = \frac{\rho}{2} v_a^2 \tag{5.2}$$

Gravitational influence is neglected because of the low density of air. The Pitot-static system measures the difference between total pressure p_t and static pressure

p_s directly. However the sensed pressure Δp_{pitot} is not exactly the differential pressure of the air flow Δp.
Firstly does the used Measurement Specialties 4525DO pressure sensor have an offset that originates from its sensing method. This offset value can be found by noting the sensed differential pressure at zero wind conditions such as in any closed room or a wind tunnel that is turned off. The so measured differential pressure Δp_{pitot} must then be subtracted from all measured values. Secondly there is an error induced by the mounting of the Pitot tube. Due to the decelleration of the flow upstream of the measurement assembly the static pressure increases slightly and sensed differential pressure thus decreases according to Eq. 5.2 [2]. The suggested calibration law to link measured differential pressure Δp_{pitot} to the actual differential pressure in the local flow is thus:

$$\Delta p = \frac{\Delta p_{pitot} + \Delta p_{offset}}{k_{\Delta p}} \tag{5.3}$$

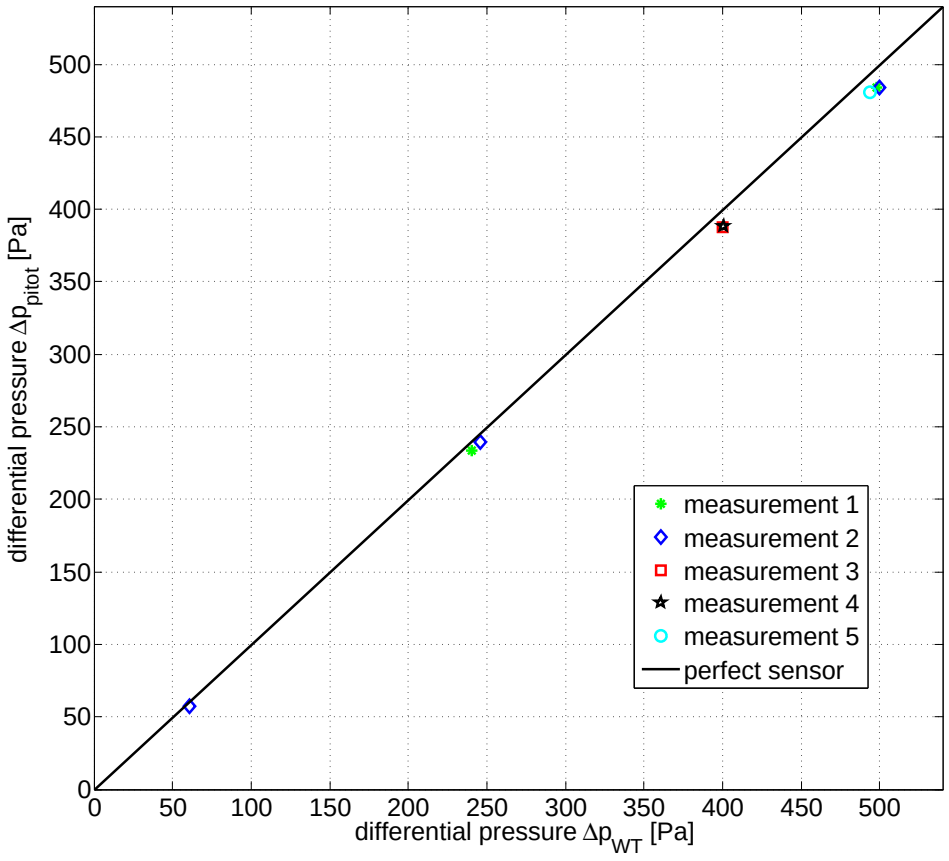

Figure 5.10: Measured differential pressure by the Pitot-static system

The offset value Δp_{offset} has to be determined for every measurement separately. For most measurements in the wind tunnel the value was about $\Delta p_{offset} = -50Pa$. It is assumed that the error in calibration is $\pm 10Pa$ according to Sect. 6.1, this value can however be reduced by using the correct calibration procedure during the flight test. The scaling factor $k_{\Delta p}$ is found to be $k_{\Delta p} = 0,971$ for the best results using least squares fitting method. Fig. 5.10 shows the difference between measured differential pressure from the Pitot tube corrected for the offset and free stream differential pressure p_{WT} obtained from the wind tunnel's measurement system. Δp_{pitot} is always about 3% lower than the free stream value and thus has to be corrected by applying the scaling factor $k_{\Delta p}$.
In order to calculate apparent flow speed v_a from the differential pressure air density must be known (see Eq. (5.2)). Air density ρ calculates from air temperature T and barometric pressure p according to the law for an ideal gas

$$\rho = \frac{p}{RT} \tag{5.4}$$

with $R = 287,06\frac{J}{kgK}$ being the specific gas constant for dry air. Both air temperature and barometric pressure are measured by the built measurement assembly and should be calibrated. For the barometric pressure the best correction found is

$$p = p_{measured} + p_{offset} \tag{5.5}$$

to correlate measured barometric pressure with the real value obtained from a calibrated pressure clock. Fig. 5.11 shows that the measured value is always higher than the actual pressure. The best fit is achieved for a value of $p_{offset} = -370Pa$. By comparing the measured pressure values with the reference manometer we obtain an uncertainty in the pressure measurement of $\delta p = \pm 60Pa$ taking into account the maximal measured deviation from the calibration rule in Fig. 5.11.

For the temperature the procedure is similar. The measured value for the temperature is compared to the thermometer of the wind tunnel in Fig. 5.12. The measured value lies below the actual temperature for all measurements and shows roughly the same offset value. The suggested correction rule to correlate measured air temperature to the actual value is similar to the one used for the barometric pressure

$$T_{calibrated} = T_{measured} + T_{offset} \tag{5.6}$$

with a value of $T_{offset} = 0,75K$ for an optimal calibration. The uncertainty in the temperature measurement is $\delta T = \pm 0,40K$ taking into account the maximal measured deviation from the calibration rule in Fig. 5.12.
According to the data sheet the differential pressure sensor has a total error band of $TEB_{\Delta p} = \pm 1\%$. Additionally there is an error if the Pitot tube is not

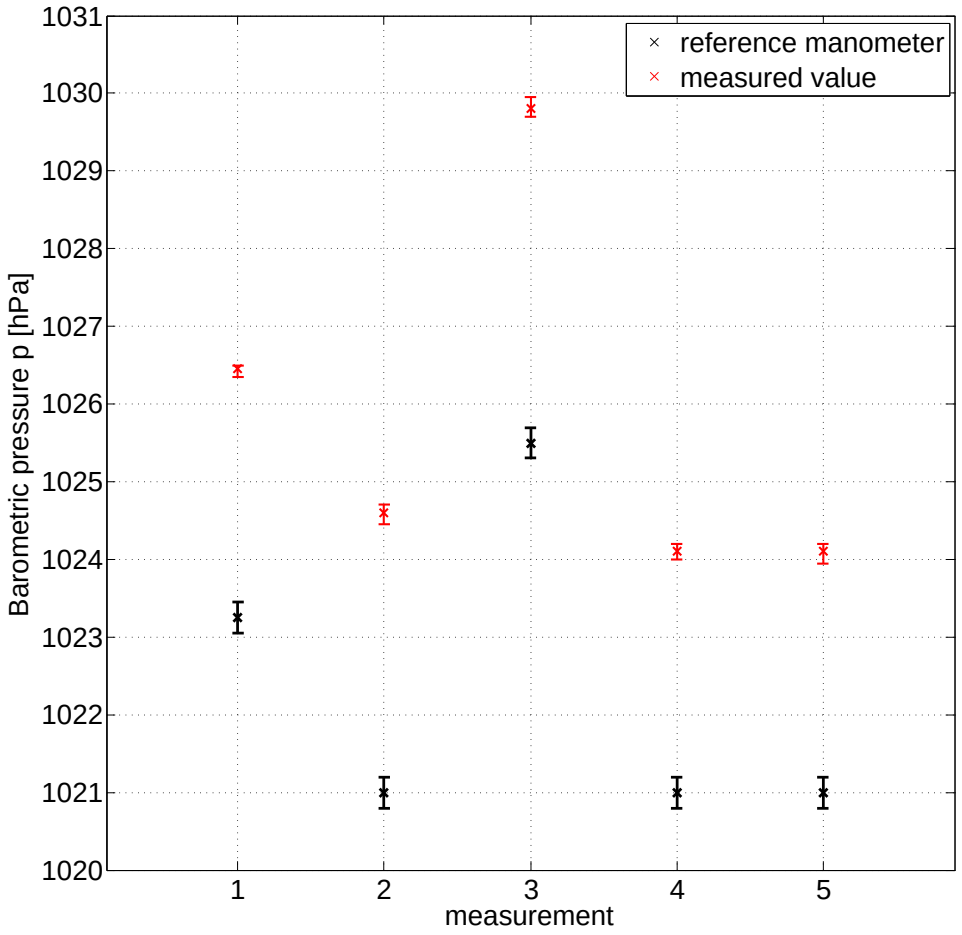

Figure 5.11: Measured barometric pressure compared to the wind tunnel reference

aligned perfectly with the flow. Fig. 5.13 shows the variation in sensed differential pressure. As there is an obvious bias on one side, the measurement is repeated and it is found that the bias is due to an imperfect non symmetric Pitot tube. Depending on how the Pitot tube is mounted a high sensed differential pressure would occur during yawing either to the left or to the right side.

Fig. 5.13a shows the sensed differential pressure for a yawing angle of $\beta_{pitot} \in [-25°; 25°]$ with the Pitot tube mounted in a way that the attachment point for the static pressure tube points upwards. Fig. 5.13b shows the same plot for the Pitot tube mounted reversely with the static pressure tube connection facing down.
The measurement signal is not symmetric with respect to the indicated yawing

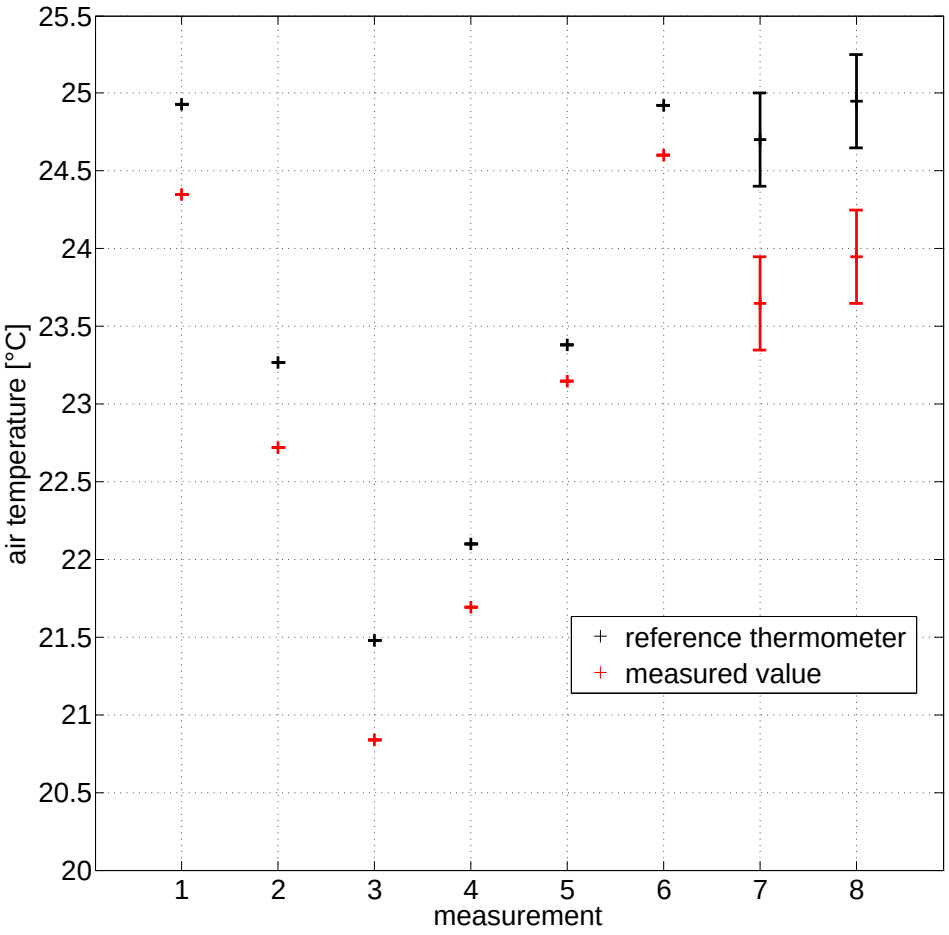

Figure 5.12: Measured air temperature compared to the wind tunnel reference

angle but off centered by about $1,5°$ which is probably due to imperfect mounting of the Pitot tube. The dashed line indicates a sensed differential pressure signal which is a function of the cosine of the yawing angle. The Pitot tube is giving a signal that is close to a cosine function, especially for yawing angles above $\beta_{pitot} = 15°$.
The oscillations in the blue smoothed pressure signal are due to the measurement technique where after 5 seconds of measurement the Pitot tube is turned for one degree by hand. This results in a small drop in sensed differential pressure at every one degree as the hand used to turn the Pitot tube blocks the flow and increases static pressure upstream where the Pitot-static tube has its static pressure port.
Fig. 5.14 shows the error in the measured differential pressure Δp_{pitot} that is caused by the misalignment of Pitot tube and airflow. Π is the fraction of the

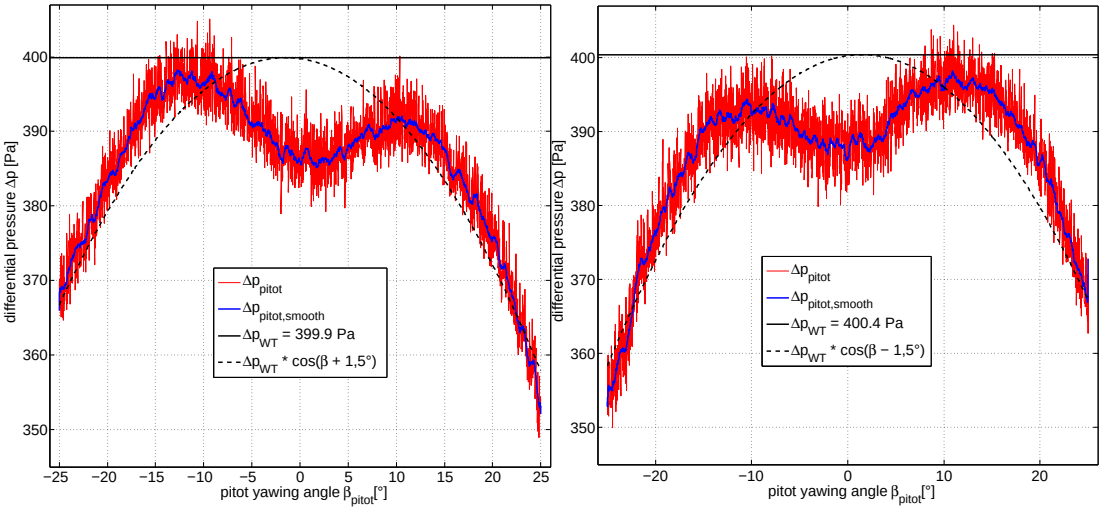

(a) Side view **(b)** Front view

Figure 5.13: Yawing effect on differential pressure measurement

real differential pressure p_{WT} that is indicated by the Pitot-static measurement. For a Pitot-tube that aligns itself with the airflow as in our assembly we assume an uncertainty of $\Delta\beta_{pitot} = \pm 3°$ due to imperfect installation and time delay of the alignment mechanism.
The sensed differential pressure ratio in that case lies in an interval of $\Pi \in [0,967; 0,977]$. Assuming an uncertainty of $\Delta\beta_{pitot} = \pm 15°$ for a case where we do not align the Pitot tube with the flow we obtain values for the ratio of indicated differential pressure in the range $\Pi \in [0,965; 0,994]$.
Installing the Pitot tube in a fixed way will thus result in an error of 3% instead of 1% for the aligned tube. The scaling factor $k_{\Delta p} = 0,971$ should in the case of a not aligned assembly also be adjusted. Assuming that the inflow angle with respect to the Pitot tube is equally distributed in the interval of $\beta_{pitot} \in [-15°; 15°]$ the average scaling factor should be rather $k_{\Delta p,not-aligned} = 0,979$ than $k_{\Delta p} = 0,971$ for the aligned case.
The error of the obtained value for the apparent flow velocity is calculated according to

$$\Delta v_a = (v_{a,+} - v_{a,ref}) \tag{5.7}$$

$$v_{a,+} = \sqrt{2R \times \frac{((1 + TEB_{\Delta p}) \times 1,005 \times 245,0Pa + 10Pa) \times (288.15K + 0,4K)}{101325Pa - 60Pa}} \tag{5.8}$$

where for the calculation of $v_{a,+}$ all maximal measurement errors that would increase airspeed are used.
The reference case is standard atmosphere at sea level with $T_{ref} = 288,15K$,

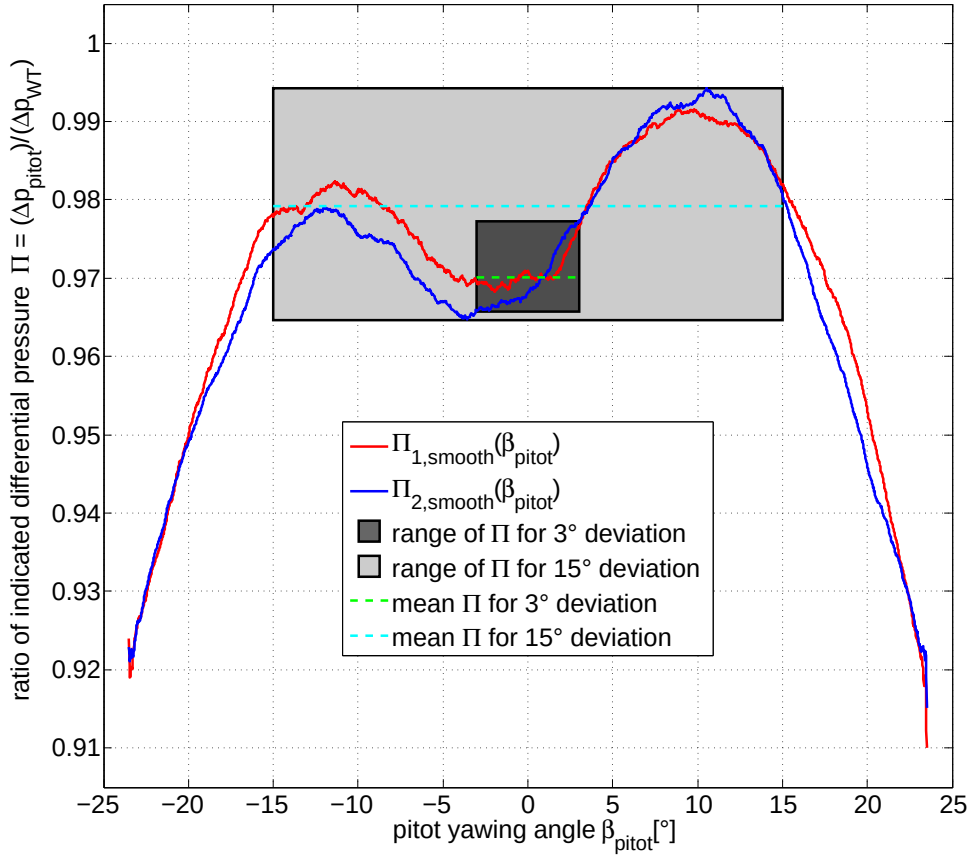

Figure 5.14: Measurement error due to uncertainty in Pitot tube misalignment

$p_{ref} = 101325Pa$ and a true flow velocity of $20\frac{m}{s}$. $\Delta p = 245,0Pa$ is the differential pressure that would correspond to a flow velocity of $v_{a,ref} = 20\frac{m}{s}$. Calculated uncertainty of apparent flow velocity is $\Delta v_a = 0,57\frac{m}{s}$ for a reference of $v_{a,reference} = 20\frac{m}{s}$. The biggest contribution to the error is the uncertainty in the calibration which could be improved easily in the future. For a reference value of $v_{a,ref} = 10\frac{m}{s}$ the error is $\Delta v_a = 0,86\frac{m}{s}$. This is due to the higher importance of the 10 Pa offset error compared to an actual differential pressure of $\Delta p = 61,25Pa$.

5.5.2 Wind vanes

The wind vanes are calibrated by measuring the voltage ratio at an angle of $-90°$ and $+90°$ towards horizontal inflow. As the voltage signal varies linearly with the angle, any value between both voltages can be related to its according angular deflection of the vane. As the kite always flies forward, we will only have angles in a range of 180 degrees, in reality we expect an even smaller interval for the inflow angles of less than $\pm 30°$. That way we can always mount the wind vanes in a way that the angular position where voltage would drop from maximum to zero does never occur during flight.
Voltage signal U_{signal} according to (Appendix A) is given by

$$U_{signal} = \frac{U_{ref}}{2} \times \frac{\xi}{360°} \tag{5.9}$$

where $U_{ref} \approx 4,65V$ is the supply voltage of the Pixhawk microcomputer and ξ is the turning angle of the magnet with respect to the Hall sensor's zero position. The reference voltage U_{ref} varies by $\pm 1\%$ due to the current drawn by other consumers of the Pixhawk microcomputer (see Sect. 6.3). This is why it is necessary to monitor and log also the reference voltage to determine the angle of the vane during flight.
The supply voltage always stays within the limits $4,5V \leq U_{ref} \leq 5,5V$ as required by the sensor. The signal voltage will therefore always stay between $0V \leq U_{signal} \leq 2,75V$ and thus can be read by the Pixhawk's 3,3 V ADC port.

The calibration rule for the vane measuring sideslip angle is

$$\beta = (0,222513 - \frac{U_1}{U_{ref}}) \times \frac{180°}{0,24736} \tag{5.10}$$

where the proportion of signal voltage for a sideslip angle of $\beta = 0°$ to reference voltage is $\frac{U_1(\beta = 0°)}{U_{ref}} = 0,222513$. The proportion of signal voltage difference for a 180° turn to the reference voltage is $\frac{U_1(\beta = 90°) - U_1(\beta = -90°)}{U_{ref}} = 0,24736$.
β has a positive value if the flow is coming from the right side with respect to the kite's forward direction.

The calibration rule for the vane measuring vertical inflow angle is

$$\alpha = (\frac{U_1}{U_{ref}} - 0,303865) \times \frac{180°}{0,252629} \tag{5.11}$$

where the proportion of signal voltage for horizontal inflow to reference voltage is $\frac{U_1(\alpha = 0°)}{U_{ref}} = 0,303865$. The proportion of signal voltage difference for 180 degrees

of traveling to the reference voltage is $\frac{U_1(\alpha = 90°) - U_1(\alpha = -90°)}{U_{ref}} = 0,252629$.
α has a positive value if the flow is coming from the down side with respect to the kite's forward direction, thus when there is a positive angle of attack.
The calibration of the wind vanes is not perfect. Firstly the position of +90 or -90 degrees is determined visually, by aligning the end of the wind vane with the middle of the mounting structure as seen in Fig. 5.15.

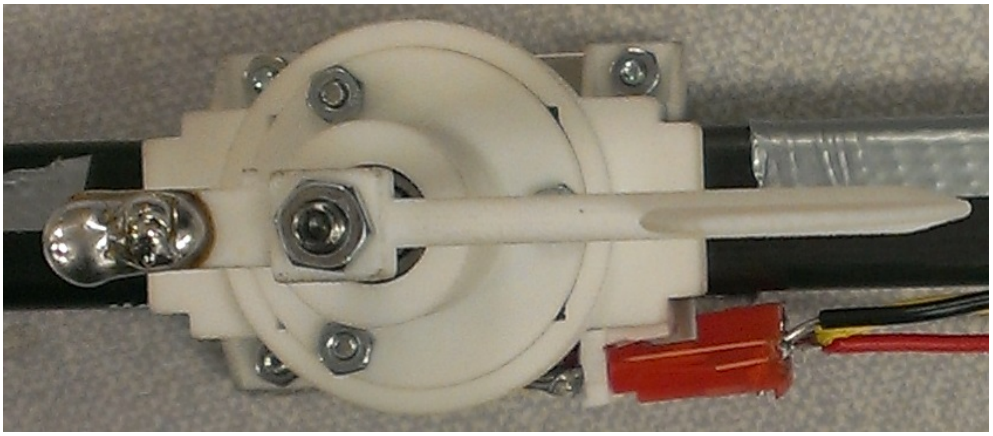

Figure 5.15: Calibration of the wind vane

The uncertainty is assumed to be $\pm 0,5mm$ which for a distance from end to pivot of the wind vane of 40mm means an angle of $0,72°$.
In order to determine the accuracy of the angular measurement the sensor is mounted on a turning table in the wind tunnel as in Fig. 5.7. The orientation of the assembly is then changed in an interval from zero to 180 degrees with 29 measurements taken at different angular positions. The matlab method polyfit which uses the method of least squares is used to find a relation between voltage signal and angle. To calculate standard deviation we use

$$\sigma_U = \sqrt{\frac{1}{29}\sum(U_{signal} - U_{polyfit})^2} \tag{5.12}$$

which gives us a value of $\sigma_U = 1.89mV$. Using the relation of angle to signal voltage found by the polyfit function which says that 6,40 mV correspond to one degree we obtain a standard deviation of the calculated angle of $\sigma_\alpha = 0,30°$. The maximum deviation of $U_{signal} - U_{polyfit}$ is 3,94mV which means an angular error of $0,62°$.
For the static misalignment error we want to obtain the maximal stiction torque we have to exceed in order to make the vane turn. When placing the vane perpendicular to the flow, it first moves at a dynamic pressure of $\Delta p = 2,5Pa$. Assuming flat plate drag with $c_{D,plate} \approx 1$, a vane surface of $S_v = 4,935cm^2$ and a leverage arm of $r_v = 0,025m$ we can say that mechanical stiction torque is inferior

to $M_{stiction} = 3,1 \cdot 10^{-5} Nm$.
Assuming an apparent flow velocity of $v_a = 20\frac{m}{s}$ at ISA conditions and thus a dynamic pressure of $\Delta p = 245Pa$ we can calculate the maximal static misalignment by calculating the vane's angle of attack $\alpha_{stiction}$ that is needed to overcome the stiction torque. According to [23] lift induced torque M can be calculated with

$$M = r_v \times qS_v c_{L,vane} \tag{5.13}$$

where $c_{L,vane}$ is the vane's lift coefficient that calculates with

$$c_{L,vane} = \frac{2\pi \times \alpha_v \times AR}{AR + 2} \tag{5.14}$$

. For this calculation we assume small angles. The vane is designed with an aspect ratio of $AR = 2$, an aerodynamic leverage of $r_v = 0,025m$ and a surface area of $S_v = 4,935cm^2$. The minimal angle of attack to overcome stiction torque is thus $\alpha_{stiction} = 0,19°$.
Summing up the uncertainty of the calibration, the maximum deviation from an ideal linear sensor as well as the static misalignment error and the minimal resolution we obtain a maximal uncertainty in the angular measurement of $1,88°$.

Chapter 6

Flight data

The setup was first tested on March 24th 2017 at Valkenburg air base in the Netherlands on a LEI-kite with a projected reference surface of $S = 19,75m^2$ (model V3). Position of the ground station was $lat_{GS} = 52,1691°$, $long_{GS} = 4,4310°$ and an elevation of $alt_{GS} = -5m$ thus below sea level. It was a sunny dry day with good sight and wind mainly from east-northeast direction (see Fig. 2.4).

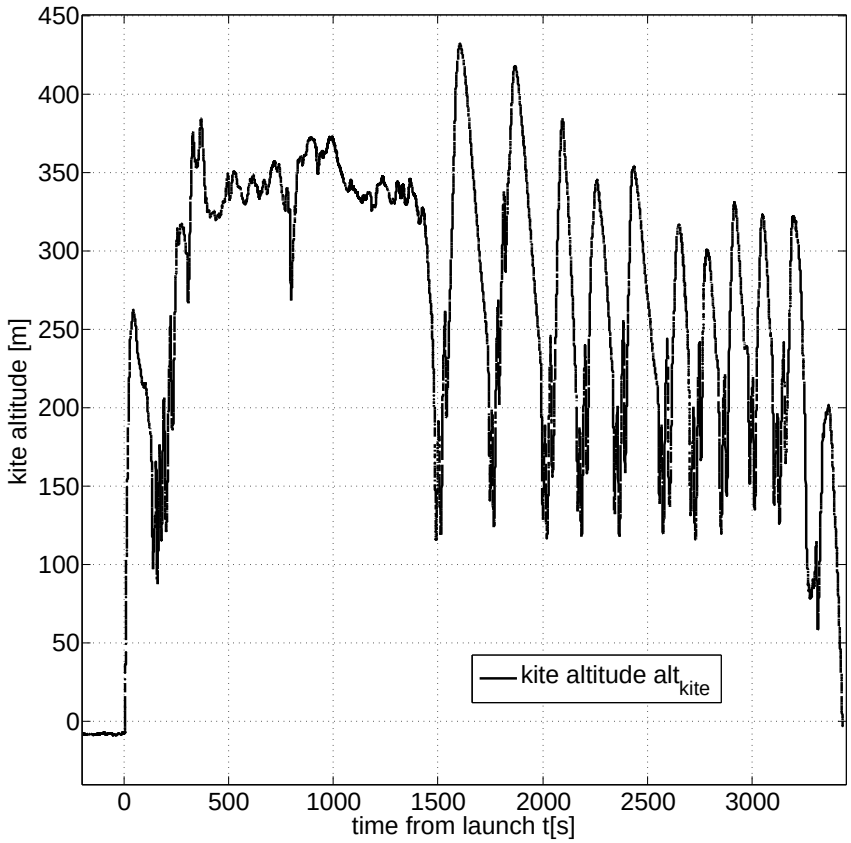

Figure 6.1: Kite altitude throughout the entire flight test

Fig. 6.1 shows the altitude of the kite over the course of the test flight. The time scale is the same for all plots in this chapter with $t = 0s$ being the moment of launching, or more precise the tenth of a second where the reel-in which triggers the kite's liftoff started.
Flight duration was roughly one hour with 10 pumping cycles being flown between $t = 1480s$ and $t = 3230s$. All cycles feature a similar altitude profile and flight path that corresponds to the one explained in Sect. 2.3. They start with the traction phase at a low altitude of around $alt = 120 - 250m$ where altitude varies quickly due to the figure of eight or elliptic pattern flown. The parking and reel-in phase brings the kite up to a higher altitude of $alt = 300 - 430m$ which then decreases due to reel-in.
In the time between launch and $t = 1480s$ the kite was mainly parked at a high altitude in order to allow some mechanical problems at the ground station to be fixed, this is why this period is of minor interest.

Figure 6.2: Picture of the on-board camera 20 seconds after take-off

Fig. 6.2 shows the sensors during the test flight briefly after launch. All three sensors align with the flow and we assume that there is no sensor malfunctioning. Only 20 seconds after take-off the kite flies already more than 200 meters above ground which is in line with the high kite speeds directly after launch plotted in Fig. 6.4.

6.1 Airspeed data validation

In order to validate air temperature and pressure obtained with our measurement assembly in Fig. 6.3 the GPS altitude of the kite alt_{GPS} is plotted over time and compared with the barometric altitude alt_p and the altitude calculated from measured air temperature alt_T. The GPS altitude is measured by the Inertial Measurement Unit (IMU) mounted on the kite. Barometric altitude is calculated by the formula

$$alt_p = -\frac{RT_{mean}}{g} \log \frac{p}{p_0} + alt_0 \tag{6.1}$$

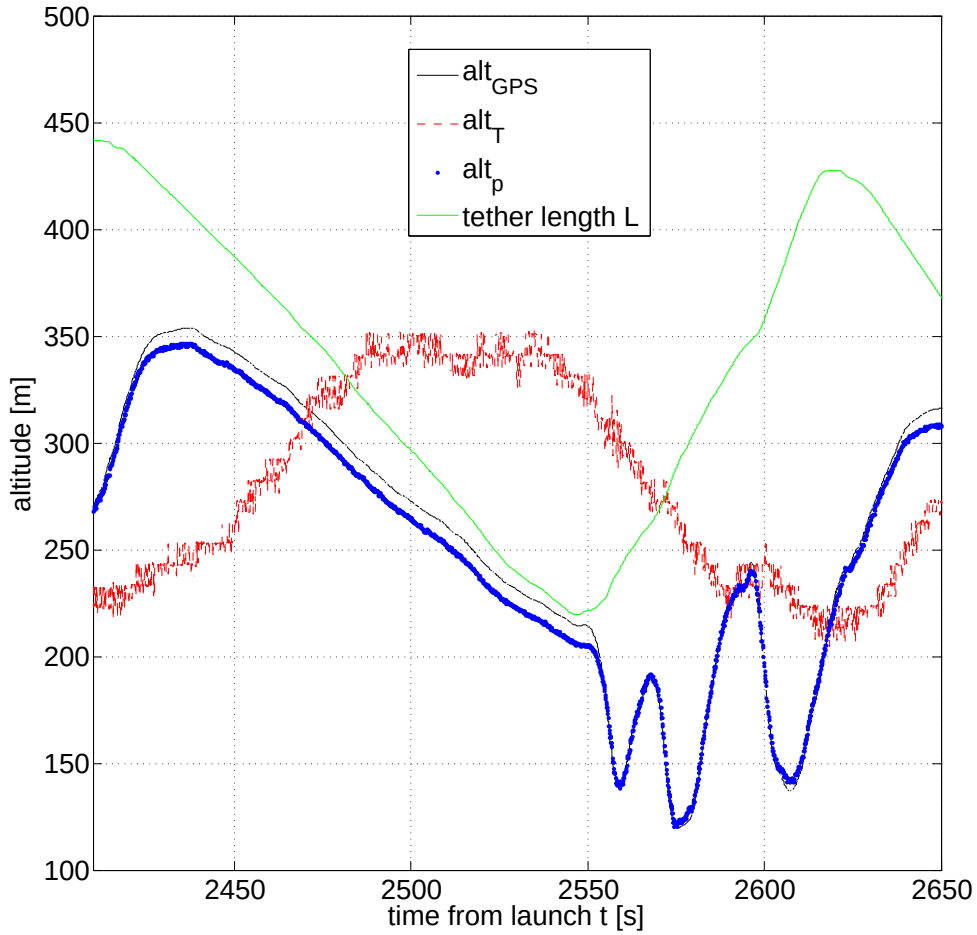

Figure 6.3: Comparison of kite altitude obtained from different sources

with $alt_0 = -8m$ and $p_0 = 102750Pa$ being the initial values for the kite on the ground before launch. $T_{mean} = 286K$ is the average air temperature during the kite's flight.
Fig. 6.3 shows a very good conformity of the kite's GPS altitude alt_{GPS} and the barometric altitude alt_p calculated from the measured air pressure. Throughout the entire flight time of one hour the deviation is limited to a maximum of about 5 meters. Only for the reel-in periods, e.g. from $t = 2420s$ till $t = 2555s$ there is a systematic offset of roughly 10 meters. This originates from the fact that during reel-in the kite flies about 10 meters above the measurement assembly which is installed between kite and KCU. It can be concluded that the suggested calibration law in Eq. 5.5 is valid for all flight situations and both GPS indicated altitude and barometric altitude are very accurate.

For the air temperature a similar approach is followed. Altitude alt_T is calculated from the measured air temperature $T_{calibrated}$ according to

$$alt_T = alt_{ref} + \frac{100m}{K} \times (T_{ref} - T_{calibrated}) \tag{6.2}$$

assuming a linear temperature lapse rate of $1K$ per 100 m of altitude which is a usual value for the low earth atmosphere [16] and fits well with the temperatures measured at the different altitudes of the kite in Table 6.1.
The reference temperature $T_{ref} = 284,4K$ at an altitude of $alt_{ref} = 330m$ corresponds to the value obtained during a long parking time at this constant altitude. Measured air temperature $T_{calibrated}$ is used to calculate alt_T. The kite altitude alt_T computed this way is plotted in Fig. 6.3. It is apparent from this plot that the altitude directly calculated from the measured temperature $T_{calibrated}$ is delayed with respect to the actual altitude for about one minute. Consequently the measured air temperature is not the one that describes the flow situation around the kite best.
To obtain the correct air temperature T at any given flight situation we assume that air temperature during the one hour test flight is only a function of the altitude as in Eq. 6.2. With altitude calculated from barometric pressure according to Eq. 6.1 and the relation of air temperature and altitude as in Eq. 6.2 air temperature T will be calculated from the barometric pressure.
Table 6.1 shows the air temperature T that is calculated with Eqns. (6.1, 6.2) and measured air temperature $T_{calibrated}$ after flight sequences of more than one minute at a roughly constant altitude to account for the temporal delay of the measurement. The comments in Table 6.1 describe the flight situation in which $T_{calibrated}$ was obtained.
Both values show a very good accordance for all different altitudes except for the measurement before launch. As cause we identify the sun radiation heating the

kite altitude	T calculated from altitude	$T_{calibrated}$	comments
-8 m	287,8 K	291,3 K	before launch
-12 m	287,8 K	287,8 K	after landing
170 m	286,0 K	285,3 K	at end of traction phase
330 m	284,4 K	284,4 K	during longterm parking
380 m	283,9 K	283,8 K	after short time parking
430 m	283,4 K	282,9 K	after short time parking

Table 6.1: Difference between calculated air temperature T and measured air temperature $T_{calibrated}$

sensor which is mounted on a black plate and protected by a plastic cover from free air convection. After landing when the sensor was in the shadow below the kite, the measured ground temperature is $3,5K$ lower and corresponds perfectly to the calculated air temperature of $T = 287,8K$ and also to the reported local air temperature of $13°C$ on that day.
From Table 6.1 it is obvious that the suggested calculation method for air temperature T gives good results for all flight altitudes. It does not suffer from a phase shift of 1 minute such as the measured temperature $T_{calibrated}$. This phase shift is especially harmful as it is of the same order of magnitude than the pumping cycle period.
As a consequence the calculated air temperature T is deemed more accurate than $T_{calibrated}$ especially during power production when the kite altitude changes quickly and will therefore be used to calculate air density. Although the temperature sensor is not used directly it is important to have its data to know atmospheric properties at the altitude of the kite's flight and develop the calculation method for real air temperature T.
We will thus apply

$$\rho = \frac{p_{measured} - 370Pa}{R(284,4K - \frac{1K}{100m} \times (alt_p - 330m)} \tag{6.3}$$

using Eqns. (5.4, 6.1, 6.2) for all calculations of air density ρ.
The suggested calibration law for the differential pressure Δp from Sect. 5.5.1 is

$$\Delta p = \frac{\Delta p_{pitot}}{0.971} + \Delta p_{offset}. \tag{5.3}$$

The offset value measured inside a caravan next to the ground station three hours before the test flight was $\Delta p_{offset,c} = -40Pa$.
This value was intended to be used for the data obtained during the test flight. Fig. 6.4 shows the sensed differential pressure Δp_{pitot} and calculated airspeed $v_{a,40}$ using the offset value of $\Delta p_{offset,c} = -40Pa$ and v_a using an offset value of $\Delta p_{offset} = +30Pa$.
Looking at the sensed differential pressure Δp_{pitot} for the time before launch $t \leq 0s$ one sees mainly negative values in the range of $-30Pa \leq \Delta p_{pitot} \leq -10Pa$. Using the original value of $\Delta p_{offset,c} = -40Pa$ would result in having negative values for the differential pressure which is not senseful from a physical point of view (see Eq. 5.2). The pressure difference Δp between total pressure p_t and static pressure p_s is by its nature positive and zero for calm air. This is why the value of $\Delta p_{offset} = +30Pa$ is chosen which results in having positive values for Δp for most of the flight duration. Two exceptions 140 and 30 seconds before launch in Fig. 6.4 coincide with strong vibrations of the measurement assembly as the video footage of the test shows which could explain those values.
For the time before launch we expect measured flow velocities v_a equal to the

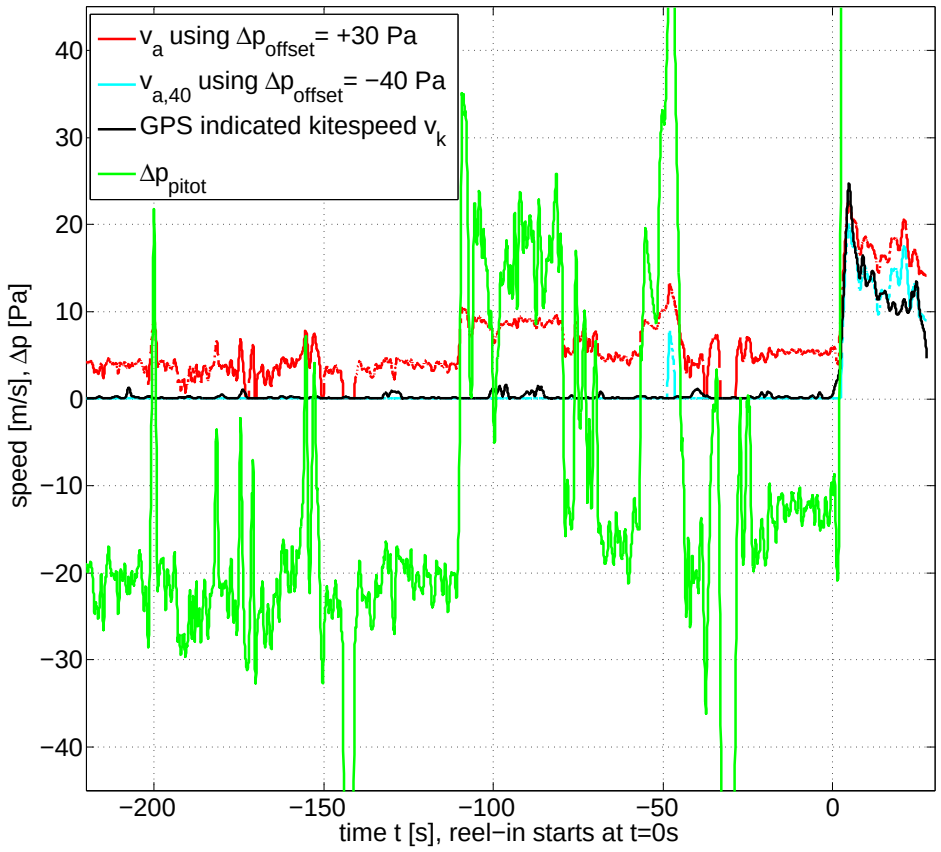

Figure 6.4: Calculated apparent flow velocity v_a using different calibration rules during launch sequence

ground wind speed thus around 5 meters per second. Using the value of $\Delta p_{offset} = +30Pa$ one obtains values for the apparent flow velocities of $4\frac{m}{s} \leq v_a \leq 10\frac{m}{s}$ for the time before launch.
However, different values of $\Delta p_{offset} \in [20Pa, 40Pa]$ could also be justified. The lack of appropriate calibration right before the test flight thus inflicts a measurement uncertainty of $\pm 10Pa$. Especially for values of v_a below $10\frac{m}{s}$ this results in a big uncertainty according to Sect. 5.5. It is strongly recommended to do calibration of the airspeed sensor directly before the test flight and not turn the system off between calibration and flight for any future test.
In order to judge the credibility of the obtained apparent flow velocity Fig. 6.5 illustrates the evolution of v_a together with the kite velocity v_k during flight of pumping cycles. v_k can be calculated as the temporal derivative of the kite

position vector K of Eq. 6.7 according to

$$v_k = |\frac{dK}{dt}|. \tag{6.4}$$

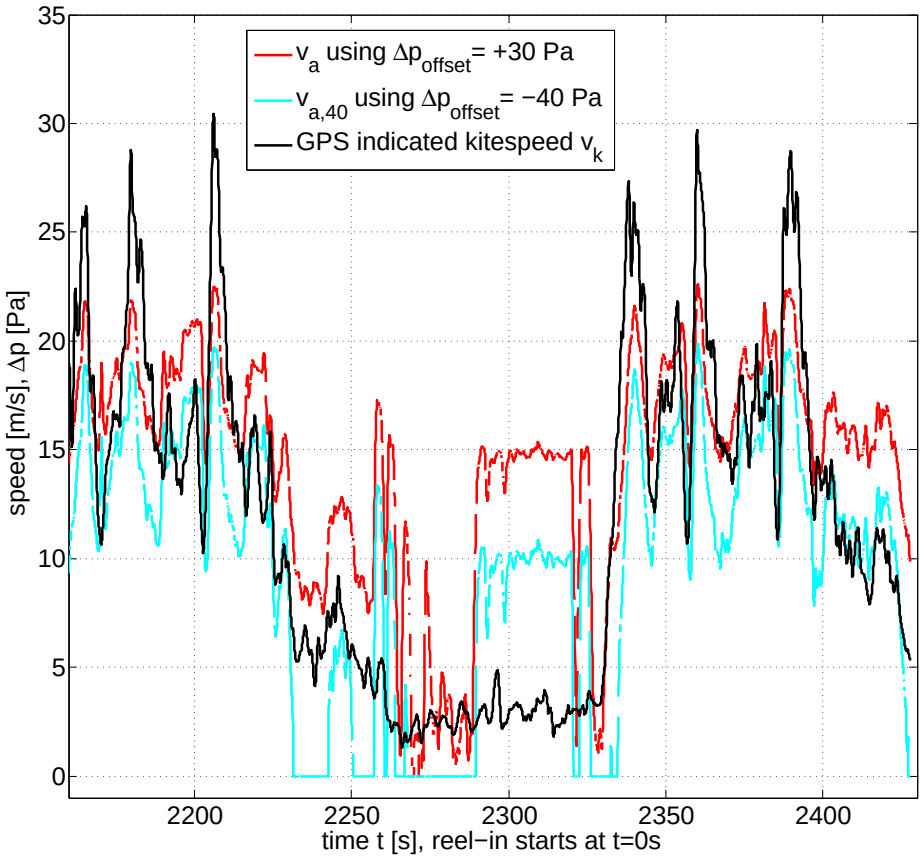

Figure 6.5: Calculated apparent flow velocity v_a for different calibration rules while flying pumping cycles

As explained in Sect. 2.3 kite speed v_k should be sometimes higher and sometimes lower than v_a during traction phase. Looking at v_a this is true for both traction periods in the intervals $t \in [2160s, 2230s]$ and $t \in [2335s, 2400s]$.
$v_{a,40}$ in contrast shows apparent flow speeds that are below the kite's speed throughout both periods which is not in line with the derived model of kite flight. Fig. 6.5 is not a proof that all v_a values are valid but a strong support to the assumption that they can be trusted during traction phase. For the reel-in period there is an interval at $t \in [2265s, 2285s]$ of very low measured air speeds v_a. Similar values are found for other reel-in phases and they are assumed erroneous

as the wind speed alone during reel-in should account for an apparent flow velocity of $10 - 15\frac{m}{s}$.
Possible cause for those repeated error could be vibrations of the system due to the low tether tension during reel-in compared to the traction phase. The video footage of the flight test shows generally more unstable tumbling behavior during parking and reel-in than during traction phase where the measurement assembly seems well stabilized. To conclude the validation section we can state that we have reason to assume good accuracy and valid data during traction phase whereas the value for v_a has to be regarded carefully if not be rejected for reel-in and parking phases as well as any period with indicated airspeed below $v_a = 10\frac{m}{s}$.

6.2 Calculation of the aerodynamic coefficient

The aerodynamic coefficient c_R which is a key parameter for the performance assessment of the kite system can be calculated according to

$$c_R = \frac{2F_a}{\rho v_a^2 S} \tag{2.2}$$

where ρ and v_a are captured by the measurement system that is subject of this thesis. F_a can be calculated from the tether force at the ground station F_{tg} and gravitational effects of the airborne system according to [22].

$$F_a = \sqrt{(\sqrt{F_{tg}^2 - \frac{sin^2\theta m_t^2 g^2}{4}} + cos\theta(m_t + m)g)^2 + (sin\theta(\frac{1}{2}m_t + m)g)^2} \tag{6.5}$$

Tether force at the ground F_{tg} is captured by the ground station, the mass of the kite-KCU-system m is known and tether mass m_t can be calculated as a function of tether length L after

$$m_t = \rho_t \pi r_t^2 L. \tag{6.6}$$

For the V3 kite that weights 11,0 kg plus sensors and antennas on the kite of 2,4 kg and the control pod of 8,4 kg the combined mass is 21,8 kg. Considering 1,0 kg for the flow vector measurement assembly the total mass of the flying wing is $m = 22,8kg$. In order to facilitate the calculation and because of its small role the gravitational effect of the tether is assumed constant. The weight of the tether mass is calculated by using the average tether length over the time where pumping cycles have been flown. In the interval between $t = 1480s$ to $t = 3230s$ the tether length varied between a minimum of 220 meters and a maximum of 484 meters with the mean value over time being $L = 345m$.
Using this tether length we calculate a tether mass of $m_t = 3,1kg$ from Eq. 6.6 with the tether radius being $r_t = 0,002m$ and the density of the tether being

$\rho_t = 724\frac{kg}{m^3}$ (see [22]). The polar angle θ in 6.5 can be calculated from the vector K that points from the ground station to the kite. As the position of the ground station is known and the IMU on the kite provides the current kite position this vector in NED coordinate system can be obtained via

$$K = \overrightarrow{GS, kite} = \begin{bmatrix} k_{north} \\ k_{east} \\ k_{down} \end{bmatrix} = \begin{bmatrix} (lat_{kite} - lat_{GS}) \times \frac{40000000m}{360°} \\ -(long_{kite} - long_{GS}) \times \frac{cos(lat_{GS})40000000m}{360°} \\ -(alt_{kite} - alt_{GS}) \end{bmatrix} \tag{6.7}$$

with lat_{kite}, $long_{kite}$ and alt_{kite} being the kite's GPS position. We thereby assume a ball-shaped earth with a circumference of 40 000 km. The kite's polar angle θ calculates from the Cartesian coordinates of Eq. 6.7 after

$$\theta = atan(\frac{\sqrt{k_{north}^2 + k_{east}^2}}{-k_{down}}). \tag{6.8}$$

Using Eqns. (2.2, 6.5, 6.7 and 6.8) the resulting aerodynamic coefficient of the kite system c_R can be calculated.
It is plotted for the first 8 out of 10 pumping cycles for the interval $t \in [1480s, 2980s]$ thereby ignoring all data points where $v_a \leq 13\frac{m}{s}$ as those speeds are considered faulty and unrealistic (see Sect. 6.1). The plot also shows the power ratio PR of the kite and the polar angle θ.
A polar angle of $\theta = 60°$ is equal to an elevation of $\beta = 30°$ during traction phase, low polar angles of around $\theta = 10 - 20°$ indicate the parking and reel-in phase and correspond to high elevation angles. The power ratio is always at $PR = 0,5$ for the traction phase and usually decreases to $PR = 0,2 - 0,3$ during reel-in. Thereby a high power ratio means the bridles that connect with the trailing edge are shortened, at a lower value they are given slack, the kite is being 'depowered'. The limits $PR = 0$ and $PR = 1$ are the theoretical limits of the control motor and do not necessarily result in a kite that can sustain controllable flight. This is why only values in the range $PR \in [0,2; 0,5]$ are used.
The first two pumping cycles were flown without depowering the kite for reel-in. This results in a longer reel-in time of around two minutes compared to one or one and a half minutes for the usual depowered reel-in. A good depower capability obviously increases the system efficiency as there is a higher fraction of time with positive power production. Further we see lower polar angles during parking for the non-depowered kite. This is in line with the common quasi-steady model of a kite [22]. Depowering decreases the lift-to-drag value of the kite $\frac{L}{D}$ and results in a higher polar angle at the parking position. During reel-in without depowering,

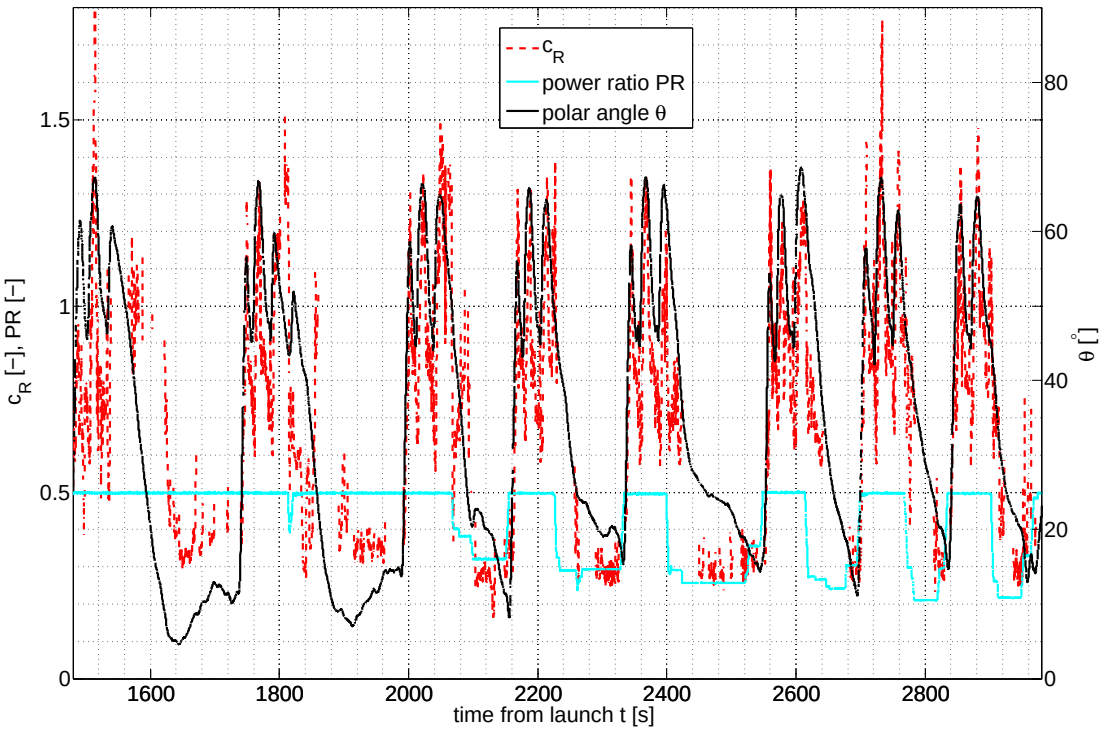

Figure 6.6: Variation of the aerodynamic coefficient c_R over 8 pumping cycles

polar angles of $\theta = 5 - 15°$ occur, for depowered reel-in the polar angles captured are considerably higher at $\theta = 10 - 25°$ (see Fig. 6.6).
What is obvious from this plot and supported by [22] is that c_R values are very low during reel-in and much higher during traction phase. For reel-in values of $c_R = 0,25 - 0,4$ are found, whereas during traction phase the coefficient oscillates around a mean value of $c_R = 0,7 - 1,0$. Usually this variation in c_R is explained with the depowering of the kite. However, for power cycles that were flown without any depowering thus a constant power ratio of $PR = 0,5$ for traction and reel-in the c_R value still changes from 0,9 during traction to 0,35 during reel-in. So obviously the depowering cannot explain the huge difference of c_R for the different phases.
Fig. 6.7 shows the aerodynamic coefficient c_R for different kites under varying conditions. For the Hydra V5 kite there is data available for two different wind speeds. It is apparent from Fig. 6.7 that wind speed has a strong effect on the resultant aerodynamic coefficient c_R.
Looking at the values for the Hydra kite for a constant power ratio of $PR_{Hydra} = 0,6$ we see the resultant aerodynamic coefficient varying from $c_{R,Hydra,22kt} = 0,5$ for a low wind speed of $v_a = 22kt = 11,3\frac{m}{s}$ to $c_{R,Hydra,29kt} = 0,7$ for a higher wind speed of $v_a = 29kt = 15\frac{m}{s}$. These values have been obtained in a tow test

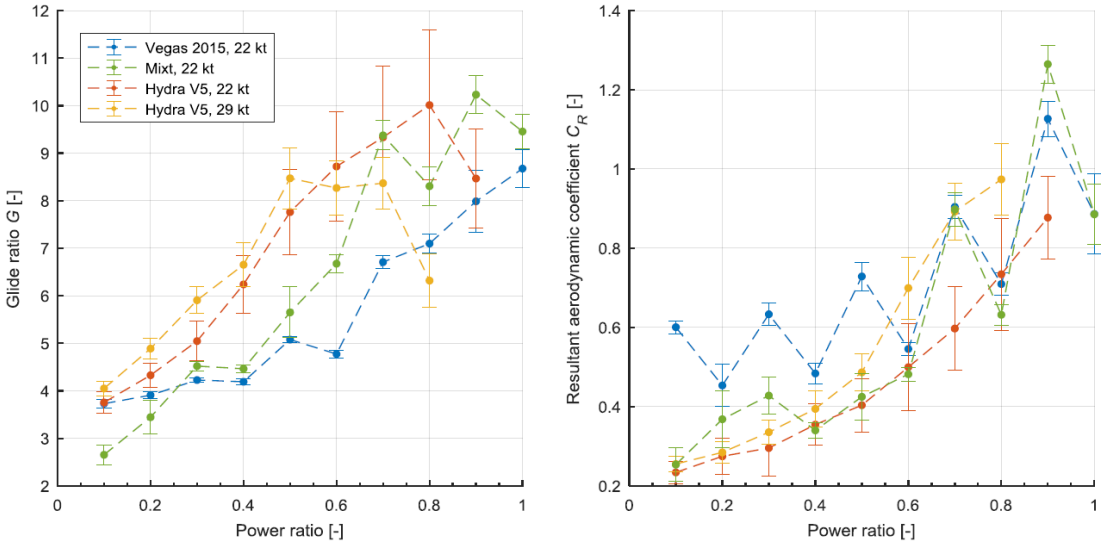

Figure 6.7: Variation of the aerodynamic coefficient c_R with depower ratio and wind speed for different kites [17]

where the apparent flow velocity v_a of the kite is equal to the wind speed just as in Fig. 2.3.
According to Eq. 2.2 the aerodynamic force is growing with the square of v_a, thereby deforming the kite and changing c_R. The precise physical changes in kite geometry, presumably a change in camber due to high loading are not regarded closely in this thesis as the FSI-problem a kite poses is too big to be covered here. As differences in airspeed and loading during one power cycle of our test flight are higher than the ones in Fig. 6.7 for the Hydra V5 kite the mentioned effect that higher loading increases the wing's c_R can account for the important change in c_R from 0,9 to 0,35 even without changing the power setting of the kite.
Using the depower capability of the kite the aerodynamic coefficient can be further decreased down to $c_R = 0,25$ as seen in the pumping cycles 3 till 8 in Fig. 6.6. As a first approach it is assumed that F_a and PR influence the aerodynamic properties of the kite and thus c_R. Fig. 6.8 shows the c_R value in the same period as Fig. 6.6 with the additional value of c_R* which is calculated according to

$$c_R* = 0,2 + \frac{F_a}{F_a, max} \times \sqrt{\frac{PR - PR_{min}}{PR_{max} - PR_{min}}} \tag{6.9}$$

with the maximum aerodynamic force $F_{a,max} = 3,75kN$ and the minimal and maximal power ratio of $PR_{min} = 0,2$ and $PR_{max} = 0,5$. The constant value of 0,2 accounts for the minimal aerodynamic coefficient the wing always has due to its drag and minimum lift value c_L which is required to keep the kite's shape and tether drag.

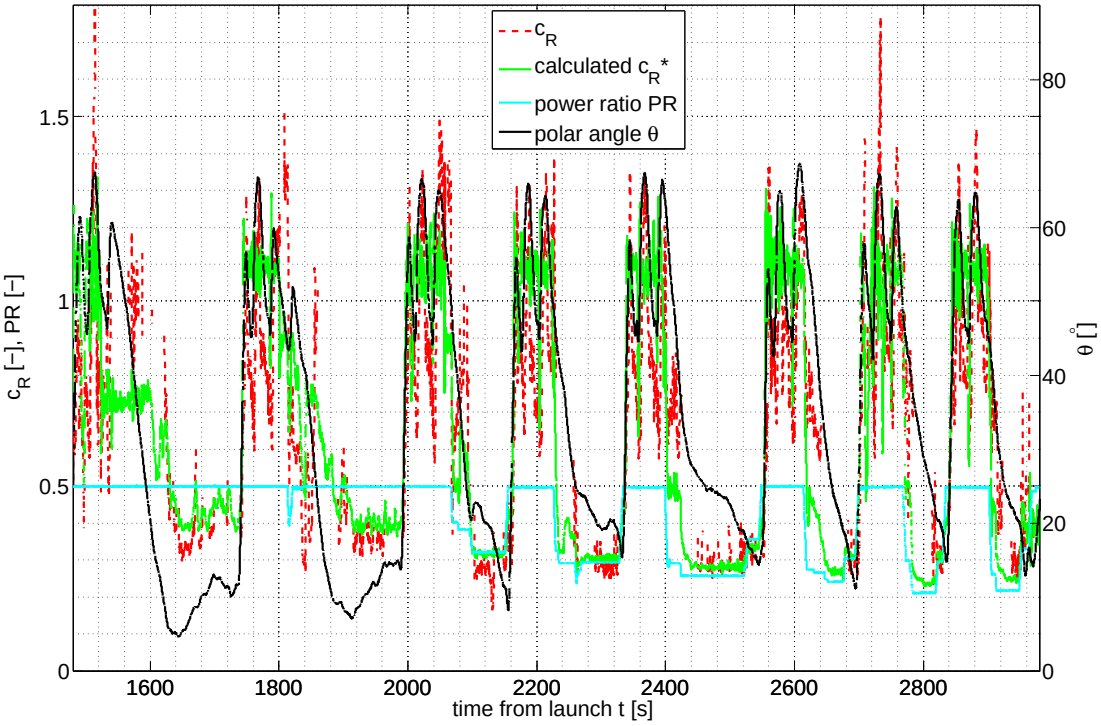

Figure 6.8: Prediction of the aerodynamic coefficient c_R over 8 pumping cycles using power ratio and wing loading

The proposed correlation can very well explain the differences in c_R during traction and retraction phase, thereby using only values that are by default captured from the pumping kite power system as they are essential to the control of the kite. However taking a closer look into the traction phases in Fig. 6.8 one can not explain all variations that occur during traction phase. As both tether force F_{tg} and power ratio are held constant most of the time during traction phase the model can not predict fluctuations in c_R during traction phase.
The aerodynamic coefficient c_R shows a systematic scheme that seems to be correlated with the polar angle θ although there is no model so far that would link both values. In Sect. 2.3 the influence of gravity on the inflow vector is mentioned. During upward flight we should experience higher values for the inflow angle α, during downward flight it should be lower. The influence of the angle of inflow on c_R will thus be given a closer look in Sect. 6.3.

6.3 Inflow angles

The raw signal for the inflow angle measurement consists of supply voltage U_{ref} and the two signal voltages for the sideslip angle U_1 and for the vertical inflow

angle U_2. Fig. 6.9 shows those three voltages during the entire test flight. The supply voltage stays between 4,6 and 4,7 Volts with some drops to a lower voltage. Except for one occasion at around $t = 2550s$ supply voltage never goes below 4,5 Volts which is the lower limit for the sensor to work properly according to its data sheet (Appendix A).

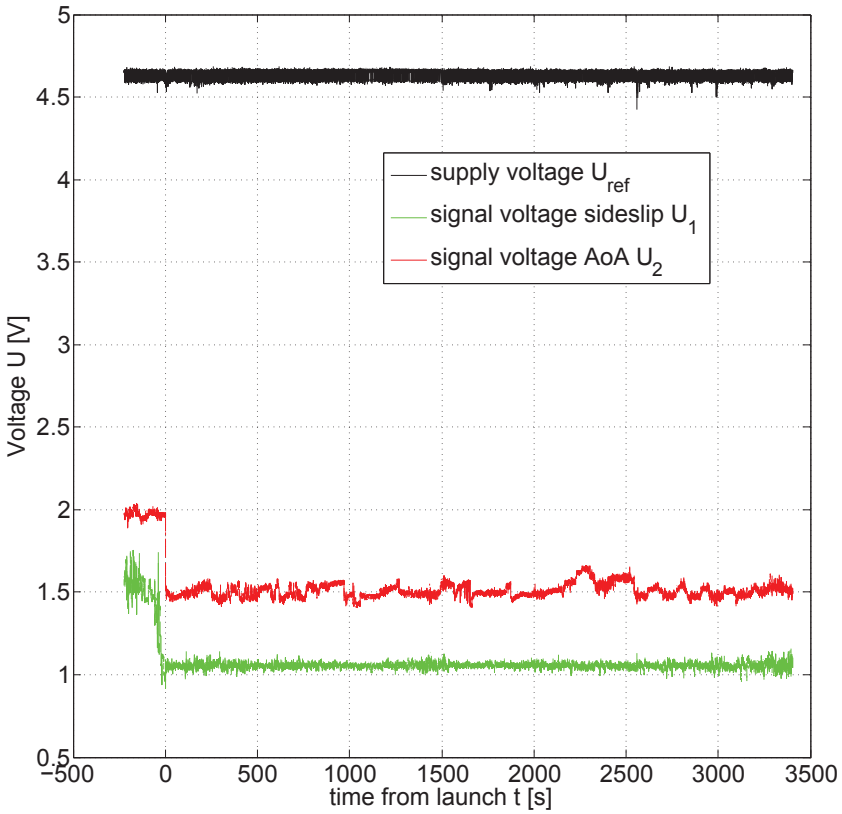

Figure 6.9: Signal and supply voltages for the angular measurement during one hour of testflight

Both signal voltages behave as expected. They vary less than $\pm 0,1V$ around their mean value which corresponds to a variation in inflow angles of $\pm 15°$ according to Sect. 5.5.2 during the flight. Before launch we have a different signal because the kite is not flying and the wind vanes are in a more or less arbitrary position that changes due to local ground wind or preflight operations.
Looking closer at the oscillations of the analog signal in Fig. 6.10 we see that for every drop in supply voltage the signal voltages drop as well. This is due to the ratiometric character of signal voltage to supply voltage and should in theory not affect the calculated angle. However for many voltage oscillations as at $t = 831,5s$ and $t = 832,5s$ we see a sharp peak of the calculated inflow angle α. This might be due to a delay of the signal voltage with respect to the supply voltage that

would result in a different ratio of $\frac{U_{signal}}{U_{ref}}$ for a short period of time.
To avoid these presumably erroneous angular measurements we apply a smoothing function which considers values in an interval of half a second. Choosing a bigger interval for the smoothing function is not suggested as the reel-out speed which effects the inflow angle α oscillates with about one Hertz (see Fig. 6.14).

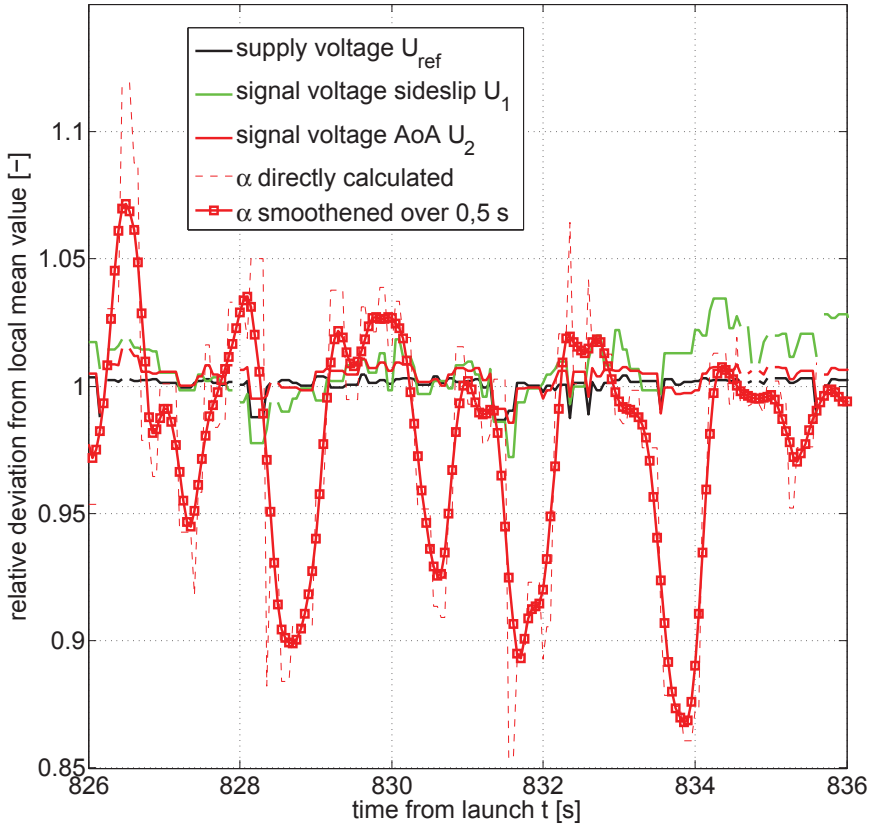

Figure 6.10: Smoothing rule for the measured angles to correct for errors induced by supply voltage oscillation

The angular signal obtained (red solid line with squares in Fig. 6.10) does not show sharp peaks that coincide with sudden changes in supply voltage and has the additional advantage of being continuous other than the signal calculated directly from the measured voltages (red dashed). We will therefore use this smoothing rule for all angles plotted in this section.

Fig. 6.11 shows the sideslip angle β and inflow angle α during the entire test flight. The deviation from the expected symmetrical mean value of $\beta_{mean,ideal} = 0°$ is with a mean angle of sideslip over the whole flight period of $\beta_{mean} = -3,8°$ considerably bigger than the expected measurement uncertainty of $1,9°$. We therefor assume some systematic asymmetric inflow.

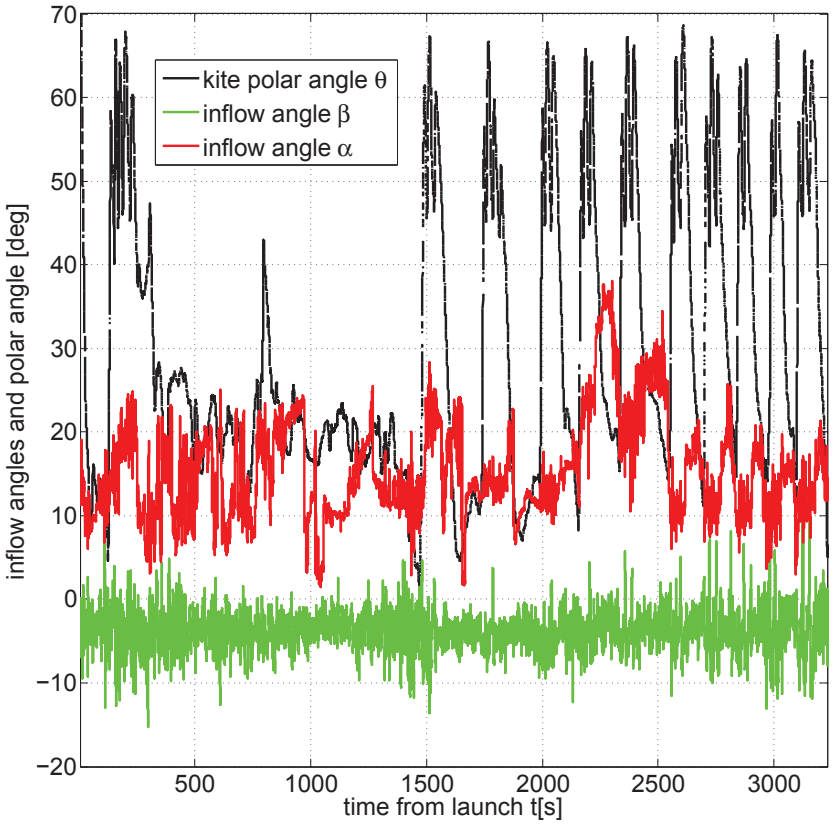

Figure 6.11: Variation of the inflow angles β and α during flight

Looking at the steering input in Fig. 6.12 we see that also the relative steering value is not centered around its neutral position but has a systematic offset. Also is the flight path not symmetric, usually one side of the figure of eight flown has a much smaller curvature radius then the other side, sometimes even oval figures are flown. Later we found that the bridle system of the V3-kite flown was not symmetric which is identified as the cause for this abnormal sideslip angle and steering behavior. In general we see that sideslip angles are small, they lie mainly in an interval of $\beta \in [-14°; 6°]$.
The vertical inflow angle shows more variation. In the first 2000 seconds of flight, it varies for $\pm 10°$ around a mean of $\alpha_{mean,0-2000} = 14,1°$. For the last eight pumping cycles where the depower capability of the kite is used (see Sect. 6.2) it varies in a very systematic way. Inflow angle α is low during traction phase and high during retraction. The fourth and fifth pumping cycle show outstandingly high values of up to $\alpha = 37°$. The reason for that is unknown, but we will focus on the angles observed in the other pumping cycles.
The mean value for the sixth till 10th pumping cycle is $\alpha_{mean,cycle6-10} = 13,5°$. During traction phase the vertical inflow angle is usually around $\alpha_{mean,traction} = 11°$, for reel-in the mean value is $\alpha_{mean,reelin} = 17°$. This systematic difference is not

observed for the first two pumping cycles where the kite's power ratio PR is constant. This is why we credit the variation from low α during traction phase and high α during reel-in to the depowering of the kite.

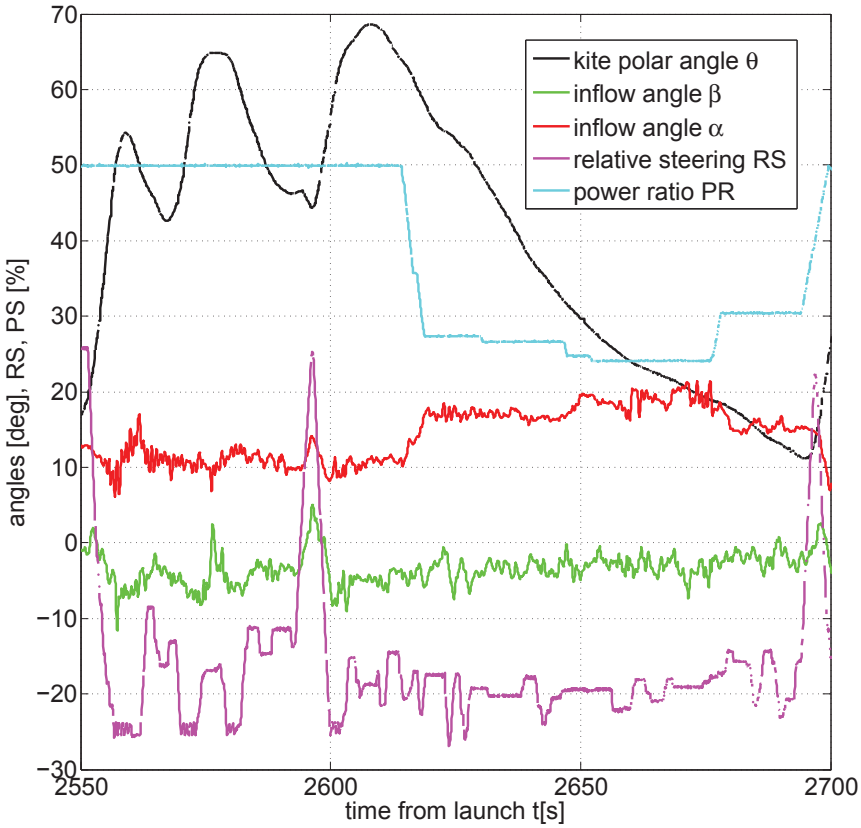

Figure 6.12: Variation of the inflow angles β and α during one pumping cycle

Looking at Fig. 6.12 it is evident that depowering is the main cause for the change in inflow angle as every variation of the kite's power ratio PR has an instantaneous effect on α. Thereby a lower power ratio PR increases the inflow angle α. However the variations during traction phase where the power ratio remains constant at $PR = 0,5$ cannot be explained that way.
Looking at the sideslip angle β during one pumping cycle in Fig. 6.12 we see that the steering is the dominant cause for any change in the sideslip angle β. During reel-in from $t = 2625s$ till $t = 2680s$ where the steering command is only used to maintain a stable orientation into the wind the inflow angle shows only minor oscillation around the long term mean of $\beta_{mean} = -3,8°$.
During traction phase where the kite is actively steered to follow the intended flight path we see strong steering commands such as in the interval $t \in [2550s; 2600s]$. Every steering command is closely followed by a change in sideslip angle in the same direction. The stronger the steering command, the stronger is usually

the change in sideslip angle β, strong deviations can be seen at $t = 2595s$ or $t = 2695s$. With the steering command known we can thus predict the change in β very well. There is no reason to assume other variables systematically affecting the sideslip angle β.

In order to determine what effects the vertical inflow angle during traction phase we take a closer look at this interval. Considering that we assume a dependency of c_R on α and are looking for a prediction of c_R that also covers variations during traction phase we plot c_R, reel-out speed v_{reel} and apparent flow velocity v_a together with the inflow angle α only for the traction phase in Fig. 6.13.

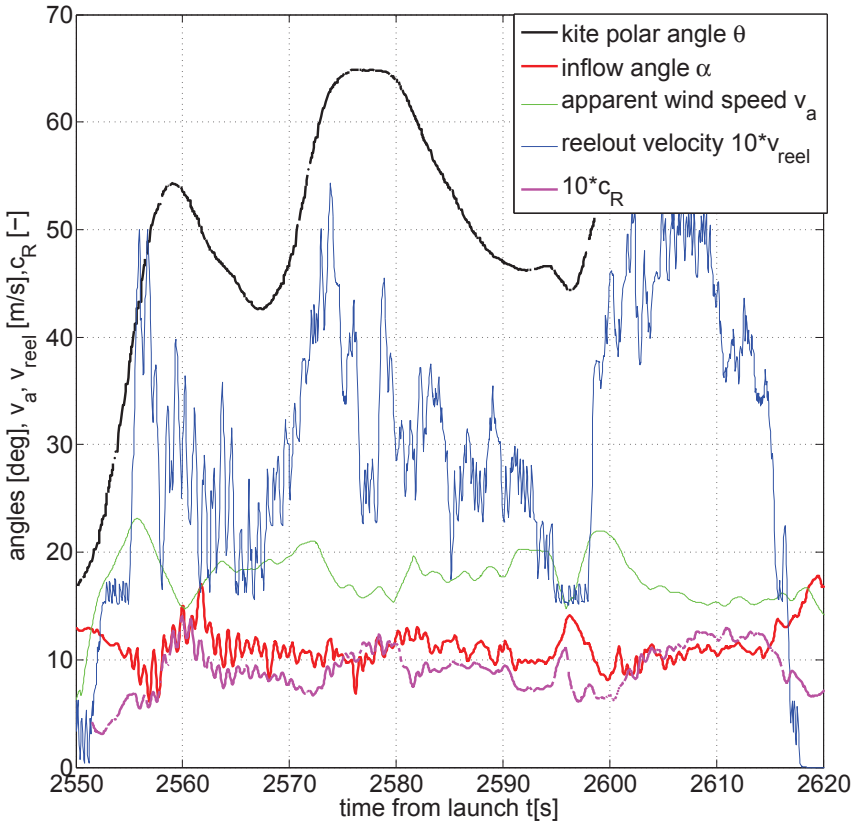

Figure 6.13: Variation of the inflow angle α and c_R during traction phase

We see that inflow angle α and the aerodynamic coefficient c_R correlate very well during traction phase from $t = 2555s$ till $t = 2615s$. In order to account for the variations of c_R during traction phase we will therefore consider the vertical inflow angle α for a better prediction of c_R* as already mentioned in Sect. 6.2.
We see two different kinds of variations for the inflow angle: A fast oscillation with a frequency of about one Hertz and an amplitude of around two degrees as well as some systematic low frequent changes with a higher amplitude of up to 5 degrees. The low frequent variation can be explained by the flight path of the

kite. Whenever we fly downward and have a positive gradient of the polar angle θ, such as at $t = 2556s$, $t = 2572s$ and $t = 2599s$ gravity acts in flight direction. We achieve higher apparent flow speeds and consequently a lower inflow angle as explained in Sect. 2.3. The winch controller which commands reel-out velocity to keep the tether force F_{tg} within its specified limit increases the reel-out velocity at those high flow velocities. The higher reel-out velocity supports the effect of a lower inflow angle during downward flight as reel-out velocity is parallel to the driving wind velocity in crosswind flight (see Fig. 2.3) and will thus decrease the effective wind velocity.
For upward flight such as at $t = 2560s$, $t = 2581s$ and $t = 2596s$ we see the opposite effect. Gravity is opposed to flight direction and decelerates the kite, we obtain lower apparent flow speeds v_a, lower reel-out speeds v_{reel} and measure consequently higher inflow angles α. The increase of α tilts the resultant aerodynamic force vector upwards which balances gravitation as shown in Fig. 2.5. The gravitational effect can thus explain very well the low frequent changes in angle of attack.
The high frequency oscillation occurs only when we reel out faster than $v_{reel,nominal} \approx 1,6\frac{m}{s}$. This is an indication that the tether force is at its intended maximum of about $F_{t,nominal} \approx 3250N$ and thus a well tensioned tether can be assumed. As the reel-out velocity v_{reel} shows oscillations with the same frequency as the inflow angle, we assume that they are correlated. Considering that the inflow angle α is an entirely independent variable measured on the kite there must be a physical cause if they show similarities.

Fig. 6.14 therefore shows the vertical inflow angle α and the reel-out velocity v_{reel} for a short interval with high temporal resolution during traction period. Both signals obviously oscillate with a frequency of about 1,2 Hertz. Every peak in reel-out velocity coincides with a valley for the vertical inflow angle.
To explain this high frequency oscillation we assume the kite's inertia in forward flight being high compared to the high frequency of 1,2 Hertz. This can be supported by looking at the apparent flow speed v_a which does not show any sudden changes and varies on a timescale of several seconds even during sudden changes of v_{reel}. When we assume ideal crosswind flight and flight speed magnitude constant, any increase in reel-out velocity will decrease the effective wind component vertical to the kite's flight direction which decreases the angle of inflow. As the kite is tethered to the ground station it has to follow the reeling velocity immediately if the tether is assumed highly tensioned. The flutter effect of a changing inflow angle α can therefore be explained with the dynamic behavior of the winch controller, commanding reel-out velocity v_{reel}.

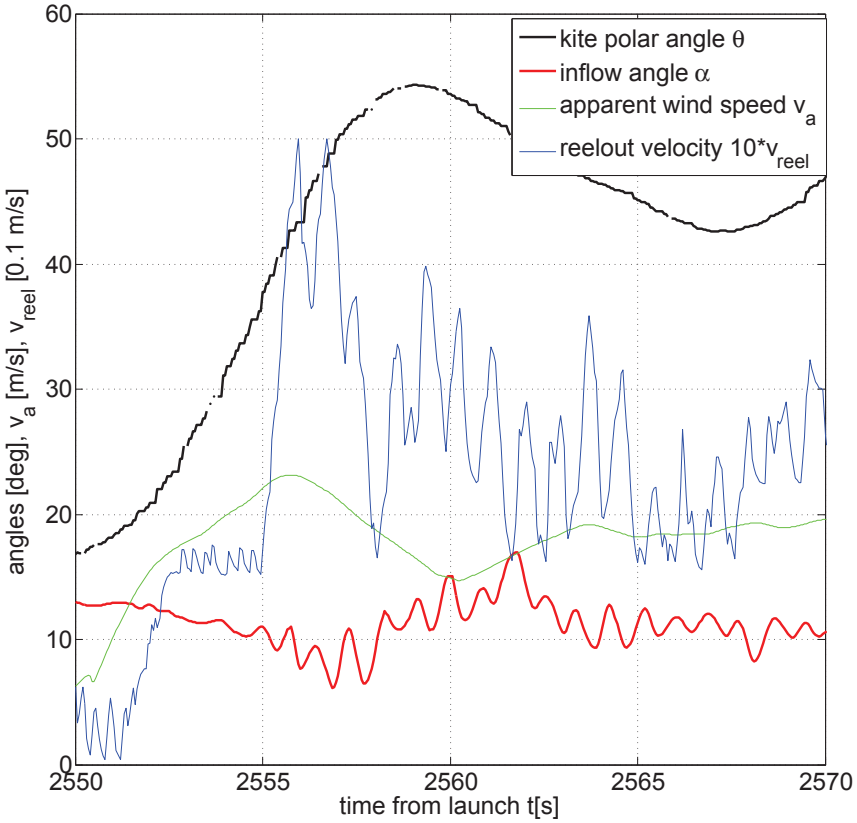

Figure 6.14: High frequency oscillations of the inflow angle α and v_{reel} during traction phase show the same frequency and a good correlation

6.4 Prediction of c_R

Coming back to a prediction for the aerodynamic coefficient c_R, I suggest following rule

$$c_R* = 0,2 + \frac{F_a}{F_a, max} \times \sqrt[4]{\frac{PR - PR_{min}}{PR_{max} - PR_{min}}} \times \frac{\alpha}{\alpha_{max}} \tag{6.10}$$

derived from Eq. 6.9 proposed in Sect. 6.2 and additionally taking into account the vertical inflow angle α. The value for the maximal inflow angle is set to $\alpha_{max} = 15°$ which is the maximum vertical inflow angle that usually occurs during traction phase (see Fig. 6.13, 6.14). The so predicted resultant aerodynamic coefficient c_R* is plotted in Fig. 6.15 for the last five pumping cycles of the flight test together with the actual c_R value obtained from Eq. (2.2).
We see a good correlation of the two values. It matches better than the predicted c_R* values from Fig. 6.8 where the inflow angle is not considered. The differences between traction and retraction are captured very precisely, looking into the single traction phases in Fig. 6.16 there are still some intervals where the suggested rule cannot match the real aerodynamic coefficient c_R.

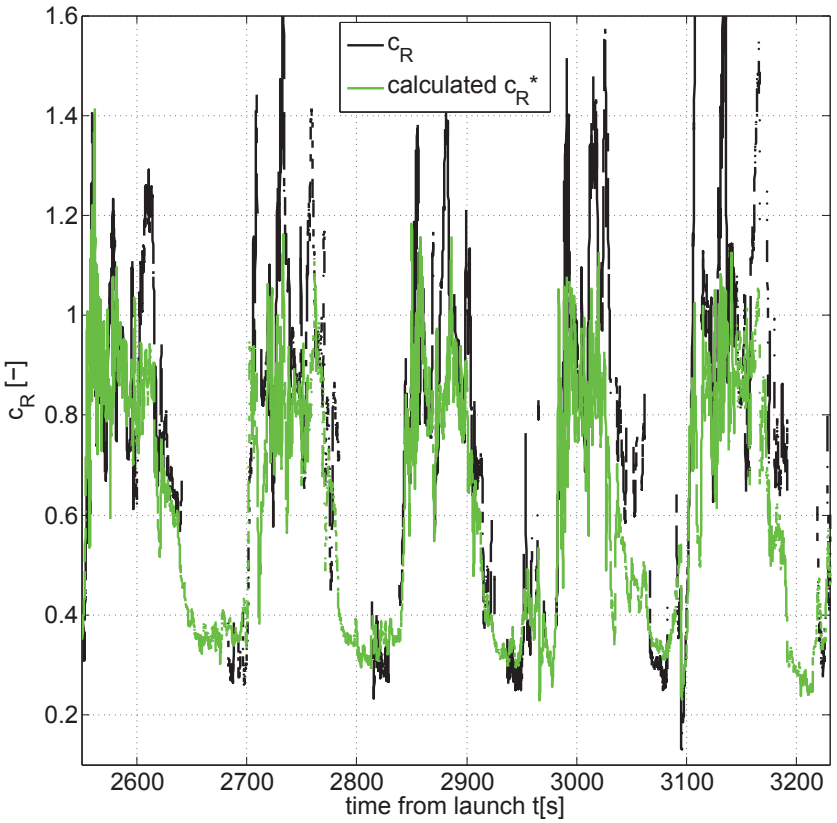

Figure 6.15: Predicted $c_{R}*$ value calculated from aerodynamic Force F_a, power ratio and inflow angle α compared with real c_R

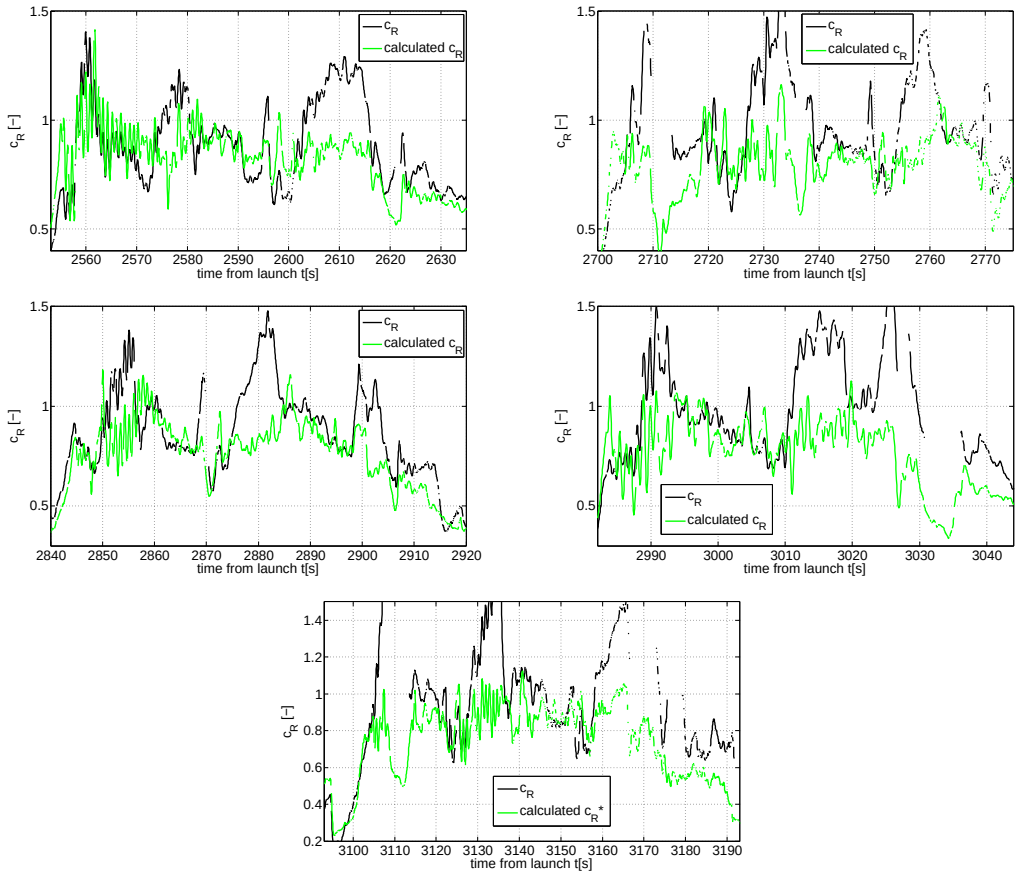

Figure 6.16: Predicted c_R* values during traction phase calculated from aerodynamic Force F_a, power ratio and inflow angle α compared with real c_R

Chapter 7

Conclusion and outlook

The measurement setup developed in this thesis supplies accurate data about the apparent flow vector of the kite. All variations of the flow vector V_a can be physically explained by steering commands, gravitational effects as discussed in Sect. 2.3 plus the reeling velocity v_{reel} commanded by the force dominated winch controller.

7.1 Conclusion

The first two research questions are addressed by the measurement setup in Fig. 6.2 and the evaluation of the acquired data during a one hour test flight in Chapter 6. An air data boom mounted in the bridles below the kite can measure apparent flow magnitude and inflow angles with good accuracy and high temporal resolution.
As response to the third research question we identified four variables having a major effect on the apparent flow vector V_a. The heading angle of the kite which changes the orientation of relevant gravitational force acting on the kite with respect to its flight direction, the steering and depower commands as well as to a lesser extent the reeling velocity v_{reel}.
The answer to the fourth research question is mainly the development of a relation for the resultant aerodynamic coefficient of the airborne system c_R. With the help of the data acquired by the experimental setup a dependency of this coefficient on wing loading, power ratio and inflow angle was found and quantified in the following equation:

$$c_R* = 0,2 + \frac{F_a}{F_a, max} \times \sqrt[4]{\frac{PR - PR_{min}}{PR_{max} - PR_{min}}} \times \frac{\alpha}{\alpha_{max}} \tag{6.10}$$

In order to optimize the flight path for power production this dependency of c_R on aerodynamic loading should be accounted for. The reliable measurement of v_a over a long period allowed for the first time a calculation of the aerodynamic coefficient c_R supported by experimental data. The prediction for c_R* of Eq. (6.10) is closer to the real values than a constant value of c_R for each traction and retraction phase or a sole dependency on angle of attack and power ratio

as suggested in [7]. A further experimental finding that can help to improve the future performance of the pumping kite system is the high frequency oscillation of the inflow angle α induced by the oscillation of the reeling velocity v_{reel}. It was first observed in the scope of this thesis and implies that the control law for the winch control should be optimized to avoid this high frequency oscillations in tether force, reeling velocity and inflow angle.

7.2 Outlook and recommendations

The correlation found for the aerodynamic coefficient c_R* is only valid for one kite model. Repeating the experiment with different kites in order to obtain the referring parameters of Eq. (6.10) for those kites and to have a basis for the extrapolation of the behavior of a projected future design seems promising.

The dependency of c_R* on the inflow angle should be replaced by a relation with variables that are always captured during flight such as heading angle and reeling velocity in contrast to the inflow angle. The results in Sect. 6.3 imply that this is possible.

Furthermore, it seems crucial to evaluate the coupling of the ground station's winch with the inflow angle of the kite. The physical properties of the winch such as a slow response to a new command and the current control law result in strong oscillations of the inflow angle and tether force. These oscillations have a negative influence on power output and lifespan of the system and should therefore be eliminated.

Considering the variables affecting the apparent flow vector identified in Chapter 6 we can explain all major changes of V_a. Therefore, we assume that wind gusts that are sometimes blamed to perturb the apparent flow of the kite are balanced by the force controlled winch. In a force controlled traction kite system wind turbulence consequently has a strong effect on the power production which is proportional to reel-out speed (Eq. (2.1)) but not on the apparent flow. This effect could be investigated further and might be a starting point to derive an average wind profile for the altitudes the kite is flying at.

Extrapolating wind data measured on the ground to a high altitude inflicts errors (see Sect. 2.2). Using the current data set of the kite system and the measurement of the apparent flow vector it seems possible to relate GPS-indicated kite position plus tether force and reeling velocity to the actual wind direction at the altitude of the kite. Once such a relation is established the optimal flight path in the wind window can be found using only data from the ground station and the kite's GPS signal which are compulsory for kite control other than an additional wind sensor.

Appendix A

The core elements of the angular rotation measurement unit, magnet and sensor were provided as free samples from:

ams AG
Tobelbader Strasse 30, 8141 Premstaetten, Austria

The full data sheet of the sensor is available at:
http://ams.com/eng/Products/Magnetic-Position-Sensors/Angle-Position-On-Axis/AS5043

The magnet used is a AS5000-MD6H-1 model, its full data sheet is available at:
http://ams.com/eng/Products/Magnetic-Position-Sensors/Magnets

Essential parts of the sensor data sheet that are referred to in the thesis are printed in the following pages.

AS5043

Programmable 360° Magnetic Angle Encoder with Absolute SSI and Analog Outputs

General Description

The AS5043 is a contactless magnetic angle encoder for accurate measurement up to 360°.

It is a system-on-chip, combining integrated Hall elements, analog front end and digital signal processing in a single device.

The AS5043 provides a digital 10-bit as well as a programmable analog output that is directly proportional to the angle of a magnet, rotating over the chip.

The analog output can be configured in many ways, including user programmable angular range, adjustable output voltage range, voltage or current output, etc...

An internal voltage regulator allows operation of the AS5043 from 3.3V or 5.0V supplies.

Ordering Information and *Content Guide* appear at end of datasheet.

Key Benefits & Features

The benefits and features of AS5043, Programmable 360° Magnetic Angle Encoder with Absolute SSI and Analog Outputs are listed below:

Figure 1:
Added Value of Using AS5043

Benefits	Features
• Highest reliability and durability	• Contactless high resolution rotational position encoding over a full turn of 360 degrees
• Simple programming	• Simple user-programmable zero position
• Multiple interfaces	• Serial communication interface (SSI) • Programmable 10-bit analog output
• Ideal for robotic and motor applications	• Input mode for optimizing noise vs. speed
• Failure diagnostics	• Failure detection mode for magnet placement monitoring and loss of power supply
• Easy setup	• Serial read-out of multiple interconnected AS5043 devices using Daisy Chain mode
• Small form factor	• SSOP 16 (5.3mm x 6.2mm)
• Robust environmental tolerance	• Wide temperature range: -40°C to 125°C

Applications

AS5043, Programmable 360° Magnetic Angle Encoder with Absolute SSI and Analog Outputs is ideal for applications with an angular travel range from a few degrees up to a full turn of 360°, such as:

- Industrial applications:
  - Contactless rotary position sensing
  - Robotics
  - Valve controls
- Automotive applications:
  - Throttle position sensors
  - Gas/brake pedal position sensing
  - Headlight position control
- Front panel rotary switches
- Replacement of potentiometers

Figure 2:
Typical Arrangement of AS5043 and Magnet

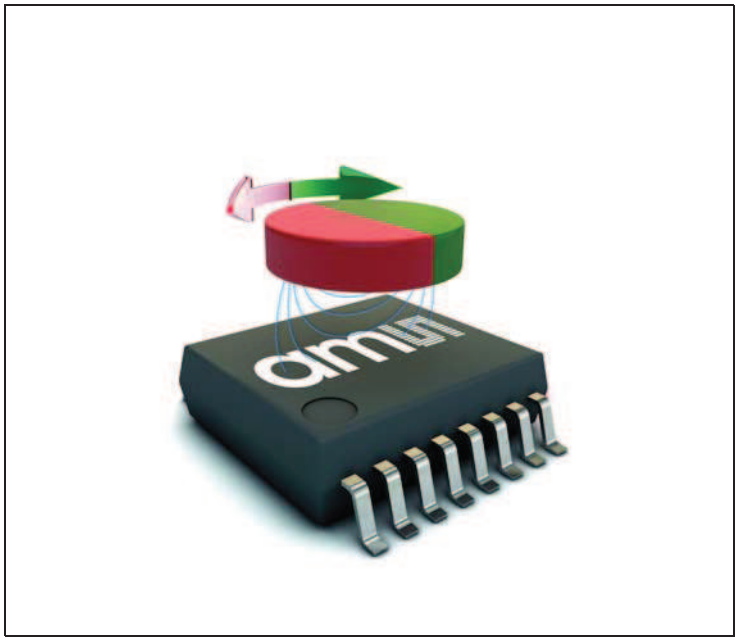

Block Diagram

The functional blocks of this device are shown below:

Figure 3:
AS5043 Block Diagram

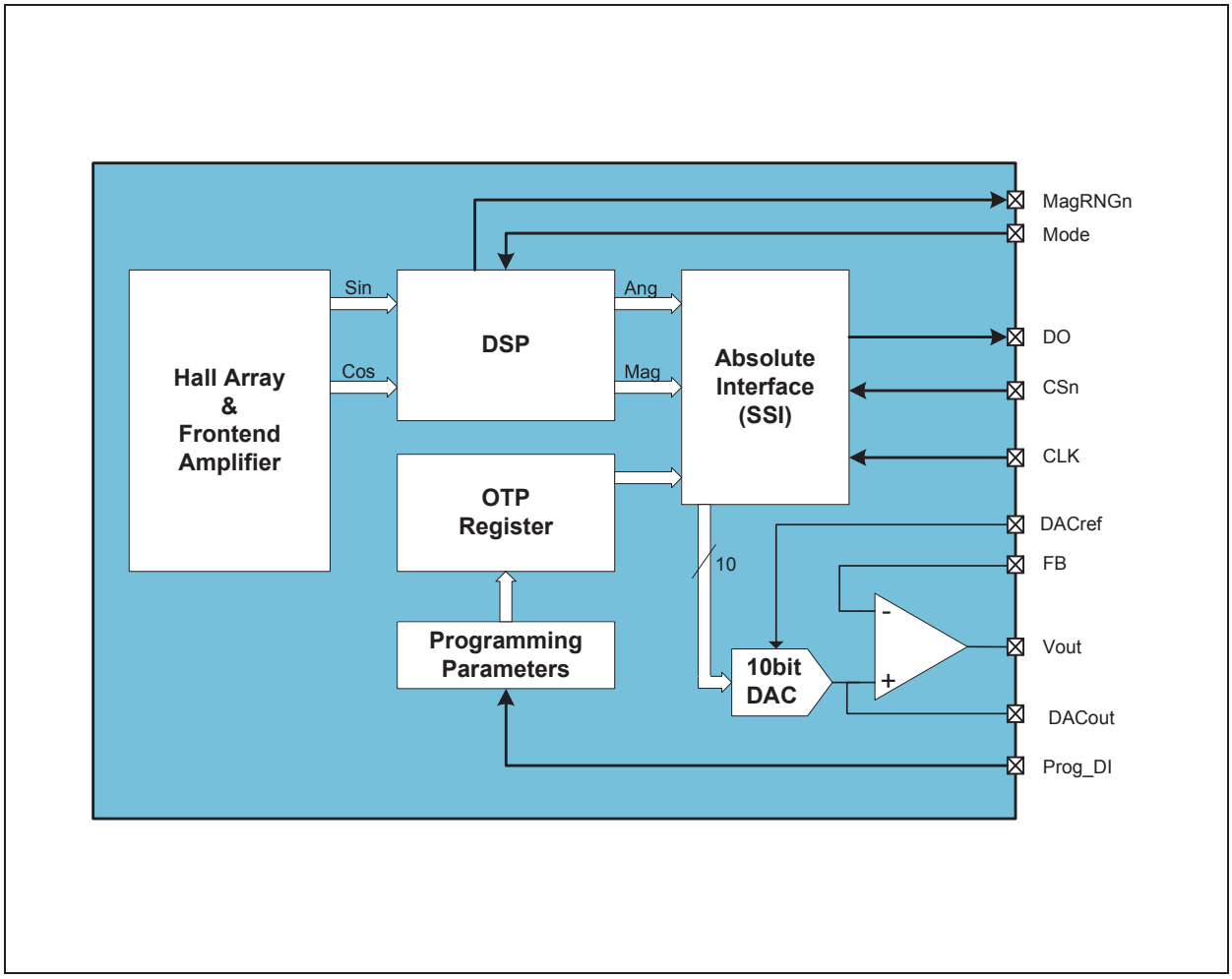

Pin Assignment

Figure 4:
AS5043 Pin Configuration SSOP16

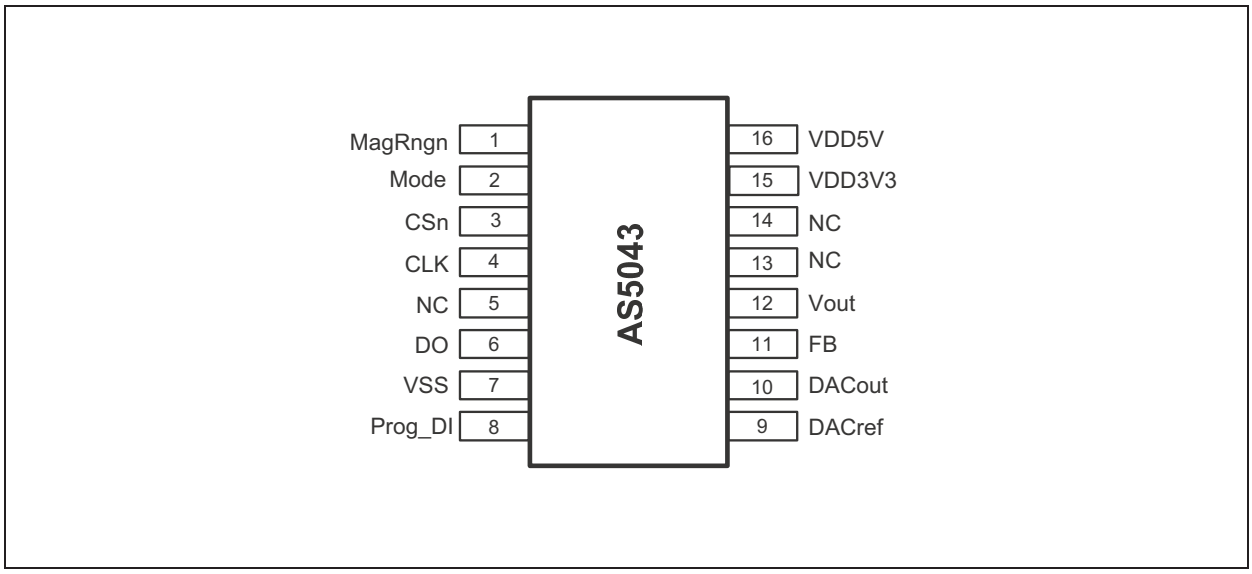

Package = SSOP16 (16 lead Shrink Small Outline Package)

Figure 5:
Pin Description SSOP16

Pin	Symbol	Type	Description
1	MagRngn	DO_OD	Magnet Field **Mag**nitude **R**a**NG**e warning; active low, indicates that the magnetic field strength is outside of the recommended limits.
2	Mode	DI_PD, ST	**Mode** input. Select between low noise (low, connect to VSS) and high speed (high, connect to VDD5V) mode at power up. Internal pull-down resistor.
3	CSn	DI_PU, ST	**C**hip **S**elect, active low; Schmitt-Trigger input, internal pull-up resistor (~50kΩ)
4	CLK	DI,ST	**Cl**oc**k** Input of Synchronous Serial Interface; Schmitt-Trigger input
5	NC	-	Must be left unconnected
6	DO	DO_T	**D**ata **O**utput of Synchronous Serial Interface
7	VSS	S	Negative Supply Voltage (GND)
8	Prog_DI	DI_PD	OTP **Prog**ramming Input and Data Input for Daisy Chain mode. Internal pull-down resistor (~74kΩ). Should be connected to VSS if programming is not used
9	DACref	AI	**DAC Ref**erence voltage input for external reference
10	DACout	AO	**DAC out**put (unbuffered, Ri ~8kΩ)
11	FB	AI	**F**eed**b**ack, OPAMP inverting input

Pin	Symbol	Type	Description
12	Vout	AO	OPAMP **out**put
13	NC	-	Must be left unconnected
14	NC	-	Must be left unconnected
15	VDD3V3	S	3V-Regulator Output for internal core, regulated from VDD5V.Connect to VDD5V for 3V supply voltage. Do not load externally.
16	VDD5V	S	Positive Supply Voltage, 3.0 to 5.5 V

Abbreviations for Pin Types in Figure 5:

DO_OD : Digital output open drain

DI_PD : Digital input pull-down

DI_PU : Digital input pull-up

S : Supply pin

DO_T : Digital output /tri-state

ST : Schmitt-Trigger input

AI : Analog input

AO : Analog output

D1 : Digital input

Pin Description

Pins 7, **15** and **16** are supply pins, pins **5**, **13** and **14** are for internal use and must be left open.

Pin 1 is the magnetic field strength indicator, **MagRNGn**. It is an open-drain output that is pulled to VSS when the magnetic field is out of the recommended range (45mT to 75mT). The chip will still continue to operate, but with reduced performance, when the magnetic field is out of range. When this pin is low, the analog output at pins #10 and #12 will be 0V to indicate the out-of-range condition.

Pin 2 MODE allows switching between filtered (slow) and unfiltered (fast mode). This pin must be tied to VSS or VDD5V, and must not be switched after power up.

Pin 3 Chip Select (**CSn**; active low) selects a device for serial data transmission over the SSI interface. A “logic high” at CSn forces output DO to digital tri-state.

Pin 4 CLK is the clock input for serial data transmission over the SSI interface.

Pin 6 DO (Data Out) is the serial data output during data transmission over the SSI interface.

Pin 8 PROG_DI is used to program the different operation modes, as well as the zero-position in the OTP register.

This pin is also used as a digital input to shift serial data through the device in Daisy Chain Mode.

Pin 9 DACref is the external voltage reference input for the Digital-to-Analog Converter (DAC). If selected, the analog output voltage on pin 12 (V_{out}) will be ratiometric to the voltage on this pin.

Pin10 DACout is the unbuffered output of the DAC. This pin may be used to connect an external OPAMP, etc. to the DAC.

Pin 11 FB (**F**eedback) is the inverting input of the OPAMP buffer stage.

Access to this pin allows various OPAMP configurations.

Pin 12 Vout is the analog output pin. The analog output is a DC voltage, ratiometric to VDD5V (3.0 – 5.5V) or an external voltage source and proportional to the angle.

3.3V / 5V Operation

The AS5043 operates either at 3.3V ±10% or at 5V ±10%. This is made possible by an internal 3.3V Low-Dropout (LDO) Voltage regulator. The core supply voltage is always taken from the LDO output, as the internal blocks are always operating at 3.3V.

For 3.3V operation, the LDO must be bypassed by connecting VDD3V3 with VDD5V (see Figure 19).

For 5V operation, the 5V supply is connected to pin VDD5V, while VDD3V3 (LDO output) must be buffered by a 1 to10µF capacitor, which should be placed close to the supply pin.

The VDD3V3 output is intended for internal use only. It should not be loaded with an external load.

The voltage levels of the digital interface I/O's correspond to the voltage at pin VDD5V, as the I/O buffers are supplied from this pin (see Figure 19).

Figure 19:
Connections for 5V / 3.3V Supply Voltages

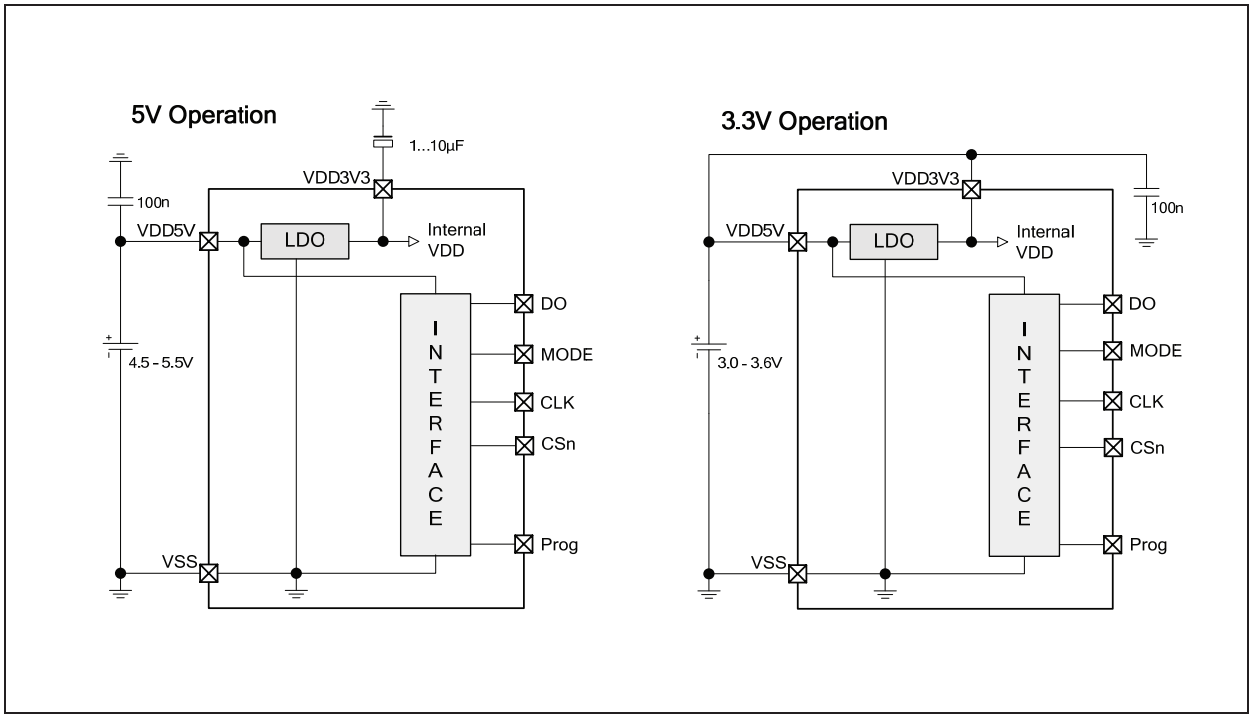

A buffer capacitor of 100nF is recommended in both cases close to pin VDD5V. Note that pin VDD3V3 must always be buffered by a capacitor. It must not be left floating, as this may cause an instable internal 3.3V supply voltage which may lead to larger than normal jitter of the measured angle.

Analog Output Voltage Modes

The Analog output voltage modes are programmable by OTP. Depending on the application, the analog output can be selected as rail-to-rail output or as clamped output with 10%-90% VDD5V.
The output is ratiometric to the supply voltage (VDD5V), which can range from 3.0V to 5.5V. If the DAC reference is switched to an external reference (pin DACref), the output is ratiometric to the external reference.

Full Scale Mode

This output mode provides a ratiometric DAC output of (0% to 100%)x Vref[1], amplified by the OPAMP stage (default =internal 2x gain, see Figure 33)

Figure 26:
Analog Output, Full Scale Mode (shown for 360°mode)

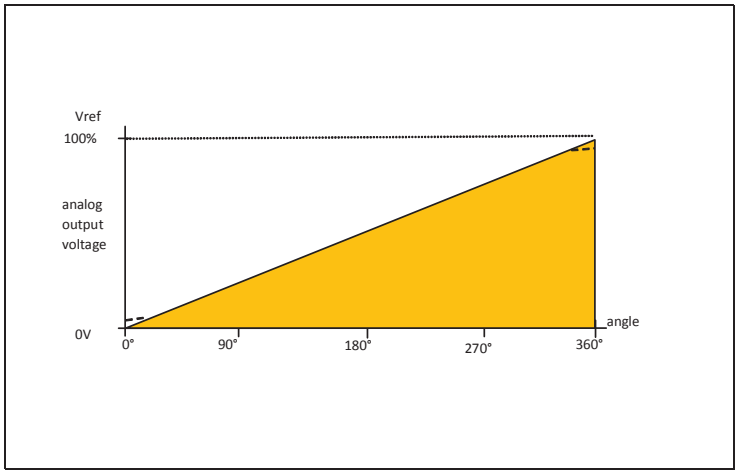

Note(s):

- In real case the output does not reach 100% Vref, because of saturation effects of the OPAMP output driver transistors. Figure 26 describes a linear output voltage from rail to rail (0V to VDD) over 360°.
- See Figure 38 for further angular range programming options.

Physical Placement of the Magnet

The best linearity can be achieved by placing the center of the magnet exactly over the defined center of the IC package as shown in Figure 43.

Figure 43:
Defined IC Center and Magnet Displacement Radius

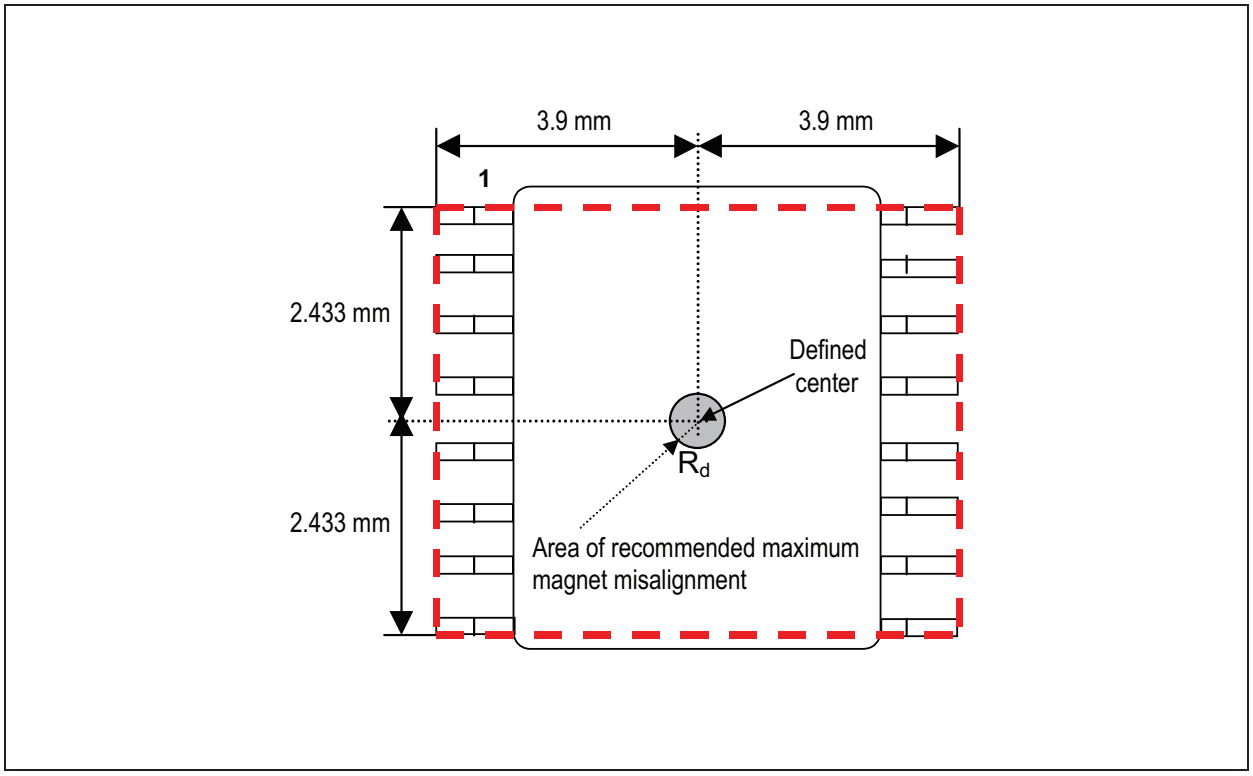

Magnet Placement

The magnet's center axis should be aligned within a displacement radius R_d of 0.25mm from the defined center of the IC with reference to the edge of pin #1 (see Figure 43). This radius includes the placement tolerance of the chip within the SSOP-16 package (± 0.235mm).
The displacement radius R_d is 0.485mm with reference to the center of the chip (see Alignment Mode).
The vertical distance should be chosen such that the magnetic field on the die surface is within the specified limits (see Figure 42). The typical distance "z" between the magnet and the package surface is 0.5mm to 1.8mm with the recommended magnet (6mm x 3mm). Larger gaps are possible, as long as the required magnetic field strength stays within the defined limits.

A magnetic field outside the specified range may still produce usable results, but the out-of-range condition will be indicated by MagINCn (pin 1), which will be pulled low. At this condition, the angular data is still available over the digital serial interface (SSI), but the analog output will be turned OFF.

Figure 44:
Vertical Placement of the Magnet

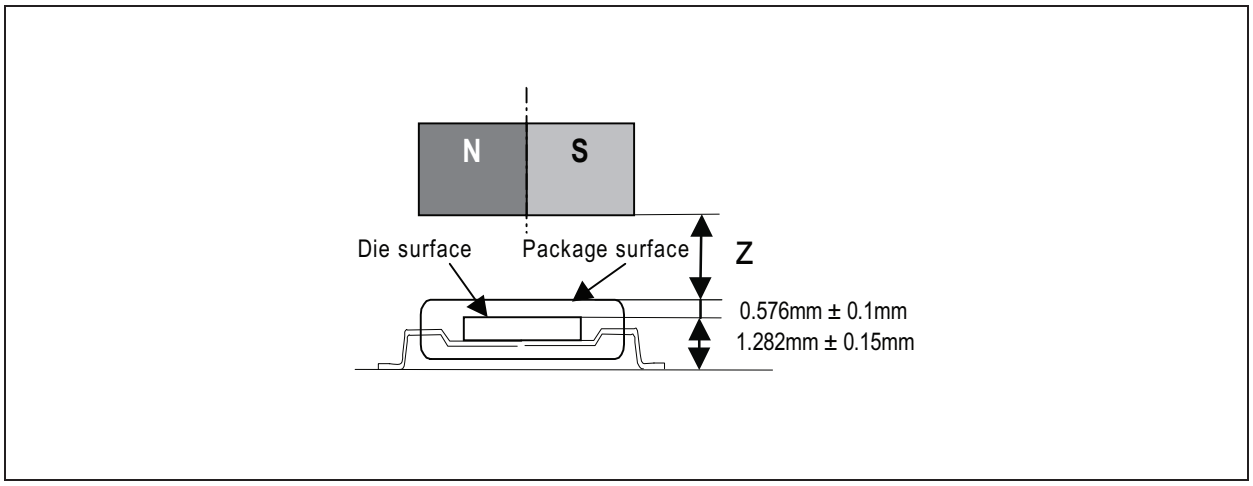

Appendix B

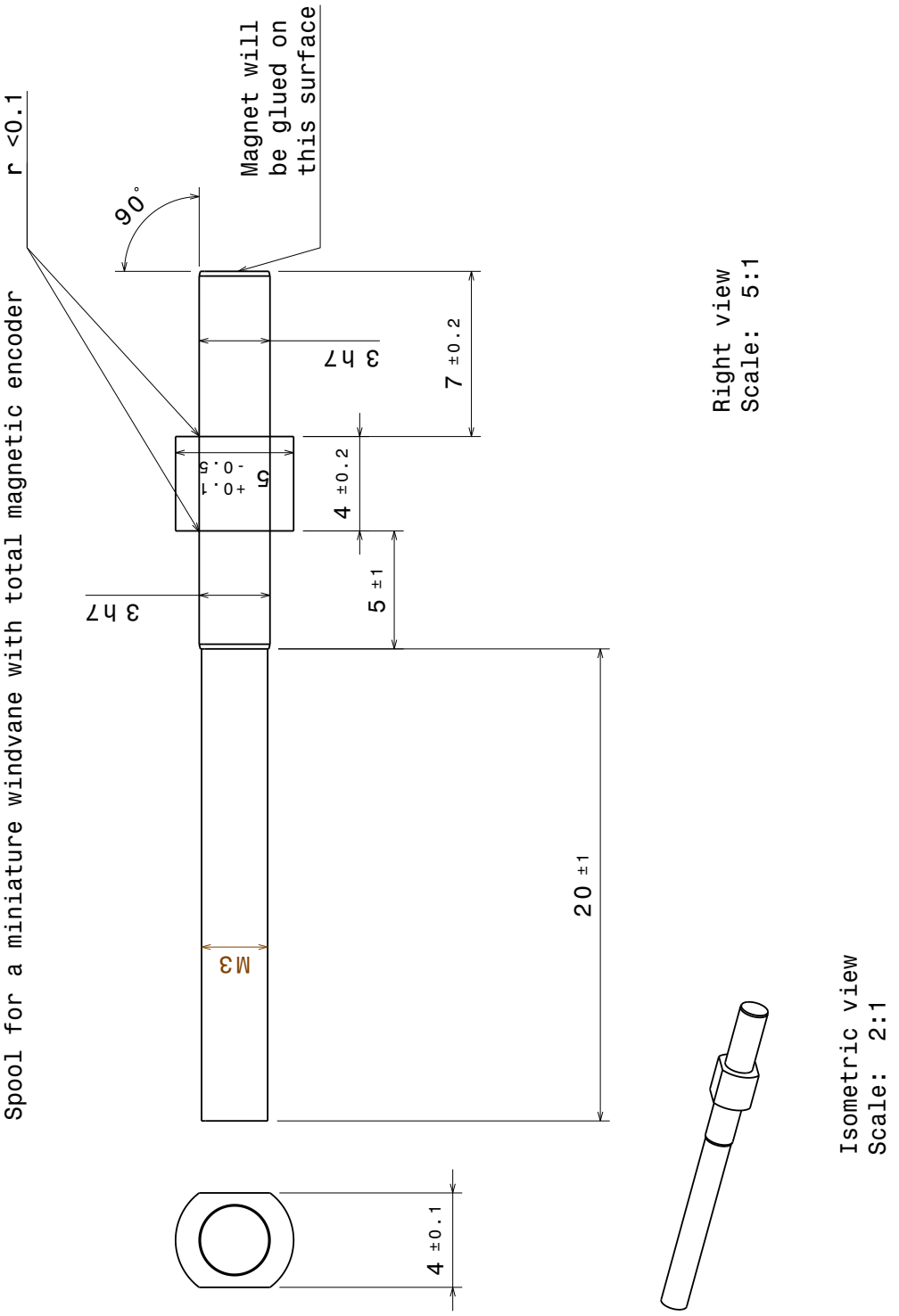
Spool for a miniature windvane with total magnetic encoder
r <0.1
Magnet will be glued on this surface
90°
3 h7
7 ±0.2
5 +0.1 -0.5
4 ±0.2
5 ±1
3 h7
20 ±1
M3
4 ±0.1
Right view
Scale: 5:1
Isometric view
Scale: 2:1

Bibliography

[1] Uwe Ahrens, Moritz Diehl, and Roland Schmehl. *Airborne Wind Energy*. Springer, Heidelberg, 2013. ISBN 978-3-642-39965-7. XVII, 3, 4, 10, 16

[2] J. B. Barlow, W. H. Rae, and A. Pope. *Low-speed Wind Tunnel Testing*. Wiley, New York, 1999. ISBN 978-0-471-55774-6. 10, 28, 34

[3] Alvaro Berzal Mejias. Wind Sensor Implementation Design. Master's thesis, Technische Universiteit Delft, the Netherlands, 2011. 16

[4] Ampyx Power B.V. Promotional video Ampyx powerplane. `www.youtube.com/watch?v=V_7VxkfSlPg`, 2013. [online] Accessed: 2017-04-06. XVII, 18

[5] Dennis W. Camp and Robert E. Turner. Response Tests of Cup, Vane, and Propeller Wind Sensors. *Journal of Geophysical Research*, 75:5265–5270, 1970. 18, 20

[6] Michael Deaves. Reynolds-Average-Navier-Stokes Methods Applied to the Non-Linear 3D Flow Effects Relevant for Leading Edge Inflatable Kites. Master's thesis, Technische Universiteit Delft, the Netherlands, 2015. XVII, 22, 23

[7] Uwe Fechner. *A Methodology for the Design of Kite-Power Control Systems*. PhD thesis, Technische Universiteit Delft, 2016. 66

[8] Bryan Franka. A tool for Aerodynamic Analysis of flexible kites. Master's thesis, Technische Universiteit Delft, the Netherlands, 2014. 10, 28

[9] Robert Gasch and Jochen Twele. *Windkraftanlagen*. Vieweg und Teubner Verlag, Wiesbaden, 4 edition, 2005. ISBN 978-3-519-36334-7. 16, 17, 18

[10] Althen GmbH. Standard Probes Datasheet. datasheet www.althensensors.com, 2017. [online] Accessed: 2017-04-06. 18, 19

[11] William Gracey. naca-summary of methods for AoA measuring, 1958. 16, 20

[12] William Gracey and Elwood F. Scheithauer. Flight investigation of the variation of static-pressure error of a static-pressure tube with distance ahead of a wing and a fuselage, 1951. 21

[13] Stephen E Hobbs. *A quantitative study of kite performance in natural wind with application to kite anemometry.* PhD thesis, Cranfield Institute of Technology, Cranfield University, 4 1986. 15, 16

[14] Gill Instruments. Wind master datasheet 3-Axis Ultrasonic Anemometer. datasheet www.gillinstruments.com, 2017. [online] Accessed: 2017-04-12. 17

[15] Miles L. Loyd. Crosswind kite power. *Journal of Energy*, 4:106–111, 1980. XVII, 2, 6

[16] Bernd Peters. Lecture notes - Umweltaerodynamik, 2016. 5, 46

[17] Benoit Python. Methodology Improvement for Performance Assessment of Pumping Kite Power Wing. Master's thesis, Technische Universiteit Delft, the Netherlands, 2017. XVII, XVIII, 27, 53

[18] Michael Ranneberg. Sensor Setups for State and Wind Estimation for Airborne Wind Energy Converters, 2013. 15

[19] Marien B. Ruppert. Development and validation of a real time pumping kite model. Master's thesis, Technische Universiteit Delft, the Netherlands, 2012. 4, 5, 11

[20] Roland Schmehl. Book of abstracts. Airborne Wind Energy Conference 2015, Delft University of Technology, 6 2015. 2

[21] spaceagecontrol. State-of-the-art air data products. `http://spaceagecontrol.com/Main/uploads/Main.Sitelist/s002a.pdf`, 2017. [online] Accessed: 2017-04-06. 19

[22] R. van der Vlugt, A. Bley, M. Noom, and R. Schmehl. Quasi-steady model of a pumping kite power system. *Submitted to Renewable Energy*, 2017. III, IV, 4, 50, 51, 52

[23] J. Wieringa. Evaluation and Design of Wind Vanes. *Journal of Applied Meteorology*, 6:1114–1122, 1967. 20, 42